DEVELOPMENT OF AN IMPROVED THERMAL MODEL OF THE HUMAN BODY AND AN EXPERIMENTAL INVESTIGATION OF HEAT TRANSFER FROM A MOVING CYLINDER

by

XIAOYANG SUN

M.S., Purdue University, Indianapolis Campus, 2003

AN ABSTRACT OF A DISSERTATION

submitted in partial fulfillment of the requirements for the degree

DOCTOR OF PHILOSOPHY

Department of Mechanical and Nuclear Engineering
College of Engineering

KANSAS STATE UNIVERSITY
Manhattan, Kansas

2012

Abstract

A new human thermal model was developed to predict the thermal responses of human body in various environments. The new model was based on Smith's model, which employed finite element method to discretize the human body. The body parts in our new model were not limited to the cylindrical shape as in Smith's model, but subjected to arbitrary shapes. Therefore, the new model is capable of dealing with more complicated shapes of the human body. Steady-state and transient temperatures of fifteen body parts were calculated for three environments: cold, neutral, and warm. Our results were compared with the data from Zhang's experimental research on the human subjects. For all three conditions, our results showed better agreement with experimental data than Smith's results did. The maximal deviation is 1°C for neutral and warm condition; for cold condition, a maximal deviation of 3.5°C is reported at hand. The comparison indicated that our new model could provide a more accurate prediction on the body temperatures.

Follow-up experiments were conducted to investigate the local and overall heat transfer from a moving cylinder in air flow. This study was expected to provide the local convective heat transfer coefficients of the human body to our new human thermal model to simulate moving humans. An experiment of a stationary cylinder in cross flow was performed to verify the accuracy and consistency of our system. Then, the experiment of a transverse oscillating cylinder in cross flow was conducted, with a oscillation frequency of 0.15 and Strouhal number of 0.3 to 1.5, depending on wind velocity. The overall Nusselt number (Nu) of the oscillating cylinder remained unaffected, compared to the stationary cylinder. This observation showed agreement with previous studies. The pivot experiment was performed to investigate swinging movement of human arms. The cylinder was positioned axially in cross flow, and reciprocated on a fixed point between horizontal and vertical positions under three wind speeds and two oscillating frequencies. The results showed that the overall Nu was between the Nu at horizontal and vertical positions in stationary state. A correlation was presented to predict the Nu of pivotal moving cylinder by using stationary Nu at horizontal and vertical positions. The correlation was proved to be valid (error less than 5%) within the range of conditions in our experiment.

DEVELOPMENT OF AN IMPROVED THERMAL MODEL OF THE HUMAN BODY AND AN EXPERIMENTAL INVESTIGATION OF HEAT TRANSFER FROM A MOVING CYLINDER

by

XIAOYANG SUN

M.S., Purdue University, Indianapolis Campus, 2003

A DISSERTATION

submitted in partial fulfillment of the requirements for the degree

DOCTOR OF PHILOSOPHY

Department of Mechanical and Nuclear Engineering
College of Engineering

KANSAS STATE UNIVERSITY
Manhattan, Kansas

2012

Approved by:

Major Professor
Steve Eckels

Abstract

A new human thermal model was developed to predict the thermal responses of human body in various environments. The new model was based on Smith's model, which employed finite element method to discretize the human body. The body parts in our new model were not limited to the cylindrical shape as in Smith's model, but subjected to the arbitrary shapes. Therefore, the new model is capable of dealing with more complicated shapes of the human body. Steady-state and transient temperatures of fifteen body parts were calculated for three environments: cold, neutral, and warm. Our results were compared with the data from Zhang's experimental research on the human subjects. For all three conditions, our results showed better agreement with experimental data than Smith's results did. The maximal deviation is 1°C for neutral and warm condition; for cold condition, a maximal deviation of 3.5°C is reported at hand. The comparison indicated that our new model could provide a more accurate prediction on the body temperatures.

Follow-up experiments were conducted to investigate the local and overall heat transfer from a moving cylinder in air flow. This study was expected to provide the local convective heat transfer coefficients of the human body to our new human thermal model for the simulation of moving humans. An experiment of a stationary cylinder in cross flow was performed to verify the accuracy and consistency of our system. Then, the experiment of a transverse oscillating cylinder in cross flow was conducted, with a oscillation frequency of 0.15 and Strouhal number of 0.3 to 1.5, depending on wind velocity. The overall Nusselt number (Nu) of the oscillating cylinder remained unaffected, compared to the stationary cylinder. This observation showed agreement with previous studies. The pivot experiment was performed to investigate swinging movement of human arms. The cylinder was positioned axially in cross flow, and reciprocated on a fixed point between horizontal and vertical positions under three wind speeds and two oscillating frequencies. The results showed that the overall Nu was between the Nu at horizontal and vertical positions in stationary state. A correlation was presented to predict the Nu of pivotal moving cylinder by using stationary Nu at horizontal and vertical positions. The correlation was proved to be valid (error less than 5%) within the range of conditions in our experiment.

Table of Contents

List of Figures

List of Tables

Acknowledgements

First of all, I would like to thank my major professor Dr.Steve Eckels, for all the help and academic guidance during my Ph.D degree. He helps me not only on the final dissertation, but also on the journal paper and course work. I would also like to thank Dr. Charlie Zheng as co-major professor, for his help on my projects and thesis. The rest members of my committee, Dr. Byron Jones, Dr. Craig Harms, and Dr. Daniel Marcus, are thanked for the contribution to my dissertation.

I appreciate financial support for my Ph.D degree from Dr.Eckels and Institute for Environmental Research.

Lastly, I would like to thank my parents. Mother and father always give me useful advice and encouragement throughout my degree. I am sorry for not being with you in last eight years, but I think my Ph.D degree is a reward for both of us.

Nomenclature

A	amplitude of cylinder oscillation
A_s	surface area of a certain element
B	mobility
c	moisture concentration
c_i	specific heat of tissue
CO	cardiac output
c_p	specific heat
$c_{p,bl}$	specific heat of blood
D	cylinder diameter, diffusivity of air
f	oscillating frequency
F	shedding frequency parameter
F_c	frequency of cylinder oscillation
F_n	frequency of vortex shedding
f_s	vortex shedding frequency
f_{St}	frequency at Strouhal number
Gr_D	Grashof number with cylinder diameter as characteristic length
H	height of a certain element
h	heat transfer coefficient
h_{ai}	convective heat transfer coefficient between arteries and tissue
h_{vi}	convective heat transfer coefficient between venous and tissue
J	mass transfer rate
k	conductivity
k_i	tissue conductivity
L	cylinder length
M	metabolic rate generated by human body

m_{cr}	core mass
m_{sk}	skin mass
$M_{activiy}$	metabolic rate due to activities
M_{basal}	basal metabolic rate
M_{shiv}	metabolic increase by shivering
$M_{shivering}$	metabolic increase due to shivering
N	one-dimensional array of the shape functions
Nu_D	Nusselt number with cylinder diameter as characteristic length
$Nu_{horizonal}$	Nusselt number of stationary cylinder in horizontal position
Nu_{pivot}	overall Nusselt number for pivot experiment
$Nu_{vertical}$	Nusselt number of stationary cylinder in vertical position
$\{P\}$	Pressure array for solution method
P	Pressure
P^0	pressure at reference point
P_i	perimeters of quarter ellipses in certain element
Pr	Prandtl number
Pr_s	Prandtl number evaluated at cylinder surface
Q	heat flux
q'	heat generation of the human body
$q''_{corrected}$	corrected readings for heat flux sensor
q_{dry}	sensible heat loss through skin
q_{evap}	evaporative heat loss through skin
q''_{in}	direct heat flux calculated from heat flux sensor
q_{mi}	metabolic generation of tissue
$q''_{reading}$	voltage readings from heat flux sensor
q_{res}	total heat loss through respiratory system

Re_D	Reynolds number with cylinder diameter as characteristic length
Re_x	Reynolds number with x as characteristic length
R_{H_2O}	gas constant
RQ	respiration quotient
r_i	radius used for calculation
S	vertical height of a certain element
St	Strouhal number
T	body temperature
T_{ai}	arterial temperature
T_{amb}	ambient temperature
T_{cal}	temperature for calculation
T_{sur}	surface temperature of the cylinder
T_{vi}	venous temperature
t_{cr}	core temperature
t_{sk}	skin temperature
U	voltage
u	fluid velocity near the cylinder surface
V	free stream velocity, the volume of a certain element
v	mean velocity of air
$\dot{V}_{O_2}$	Oxygen consumption rate
v_{bl}	mean blood velocity
v_{resp}	air velocity in respiratory tract
W	work done by the body
w_b	volumetric rate of blood
x	coordinate in the streamline direction
y	coordinate perpendicular to the streamline direction
z	coordinate in axial direction

γ	correction factor
θ	angle between the free stream direction and a certain point on the cylinder surface
μ	viscosity of the fluid, chemical potential
μ^0	chemical potential at reference point
ν	kinematic viscosity of the fluid
ρ	density
ρ_b	blood density
ρ_i	tissue density

Chapter 1 - Introduction

1.1 Objectives

The motivation of this thesis originated from a fact that the existing mathematical models to predict human thermal status still had room to improve. There were two main limitations for the previous models. First, the body parts used for discretization remained cylindrical since 1990s, although more powerful computers were widely used. The cylindrical body parts did not accurately represent all body parts. Second, the human body simulated by previous models were not moving. However, the movement of humans could result in a significant change of heat transfer, i.e., the convective heat transfer changed if a human was moving. Due to above two limitations, an improved thermal model, which was based on Smith' model (Smith 1991), was developed with shaping capability, and then the experiments were performed to study the heat transfer of a moving cylinder in cross flow. With the new model, more accurate simulation results could be obtained.

The improvement of the new model was proved by comparing the simulation results with others' experimental data taken from the test on human subjects. The overall and local convective heat transfer coefficients obtained from the moving cylinder experiments could be fed into our numerical model, replacing old constant coefficients. Meanwhile, the investigation on the moving cylinder was also a popular topic in the study of heat transfer. The pivotal movement of the cylinder in cross flow was first studied in this thesis. The extension of our work can focus on incorporation of experimental data and our new model. If the convective heat transfer coefficients obtained from experiments can be incorporated into the thermal model, it is possible to simulate the effect of a moving human, which improves the thermal simulation of humans.

1.2 Background

The physiology, temperature control mechanism, and thermal responses of the human body are presented in section 1.2.1. The fundamentals of convective heat transfer and stationary cylinder in cross flow are presented in section 1.2.2. The background section only introduces

basic knowledge regarding to the main topics. Details of the human thermal models and cylinder heat transfer will be introduced in the chapter of literature review.

1.2.1 Human physiology

Human body is an active organism which has ability to maintain a relatively constant internal environment. The process by which the body regulates its internal environment is called homeostasis. Homeostasis regulation involves three mechanisms: the receptor, the control center, and the effecter. The receptor receives information that something changing in the environment effects on the body. The control center receives and processes information from the receptor, and then sends commands to effecter. Lastly, the effecter responds to the commands of the control center by either opposing or enhancing the physiological activities. The receptor may receive both negative and positive feedbacks from the changing environments. The negative feedback refers to a reaction in which the system responds in such a way as to reverse the direction of change. For instance, when the concentration of carbon dioxide in the human body increases, the lungs are signaled to increase their activity and expel more carbon dioxide. Thermoregulation is another example of negative feedback. When body temperature rises (or falls), receptors in the skin and the hypothalamus sense a change, triggering a command from the brain, and some mechanisms are carried out to pull the body temperature back to normal standard. The positive feedback is a response to amplify the change. It is less common than negative feedback, but also has its applications, such as in nerves threshold and blood clotting.

Among all the feedbacks in human system, thermal response is one of the most important responses, because it has closely relation to our body thermal conditions, which are usually vital to our health. Basically, there are three types of thermal responses: vasomotor, sudomotor, and shivering. Vasomotor responses is such a mechanism that the control center regulates core body temperature to normal level by increasing or decreasing blood vessel diameter in hot or cold environment. Vasodilation and vasoconstriction are two opposite reactions of vasomotor response. When human stays in hot environment, the core body temperature starts to rise, and the vasodilation process occurs. The control center signals blood vessels to dilate in diameter, and cause cardiac output (blood flow rate) to increase. Thus, more heated blood is diverted to the skin through superficial blood vessels, where heat can be more easily released into ambient. In

the process of vasodilation, the blood flow rate increases, while vascular resistance and blood pressure decrease. Vasoconstriction, the opposite process of vasodilation, is the narrowing of the blood vessels resulting from contraction of muscular wall of the vessels. If the environment is cold, the blood vessels will constrict, leading to the increasing of vascular resistance and blood pressure, and the decreasing of blood flow rate. So there is less body heat released to ambient. The skin also turns paler because less blood reaches the surface, preventing the radiation of heat. Assuming that the environmental temperature continue rising, and the vasodilation response is not enough to pull the core temperature back to normal level, then sudomotor response occurs. The sweat glands are stimulated and begin to sweat, then the evaporation phenomenon occurs on the skin surface so that the heat is released. Because latent heat loss by evaporation is much larger than convective heat loss by blood, so sudomotor response can regulate core temperature more efficiently than vasodilation. It should be noted that the human body may lack water and salt after sudomotor process because of fluid and mineral loss by sweating, so it is very important to supply nutrition after large amount of sweating. Shivering has a opposite but similar sense to sudomotor. When core temperature drops to some degree and vasoconstriction cannot regulate it to normal level, shivering response occurs. Shivering response is able to generate extra heat by physical contraction of muscles. Although this movement of muscle causes additional convective heat loss on the skin surface, the heat generation by shivering is much more than this additional loss.

Core temperature, as mentioned above, is one of the most typical and important indicative temperatures used for both experimental study and human thermal simulation. It is an operating temperature of human body, specifically in deep structure of the body, for example, liver temperature. In normal condition, core temperature is maintained within a narrow range so that essential enzymatic reaction can occur. Higher or lower in core temperature may lead to disorder of thermoregulation and chemical environment. Hyperthermia occurs when human body absorbs more heat than it can dissipate. It is usually caused by long exposure to high heat source. 40°C (104°F) or above is considered a lift-threatening signal, and needs immediate medical treatment. In contrast to hyperthermia, hypothermia is an acute condition when core temperature drops below that required for normal metabolism and body function. It is caused by excessive exposure to cold environment. Symptoms appear when core temperature drops by 1-2°C (1.8 -

3.6 °F) below normal temperature. Another confusable temperature concept is fever. Although the symptom of fever is similar to hyperthermia, in which the core temperature raises above normal level, the mechanisms of fever and hyperthermia are different. In fever, the temperature raising is the command from control center, usually brain, keeping the core temperature at certain level. This is an active process since most fever is caused by disease or virus. In contrast, the process of hyperthermia is a passive one: excessive heat stress is exerted on human, exceeding the thermoregulation ability of the human body. Skin temperature, usually referring to the average surface temperature over a certain body part or the whole body, is another temperature concept which is widely used in experimental measurements. Although some research show that there is no strong evidence that skin temperature dominates thermoregulation in human body, more researchers believe that it is a important indicator for some thermal responses, such as sweating and shivering. In this dissertation, the combination of skin and core temperatures is used to predict blood vessel diameter in vasomotor process and sweating threshold in sudomotor process.

To develop a human thermal model, respiratory system should also be taken into account because it is another way for human body to exchange heat and mass with environment. The key parameter, air velocity in respiratory tract, can be obtained from the oxygen consumption rate, which is a function of activity level and metabolic generation. There are some other mechanisms for the human body to exchange heat with environment, such as heat convection, evaporative heat loss and radiation. Equation 1-1, 1-2 and 1-3 show the calculation for these three mechanisms (ASHRAE 2005). In Equation 1-1, ε is the emissivity of the clothing, usually close to unity unless particular material is used, so the overall radiant heat transfer coefficient h_r is close to 4.7 for common situations. Equation 1-2 gives the calculation of convective heat transfer coefficient h_c for a seated human in moving air, and the velocity limitation is from 0.2 to 4.0m/s. Evaporative heat transfer coefficient h_e can be obtained by Lewis relation in Equation 1-3, where LR is Lewis ratio evaluated 16.5 K/kPa for most calculations. Calculation results from Equation 1-1, 1-2 and 1-3 show that heat convection, evaporation and heat radiation play important roles in heat exchange of the human body.

$$h_r = 4.7\varepsilon \qquad 1\text{-}1$$

$$h_c = 8.3V^{0.6} \qquad 1\text{-}2$$

$$h_e = \mathrm{LR} h_c \qquad 1\text{-}3$$

1.2.2 Convection and cylinder in cross flow

Convection is the transfer of heat from one place to another by the movement of fluids. The presence of bulk motion of the fluid enhances the heat transfer between the solid surface and the fluid. Convection is usually the dominant form of heat transfer in liquids and gases. Convective heat transfer actually describes the combined effects of conduction (heat diffusion), plus heat transfer by bulk fluid flow, a process technically termed "heat advection". There are two types of convective heat transfer, natural convection (or free convection) and forced convection. Natural convection is driven by buoyancy forces that result from the density variation due to temperature variation in the fluid. When the mass of the fluid is in contact with a hot surface, its molecules separate and scatter, causing the mass of fluid to become less dense. When this happens, the fluid is displaced vertically or horizontally while the cooler fluid gets denser and the fluid sinks. Thus the hotter volume transfers heat towards the cooler volume of that fluid. The migration of air from high density area to low density area results in velocity variation. The velocity due to fluid density difference is very low, so the velocity boundary layer is usually laminar boundary layer. However, it should be noted that free convection boundary layers are not restricted to laminar flow. As with forced convection, hydrodynamic instabilities may arise. The disturbances in the flow may be amplified, leading to transition from laminar to turbulent flow. It is proved by experimental investigation that transition to turbulence has a strong effect on heat transfer. Forced convection is a type of heat transport where fluid is driven by external force. It is a very useful method to transfer heat energy efficiently, and has a wide application in our day life. Since the flow is driven by external source, a high relative velocity of solid surface to fluid can be induced, which results in a high heat transfer rate on the solid surface. In any forced convection situation, some amount of natural convection is always present whenever there are gravity forces present. When the natural convection is not negligible, such flows are typically referred to as mixed convection.

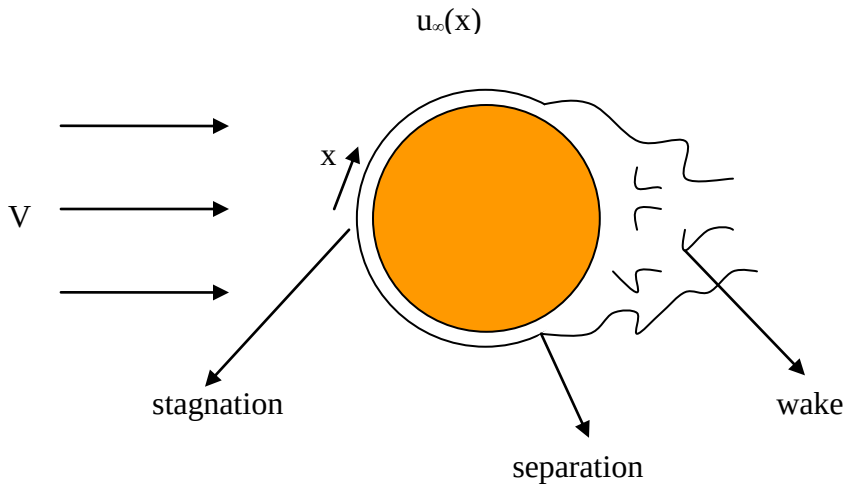

Figure 1.1 Schematic of flow over a circular cylinder

Cylinder in cross flow is a typical external flow problem which involves fluid motion normal to the axis of a circular cylinder. We are interested in this model because the basic body shape used in our numerical model is cylindrical. As shown in Figure 1.1, the free stream fluid is brought to rest at the forward stagnation point with maximal pressure. From this point, the pressure decreases with increasing x, and the boundary layer develops under the influence of a favorable pressure gradient ($dp/dx < 0$). The pressure eventually reach a minimum somewhere along the cylinder, depending on free stream properties and cylinder geometry. After this minimum point further boundary layer development occurs towards the rear of the cylinder in the presence of an adverse pressure gradient ($dp/dx > 0$). Accordingly, the fluid accelerates at stagnation point because of the favorable pressure gradient ($dp/dx < 0$), and reaches maximum velocity when $dp/dx = 0$; then the fluid decelerates because of the adverse pressure gradient ($dp/dx > 0$). As the fluid decelerates, the velocity gradient at the surface, $\frac{\partial u}{\partial y}|_{y=0} = 0$, eventually become zero at some point, which is termed separation point. At the separation point, fluid near the surface lacks sufficient momentum to overcome the adverse pressure gradient, and downstream flow is impossible. Since fluid may flow back upstream, the separation of boundary layer occurs. Once boundary layer separation occurs, the boundary layer detaches from the

surface, and wake flow is formed in the downstream region. Because both forward flow and backward flow exist in this region, vortex is formed and flow is highly irregular. It is experimentally proved that the heat transfer is enhanced in wake flow region due to irregular motion of the fluid. The position of separation point is dependent on Reynolds number Re_D, with cylinder diameter D as characteristic length. The Reynolds number is defined as $\mathrm{Re}_D = \frac{VD}{\nu}$, where V is fluid velocity and ν is kinematic viscosity of fluid. If $\mathrm{Re}_D \le 2\times10^5$, the boundary layer remains laminar, and separation occurs at $\theta \approx 80°$; if $\mathrm{Re}_D \ge 2\times10^5$, boundary layer transition occurs, and separation point is delayed to $\theta \approx 140°$.Since the velocity field of cylinder in cross flow is complicated, as discussed above, the analytical solution for heat transfer is hard to obtain. There are experimental results and empirical correlations for local and overall Nusselt number (Nu). More details will be discussed in the literature review chapter.

The heat transfer of a moving cylinder in cross flow is much more complicated than stationary cylinder. The convective heat transfer coefficient depends on many factors, such as the direction of movement, speed of movement, boundary layer type, etc. In our experiment, two types of movement were investigated: transverse oscillation and pivot movement. These two cases have been studied for many years, but still remain controversial. The details of the moving cylinder cases will be reviewed in the next chapter, and their experimental results will be also presented and discussed. Numerical solution for a moving cylinder in cross flow was reported by Zhang (2008), who implemented an immersed-boundary method on a transversely oscillating cylinder to study the heat transfer. The experimental data could be compared to numerical solutions for the purpose of validation. If the simulation method was validated, it could be used for obtaining the heat transfer coefficients for the body parts. The advantage of numerical simulation is the flexibility to simulate moving humans in any condition, which cannot be performed by experiment.

In introduction chapter, the objective of this thesis was presented, and the fundamentals of human physiology and convective heat transfer were introduced. To improve the thermal simulation on the human body, it is significant to develop a shaping-capability model. The following experimental investigation of heat transfer from a moving cylinder is not only a creative experiment, but also a good addition to our thermal model. The literature reviews of

previous models and moving cylinder will be presented in Chapter 2. The thermal model and solution method will be developed in Chapter 3. The results of our model will be discussed in Chapter 4. For experiment, apparatus setup and experiment procedure will be introduced in Chapter 5, and results and data analysis will be discussed in Chapter 6. Finally, a conclusion will be drawn in Chapter 7.

Chapter 2 - Literature Review

Previous numerical models of the human body are reviewed in section 2.1. Gagge (1971), Stolwijk (1966), and Wissler' (1985) models are considered basic models, which include the most important physical and physiological mechanisms of the human body, such as heat transfer inside and outside the body, circulatory system, and thermal responses, etc. The following models are modified version of these three models in the aspects of clothing, blood vessel, or the introduction of new physiological correlations. The literatures regarding a cylinder in cross flow are reviewed in section 2.2. Stationary and oscillating cylinder in cross flow has been studied for many year, but there are only a few references about the axially aligned cylinder in cross flow

2.1 Human thermal models

The earliest effort to develop biothermal human model can date back to 1960s. Wyndam and Atkins (1969) developed solutions for heat flow in human body and temperature regulation under heat stress with the aid of analog computers. The models, which were based on biological and physiological facts of human body, were not complex because the computer was not powerful enough to finish high level computations. With the development of faster computer, called "super computer" in 1980s, some more complicated models were presented.

2.1.1. Gagge's Model

Gagge's model is described in ASHRAE handbook Fundamentals (2005) and other two publications by Gagge (1971) and Stolwijk (1970) in 1970s. It is a lumped thermal parameters model which divides the body into two concentric shells, an inner layer and an outer layer. The inner layer represents internal organs, bone, muscle and several types of tissues, while the outer layer represents skin. The temperature for each layer is assumed to be a uniform variable, which is called "bulk temperature". Two differential equations of energy conservation are written for two layers as

For core layer:

$$M + M_{shiv} = W + q_{res} + (K + \text{SkBF}\ c_{p,bl})(t_{cr} - t_{sk}) + m_{cr} c_{cr} \frac{dt_{cr}}{d\theta} \qquad 2\text{-}1$$

For skin layer:

$$(K + \text{SkBF}\ c_{p,bl})(t_{cr} - t_{sk}) = q_{dry} + q_{evap} + m_{sk} c_{sk} \frac{dt_{sk}}{d\theta} \qquad 2\text{-}2$$

Equation 2-1 is the differential equation for inner layer, where M is the metabolic rate generated by human body, $M_{shiv}$is the metabolic increase by shivering, W is the work done by the body, q_{res} is the total heat loss through respiratory system. The last two terms express the heat conduction between core and skin, and the heat storage rate in core layer.

Equation 2-2 formulates the skin layer energy balance, where q_{dry} is the sensible heat loss through the skin, q_{evap} is the evaporative heat loss through the skin, and other two terms have the same meaning as in Equation 2-1.

Equation 2-1 and 2-2 are from 1st law of thermal dynamics, taking into consideration the metabolic generation by human, work done by activity, heat conduction and diffusion through respiratory system and skin, heat conduction between two layers, and transient energy storage. Although this equation is a rough description of core layer, it includes the most basic phenomena of energy exchange in human body. Most of the following models adopt Gagge's energy formulation to develop differential equations.

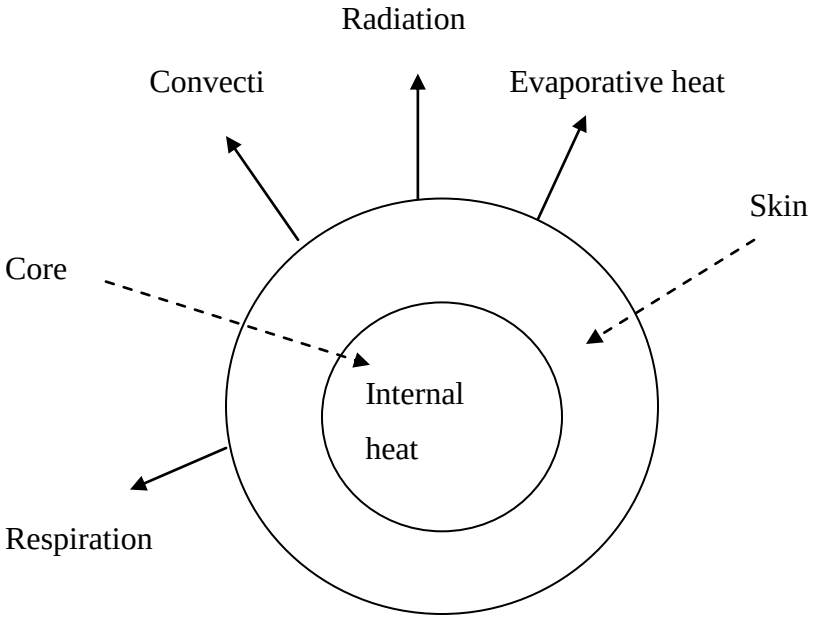

Figure 2.1 Gagge's two-node model

Gagge's model describes a transient process of body temperature subject to uniform environment. With the infinite time marching, the skin and core compartment come to steady state and temperature of each part goes constant. The circulatory system and respiratory system are not well simulated in Gagge's model. No blood vessel is specified, and volumetric blood flow rate is a function of core and skin temperature only. Blood flow rate is used to determine the mass fraction (the ratio of skin or core mass to total mass) of skin or core compartment and heat transfer rate of conduction in between. Respiratory effect is only simulated as the heat conduction through the skin, but no mass transfer included. Due to the incomplete simulation of circulatory and respiratory system, the results from Gagge's model mainly reflect the influence of environmental changes on human body, and not a lot of feedback from inside human mechanism is indicated.

2.1.2. Stolwijk's Model

Stolwijk (1966, 1970) extended Gagge's idea and developed a new human thermal model through 1966 - 1971. This model divides human body into six different segments as head, trunk,

arm, hand, leg, and foot. Each part has four concentric layers, representing core, muscle, fat and skin. A central blood compartment links the six segments together via the appropriate blood flow rate to each of the segment. Schematic of Stolwijk model is shown in Figure 2.2.

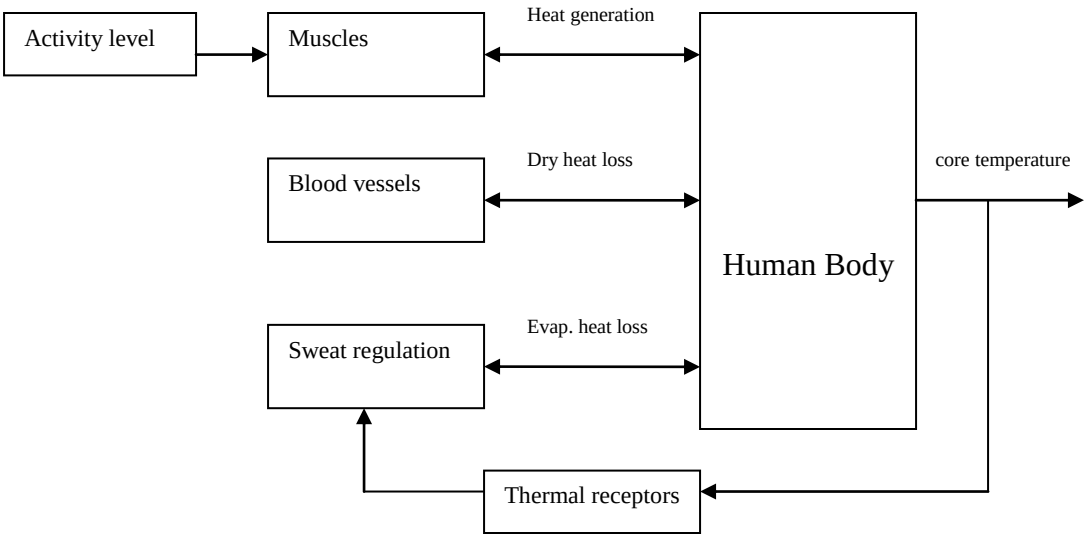

Figure 2.2 Schematic of Stolwijk's model

The temperature in each node is assumed to be uniform, just like Gagge's model, and the blood flow rate is a function of temperature of blood pool (node). Each node exchanges heat with adjacent nodes by heat conduction and with central blood pool by heat convection. The control equations are written for each of 25-nodes, which are very similar to that of Gagge's model except an additional term added to represent heat convection from the blood vessels.

Stolwijk model is still a multi-node model, which assumes a uniform temperature for each node. This assumption makes the model incapable of calculating the changing environmental conditions. However, Stolwijk's model improved Gagge's model in two ways. Firstly, Stolwijk's model is capable of calculating radial temperature distribution in the individual body part. Second, a central blood pool is included to imply the heat convection effect caused by blood vessel, although the connection model for the blood vessels is very simple.

2.1.3. Wissler's model

Wissler's model (1964, 1966, 1985) is one of the complete human thermal models. The human body is divided into 15 elements to represent head, thorax, abdomen, upper arms, lower arms, hands, thighs, calves and feet. Each element has three vascular systems consisting of arteries, veins, and capillaries. The large arteries and veins are modeled using an arterial blood pool and a venous blood pool. Arterial blood entering each body element flows into the capillaries of that element or into the arteries of more distal elements. Blood leaving the capillaries flows into the veins where it mixes with the venous return from the more distal elements. The mixed venous stream then returns to the heart and lungs before entering the arterial system for recycling.

Energy equations are written for each element, including heat storage, metabolic heat generation, convective heat transfer due to blood flow, and heat conduction in radial direction, as in Equation 2-3.

$$\rho_i c_i \frac{\partial T_i}{\partial t} = \frac{1}{r}\frac{\partial}{\partial r}(k_i r \frac{\partial T_i}{\partial r}) + q_{mi} + \rho_b c_b w_b (T_{ai} - T_i) + h_{ai}(T_{ai} - T_i) + h_{vi}(T_{vi} - T_i) \quad \text{2-3}$$

where ρ_i is the density of tissue, c_i is the specific heat of tissue, T is the instantaneous temperature of tissue, k_i is the conductivity of tissue, q_{mi} is the metabolic generation of tissue, ρ_b is the density of blood, c_b is the specific heat of blood, w_b is the volumetric rate of blood, T_{ai} is the arterial temperature of tissue, T_{vi} is the venous temperature of tissue, h_{ai} is the convective heat transfer coefficient between arteries and tissue, h_{vi} is the convective heat transfer coefficient between venous and tissue.

Two additional energy equations are written for the arteries and venous blood pools in each element because of the introduction of arterial and venous temperature distribution in Equation 2-4 and 3-5 as

$$m_{ai} c_b \frac{dT_{ai}}{dt} = \rho_b c_b w_{ai}(T_{am} - T_{ai}) + 2\pi l_i \int_0^{a_i} h_{ai}(T_i - T_{ai}) r dr + h_{avi}(T_{vi} - T_{ai}) \quad \text{2-4}$$

$$m_{vi} c_b \frac{dT_{vi}}{dt} = \rho_b c_b w_{vi}(T_{vn} - T_{vi}) + 2\pi l_i \int_0^{a_i} (\rho_b c_b w_{vi} + h_{ai})(T_i - T_{vi}) r dr + h_{avi}(T_{ai} - T_{vi}) \quad \text{2-5}$$

Then, a series of boundary conditions and initial conditions are specified at the surface of skin. The sensible heat loss through skin, evaporative heat loss through skin, and the radiation heat exchange are all included in these conditions.

Wissler made a significant contribution in his model to predict blood flow rates, the metabolic heat generation rate, and the sweat rate. A series of mass balance equations are set for the control system, including the mass balance of oxygen, carbon dioxide and lactic acid. From these control equations, oxygen requirement can be calculated, then the metabolic rate generation can also be obtained.

Generally, Wissler's model is a significant improvement over Gagge's and Stolwijk's model to a great extend. A set of criteria to describe human passive system is presented, and the circulatory system is also enhanced by the employment of blood pool. To validate this model, Wissler tested several practical cases and compared to experimental references. The results seem to be inspiring due to the good accuracy. However, limitations of this model should also be mentioned. One of the most significant limitations is the assumption of axial symmetry in each of the cylindrical elements. Even the environmental conditions are approximately uniform, temperature variation along the longitude direction exists. Another limitation is that the model does not work well for non-uniform boundary conditions, especially for cold environment. In addition, more detailed description of vascular system is remained to improve.

In the next section we will look through some other human thermal models developed within the last twenty years. Not all the information of the model is given, but just the important modifications to the old models will be shown and discussed. These models include Smith model (1991), Yi's model (2004), and Salloum's model (2007), etc.

2.1.4. Smith's Model

Smith's model (1991) was developed in 1991, based on both Stolwijk's and Wissler's model. It is a transient, three-dimensional human thermal model developed by using finite element method. The employment of this method leads to a more accurate results and a potential to deal with non-uniform environmental conditions. Smith improved Stolwijk's and Wissler's model in three major ways: a realistic geometric representation of human body, a modified controlling system, and an improved controlled system (or passive system). These three

modifications will be introduced in the following paragraphs.

Geometric representation of body shape. Like Wissler's model, Smith still uses 15 cylindrical segments to represent human body, but the concentric layers are no longer fixed at four. For the torso and head, four shells are used to represent core, muscle, fat and skin; for other parts, i.e. hand, arm or leg, three shells are used to represent bone, tissue and skin. This configuration seems to be simpler than Wissler's model, but it is not the true. In fact, there are nine types of element, corresponding to brain, abdomen, lung, bone, muscle, fat, skin, blood vessel, respiratory tract, etc, respectively. Each element must be assigned to one of the nine types, and each type of element has its own physical properties and thermal parameters, such as thermal conductivity, specific heat, density, etc. Thus, a relatively realistic human is constructed.

Controlling system. Controlling system refers to the thermal regulation and response of human body when the body is subject to a particular environment, i.e. cold weather. The main thermal regulation is metabolic generation, and the main thermal response is metabolic increase due to shivering, vasomotor, and sweating. Smith drops most of the empirical correlation formulas in Wissler's model, and used the new published data in medicine and physiology journals (around 1990s), such as cardiac output data, blood vessel radii data, metabolic generation subject to different level of activities, and sweating rate data, etc. By using this series of new data, a more accurate prediction of human thermal response should be expected.

Passive system. Passive system refers to the body tissues which is controlled by controlling system and reacted with the changes of thermal responses. Typically, the controlled system can be considered as the whole human body. To improve the controlled system, Smith also replaces the old correlations with the new data, such as volumetric flow rate, oxygen requirement for respiratory system, blood pressure distribution, etc. It has been validated that with the new correlations better results are obtained. In addition to updating the physical data, Smith also improved vascular system. Specifically, the types of blood vessels are increased in her model.

To validate the performance of this model, Smith tried more than ten cases, covering cold, neutral, warm environment conditions and various levels of activity. The results are comparable to experimental results.

2.1.5. Fiala's model

Fiala's model (2001) is based on Wissler's model. This model improved human thermoregulation and response correlations. From 26 independent experiments, Fiala found that the human thermoregulation and response, such as shivering, vasoconstriction, vasodilatation, and sweating, are strongly dependent on the mean skin temperature and head core temperature. Fiala used a regression analysis to obtain the curve fit for those thermoregulation parameters. The regression formula can be expressed as follows:

for shivering

$$\begin{aligned} \mathrm{SH} &= 10[\tanh(0.48T_{sk,m} + 3.62) - 1]T_{sk,m} \\ &- 27.9T_{hy} + 1.7T_{sk,m}\frac{dT_{sk,m}}{dt} - 28.6 \end{aligned} \qquad \text{2-6}$$

for sweating

$$\begin{aligned} \mathrm{SW} &= [0.8\tanh(0.59T_{sk,m} - 0.19) + 1.2]T_{sk,m} \\ &+ [5.7\tanh(1.98T_{hy} - 1.03) + 6.3]T_{hy} \end{aligned} \qquad \text{2-7}$$

for vasoconstriction

$$\mathrm{Cs} = 35[\tanh(0.34T_{sk,m} + 1.07) - 1]T_{sk,m} + 3.9T_{sk,m}\frac{dT_{sk,m}}{dt} \qquad \text{2-8}$$

for vasodilatation

$$\begin{aligned} \mathrm{D1} &= 21[\tanh(0.79T_{sk,m} - 0.70) + 1]T_{sk,m} \\ &+ 32[\tanh(3.29T_{hy} - 1.46) + 1]T_{hy} \end{aligned} \qquad \text{2-9}$$

To validate his model, Fiala compared with Stolwijk's model and experimental results under the same environmental conditions. It is evident that Fiala's model is closer to the experimental results than Stolwijk's.

2.1.6. Li's model

Li's model (2004) modified Stolwijk's multi-node model by considering sweat

accumulation on the skin surface and is applied to simulate the human physiological regulatory response. In Stolwijk's model, the moisture accumulated on the surface skin is ignored, and the sweating phenomenon is described by a parameter called "wettedness", which denotes the percentage of skin covered by sweat. It is pointed out by Jones and Ogawa (1992,1993) that wettedness cannot predict sweating phenomenon very well, and they raised a mass-balance-based method to predict the sweating rate accumulated on the skin surface. Li's model just applied Jone's idea and developed an alternative sweating model. In this model, the sweating accumulation on the skin surface can be derived as

$$\frac{dm_{s,i}}{dt} = m_{rsw,i} + \frac{P_{sat,i} - P_{sk,i}}{R_{esk,i} h_{fg}} - \frac{P_{sk,i} - P_{ea,i}}{R_{ea,i} h_{fg}} \qquad 2\text{-}10$$

One of the advantages to use this method is that sweating accumulation can be well predicted on the surface surroundings, so it is convenient to apply the clothing model if the mass transfer rate between skin and clothing is calculated.

2.1.7. Salloum's model

Salloum's model (2007) is a mathematical multi-segmented model based on an improved Stolwijk and Wissler models for predicting nude human thermal and regulatory responses. The creation of Salloum is to develop realistic blood vessel arrangement.

For any body element, the blood exiting the arteries and flowing into the capillaries is divided into blood flowing in the core (exchanges heat by perfusion in the core) and blood flowing into the skin layer (exchanges heat by perfusion in the skin). The blood vessel data is from Avilio's paper (Avilio 1980). In this work, the Avolio multi-branched model of the human arterial system is used where arteries are divided into 128 vessels starting from the central vessels to major peripheral arteries supplying the extremities including vessels in the order of 2.0 mm in diameter. The vein arrangement is similar to the arteries' such that each artery-vein pair is represented by two parallel cylinders. The flow in veins is assumed non-pulsatile, and is equal to the mean velocity value of the corresponding arteries. Veins are bigger than arteries where the vein diameter is assumed equal to twice of corresponding artery diameter.

With this arrangement and cardiac output data, the whole blood vessel system can be simulated, and the blood flow for each node can also be calculated. It is evident that this realistic

blood vessel system is better than previous blood vessel network.

2.2 Cylinder in cross flow

We are interested in the overall and local Nu for three cases: stationary cylinder in cross flow, transverse oscillating cylinder in cross flow, and pivotal motion of axially aligned cylinder in cross flow. Heat transfer for stationary cylinder in cross flow has been studied by many researchers in past 100 years. A correlation for local Nu was presented by Zukauskas (1987) for low Reynolds number, and the classical correlations for overall Nu were presented by Churchill (1977), Hilpert (1933), and Zukauskas (1972). Heat transfer of transverse oscillating cylinder in cross flow was first studied by Sreenivasan (1960) for small value of oscillating frequency f. The later work by Kezios (1966), Saxena (1978), Cheng (1997), Gau (1999), Park (2001), and Pottebaum (2006) etc, implied that Nu might be enhanced if oscillating frequency met certain requirements. For the cylinder axially aligned in cross flow, several journal papers were found to study the velocity field and boundary layer reattachment phenomenon. However, there was very little discussion of the heat transfer. The heat transfer was highly related to the velocity field and wake type of the flow, which makes the velocity boundary layer and wake flow very complicated. Although there is no heat transfer correlation or empirical equation for axially aligned cylinder, it is still necessary to review relevant papers.

2.2.1 Stationary cylinder in cross flow

Nu from stationary cylinder in cross flow has been proved to be strongly related to Re_D, with cylinder diameter D as characteristic length. Some correlations also include Prandtl Number (Pr) as variables. At the forward stagnation point, boundary layer analysis (Kays 2005) yields an expression shown in Equation 2-11. Equation 2-11 is more accurate for $\mathrm{Pr} \geq 0.6$ and $\mathrm{Re}_D \leq 2{,}000$, because for low Re_D the boundary layer remains laminar at the front semi-sphere and no turbulent effect exists at stagnation point.

$$Nu_D(\theta = 0) = 1.15\,\mathrm{Re}_D^{1/2}\,\mathrm{Pr}^{1/3} \qquad 2\text{-}11$$

Experimental results for the variation of the local Nusselt number with θ are shown in Figure 2.3. For low Re_D ($\mathrm{Re}_D = 500$), maximal Nu is reached at stagnation point. The velocity boundary layer on the cylinder surface for low Re_D is a laminar boundary layer, which develops with the increase of θ, so the heat transfer coefficient decreases along the cylinder circumference. For the condition of $\mathrm{Re}_D \le 10^5$ (purple curves in Figure 2.3), Nu number decreases with increasing θ as a result of laminar boundary layer development. However, a minimum is reached at $\theta \approx 80^\circ$, where separation occurs and Nu number increase with θ due to mixing associated with vortex formation in the wake. In contrast, for $\mathrm{Re}_D \ge 10^5$ (blue curve in Figure 2.3), the variation of Nu number with θ is characterized by two minima. The decline in Nu number from the value at the stagnation point is again due to laminar boundary layer development, but the sharp increase that occurs between 80° and 100° is now due to boundary layer transition to turbulence. With further development of the turbulent boundary layer, Nu number again begins to decline. Eventually separation occurs ($\theta = 140^\circ$), and Nu number increases as a result of mixing in the wake region. The increase in Nu number with increasing Re_D is due to a corresponding reduction in the boundary layer thickness, which is indicated by the red curve in Figure 2.3. The transition from laminar boundary layer to turbulence occurs earlier at $\theta \approx 40^\circ$, resulting a sharp increase of Nu number. With the development of turbulent boundary layer, Nu number decreases with θ until the separation point $\theta = 140^\circ$, and then start to increase due to the mixing effect in wake region.

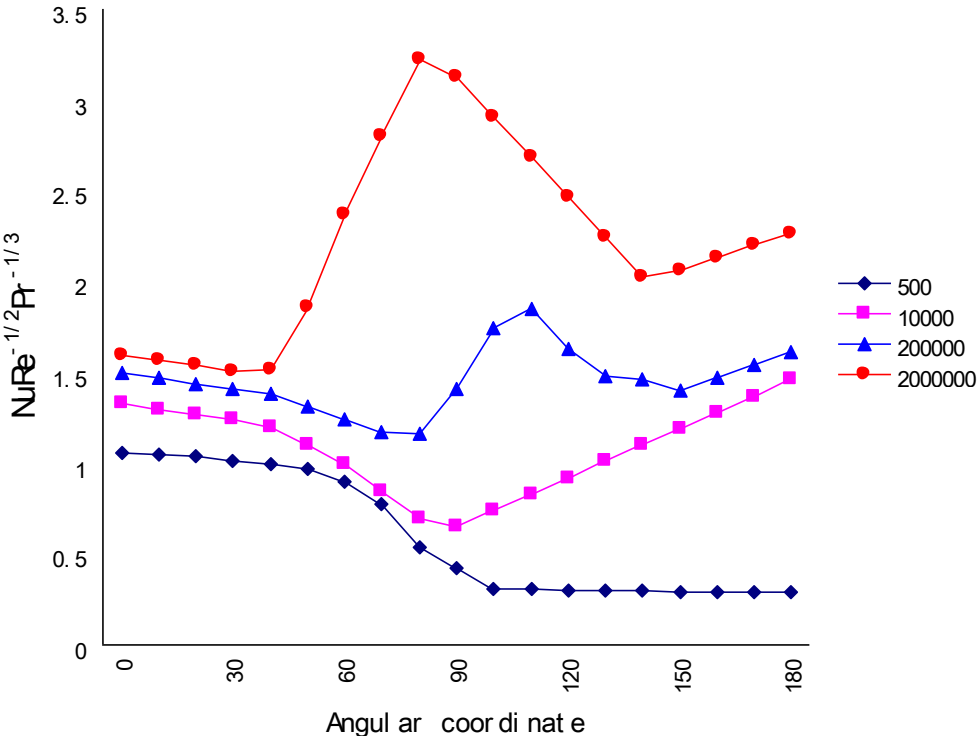

Figure 2.3 Local Nusselt number for flow over a circular cylinder

In most engineering projects, we are more interested in overall Nu from a circular cylinder in cross flow. One of empirical correlations is given by Hilpert (1933) as shown in Equation 2-12, and the condition for parameters shown in Table 2.1. The restriction of Pr in Equation 4-2 is $\Pr \geq 0.7$.

$$Nu_D = C \operatorname{Re}_D^m \Pr^{1/3} \qquad 2\text{-}12$$

Table 2.1 Constants for Equation 2-12

Re_D	C	m
0.4 - 4	0.989	0.330
4 - 40	0.911	0.385
40 - 4000	0.683	0.466
4000 - 40,000	0.193	0.618
40,000 - 400,000	0.027	0.805

Another correlation due to Churchill (1977) is shown in Equation 2-13. It covers the entire range of Re_D for which data are available, as well as a wide range of Pr. Although Equation 2-13 is applicable for all range of Re_D and Pr, it is recommended for $\mathrm{Re}_D\,\mathrm{Pr} \geq 0.2$.

$$Nu_D = 0.3 + \frac{0.62\,\mathrm{Re}_D^{1/2}\,\mathrm{Pr}^{1/3}}{[1+(0.4/\mathrm{Pr})^{2/3}]^{1/4}}[1+(\frac{\mathrm{Re}_D}{282000})^{5/8}]^{4/5} \qquad 2\text{-}13$$

$$\text{for } \mathrm{Re}_D\,\mathrm{Pr} > 0.2$$

The correlation due to Zukauskas is given in Equation 2-14, and the corresponding constants are listed in Table 2.2. If $\mathrm{Pr} \leq 10$, n=0.37; if $\mathrm{Pr} \geq 10$, n=0.36. Pr_s denotes the Prandtl number evaluated at cylinder surface.

$$Nu_D = C\,\mathrm{Re}_D^m\,\mathrm{Pr}^n(\frac{\mathrm{Pr}}{\mathrm{Pr}_s})^{1/4} \qquad 2\text{-}14$$

Table 2.2 Constants for Equation 2-14

Re_D	C	m
1 - 40	0.75	0.4
40 - 1000	0.51	0.5
10^3 - 2×10^5	0.26	0.6
2×10^5 - 10^6	0.076	0.7

Sanitjai and Goldstein (2004) experimentally investigated the forced convection heat transfer from a circular cylinder in cross flow to air and liquid for Reynolds number from 2000 to 90,000 and Prandtl number from 0.7 to 176. An empirical correlation was proposed for average Nusselt number around the cylinder, as shown in Equation 2-15.

$$Nu_D = 0.446\,\mathrm{Re}_D^{0.5}\,\mathrm{Pr}^{0.35} + 0.528[(6.5e^{\mathrm{Re}_D/5000})^{-5} + (0.031\,\mathrm{Re}_D^{0.8})^{-5}]^{-0.2}\,\mathrm{Pr}^{0.42} \qquad 2\text{-}15$$

It should be noted that each correlation is reasonable over a certain range of condition. For engineering calculations, we should not expect accuracy much better than 20%, because the correlations are based on recent results encompassing a vide range of conditions, such as Reynolds number, Prandtl number, blockage ratio, even cylinder surface conditions.

2.2.2 Oscillating cylinder in cross flow

It is evident from recent studies that transverse oscillation of a cylinder in cross flow will significantly enhance the heat transfer of the cylinder under certain conditions. The mechanism of this enhancement still remains unsolved. One of favorite explanations is that the wake structure is the key between oscillation and heat transfer. Different wake structure will result in totally different heat transfer around the cylinder. Williamson and Roshko (1988) studied wake structures under various oscillating conditions. Each wake mode corresponds to a number of vortices during one oscillation cycle. Basically, wake mode consists of single vortex (S) and a pair of counter-rotating vortices (P). More wake types, i.e. $2S$, $2P$ or $S+P$, may exist under different conditions. Williamson and Roshko defined a non-dimensional parameter, amplitude ratio A/D , for determining the wake mode. They also presented a region map for wake modes.

Sreenivasan and Ramachandran (1961) was one of the early researchers who experimentally studied on the heat transfer of transverse oscillating cylinder in cross flow. The test cylinder used in their experiment was 6 inches (0.152m) in length and 0.344 inch (0.0087m) in diameter. A thermocouple was inserted in the middle of the cylinder to measure the transient temperature variation. A crank system was used to vibrate the cylinder within the range from 200 to 2800 cycles/min. It was observed from the experiment that in the range $2500 < \mathrm{Re}_D < 15{,}000$, the heat transfer from the cylinder subjected to vertical vibration in cross flow remained unaffected when the ratio of vibration velocity to flow velocity varied from 4% to 20%. This result indicated that if the oscillation velocity was much smaller than flow velocity, no obvious enhancement on Nu_D could be observed.

Kezois (1966) pointed out that the heat transfer was enhanced by 20% for small amplitude ($0.02 < A/D < 0.075$) transverse oscillation when the oscillation frequency is close to Strouhal number. Strouhal number, St, is defined in Equation 2-16.

$$St = \frac{f_{St} D}{V} \qquad 2\text{-}16$$

Where f_{St} is the frequency at which vortices are shed, and can be obtained from the observation on wake flow structure. D and V are the cylinder diameter and flow velocity, respectively. It is noted that Kezois 's experiment is for very small amplitude ratio, meaning that the cylinder reciprocates over very short distance. Under this situation, the boundary layer shift with vibration is hard to be observed.

Saxena (1978) carried out the oscillating experiment by using a test cylinder of 74.6 mm in length, 22.2 mm in diameter, and 3.18 mm in thickness. A cartridge heater was fitted inside, and four thermocouples were equally spaced on the cylinder surface circumferentially. The Reynolds number in the experiment was 3500. The amplitude ratio varied from 0.89 to 1.99 and the oscillation frequency from 0.4 to 1.2 Hz. For the range of conditions, some local heat transfer coefficients were up to 60% larger during oscillation than when the cylinder was at rest, and the largest increase occurred on the back of the cylinder at the largest amplitude and frequencies. Saxena also reported that both amplitude and frequency contributed to the increase of heat transfer, being about equal influential.

Cheng (1997) utilized a modified transient test method and a flow visualization technique to determine the heat transfer coefficient and observe the flow pattern of transverse oscillation

cylinder in cross flow. The length and diameter of the test cylinder is 250mm and 16mm, respectively. The transient temperature of the cylinder was measured by three K-type thermocouples distributed at three different longitudinal locations along the cylinder. In the range of parameters $0 \le f \le 0.65, 0 \le A/D \le 0.628$, and $0 \le \mathrm{Re}_D \le 4000$, results showed that the heat transfer can be significantly increased by oscillation of the cylinder. A maximum of 34% increase in heat transfer was observed within the parameter ranges. Cheng also suggested that two types of effects, namely, the lock-on effect and the turbulent effect, might contribute to the enhancement of heat transfer. For a cylinder oscillating at low frequency and amplitude in low Reynolds number flow, heat transfer was enhanced only in lock-on regime. If the oscillation parameters and Reynolds number were sufficiently high, heat transfer might be influenced by the turbulence effect resulting from higher relative velocity between the fluid and the cylinder.

Gau (1999) performed a series of experiments to study the flow structure and heat transfer over a heated oscillating cylinder. A Bakelite test cylinder, with 300 mm in length, 30 mm in outside diameter, and 3 mm in thickness, was selected to reduce the radial and circumferential heat conduction effect. Reynolds number varies from 1600 to 4800, and amplitude ratio A/D from 0.064 to 0.016. The excitation frequencies of the cylinder were selected at $F_c/F_n =$ 0, 0.5, 1, 1.5, 2, 2.5, and 3, where F_c and F_n were frequencies of the cylinder oscillation and vortex shedding. Gau reported that synchronization of vortex shedding with the cylinder excitation occurs at $F_c/F_n = 1$ and $F_c/F_n = 3$, where the heat transfer is greatly enhanced. Gau also pointed out that the enhancement in the heat transfer is proportional to the magnitude of the excitation frequency. Gau's study was a breakthrough because he found that resonance of cylinder oscillation and vortex shedding might result in the enhancement of heat transfer, not limited to one-frequency enhancement (when f close to Strouhal frequency) reported by previous researchers.

Gau's conclusion was proved by Park (2001). Park performed a experiment to examine the effect of forced transverse oscillation on heat transfer for $\mathrm{Re}_D =$ 550, 1100, 3500, and amplitude ratio $A/D =$ 0.1 and 0.2. It is found that there is a large increase in heat transfer at about three times the unforced vortex shedding frequency for $A/D =$ 0.1, and there are large increase in heat transfer at two and three times the frequency for $A/D =$ 0.2. Digital particle

image thermometry / velocimetry (DPIT/V) was employed by Park, and showed that the heat transfer enhancement was correlated with a shortening of the vortex roll-up distance.

Pottebaum (2006) performed similar experiments as Park by using DIPT/V to investigate synchronization of frequencies (heat transfer enhancement), formation length, wake mode, and transverse velocity from a oscillation cylinder in cross flow. Oscillation frequency f, amplitude ratio A/D, wake mode (P, S etc) were considered as variables, which might be possible to affect the heat transfer. The range of frequency f was from 0.066 to 1.082, amplitude ratio A/D from 0 to 1 with 0.05 of increment. The Reynolds number was 687 for all cases. It was reported by Pottebaum that (1) heat transfer is significantly enhanced by small amplitude oscillation at frequencies near the Strouhal frequency and its harmonics for amplitude ratio A/D < 0.5; (2) vortex roll-up process in the cylinder wake could affect the heat transfer coefficient significantly; (3) the transverse velocity was found the primary factor for variation of heat transfer coefficient. Pottebaum's results agreed Park (2001)'s results in low Reynolds number range, but showed more details on variation of heat transfer coefficient with different amplitude ratios A/D.

2.2.3 Axially assigned cylinder in cross flow

The problem of axially assigned cylinder in cross flow is very complicated. This problem, which is shown in Figure 2.4, can be analog to the problem of the flow over a blunt flat plate. There are some studies on the flow separation and reattachment phenomenon from a blunt flat plate in cross flow by Kiya (1983), Sheridan (1997) and Mills (2002) etc. Sheridan (1997) and Mills (2002) also investigated interaction between the leading-edge shear layer and the trailing-edge vortex shedding. However, only a few studies were found to investigate an axially assigned circular cylinder of a fixed length to diameter ratio (fineness ratio) in cross flow. The previous studies focused on the flow field of axially assigned cylinder in cross flow, not on the heat transfer of the cylinder. Because the heat transfer is highly correlated to the boundary layer and wake mode of the flow, but no agreement is reached on the flow field from previous studies. For flow field study, Ota (1975) used flow direction probe, hot wire and Pitot tube to measure the mean flow field within the separation bubble and in the boundary layer on a cylinder of fineness ratio 10. Kiya (1991) used a split film, hot wire probe and pressure transducer to

measure the separation and reattaching flow. A cellular structure in the reattachment region was found, and the variation of the drag coefficient for different fineness ratios were also calculated and plotted.

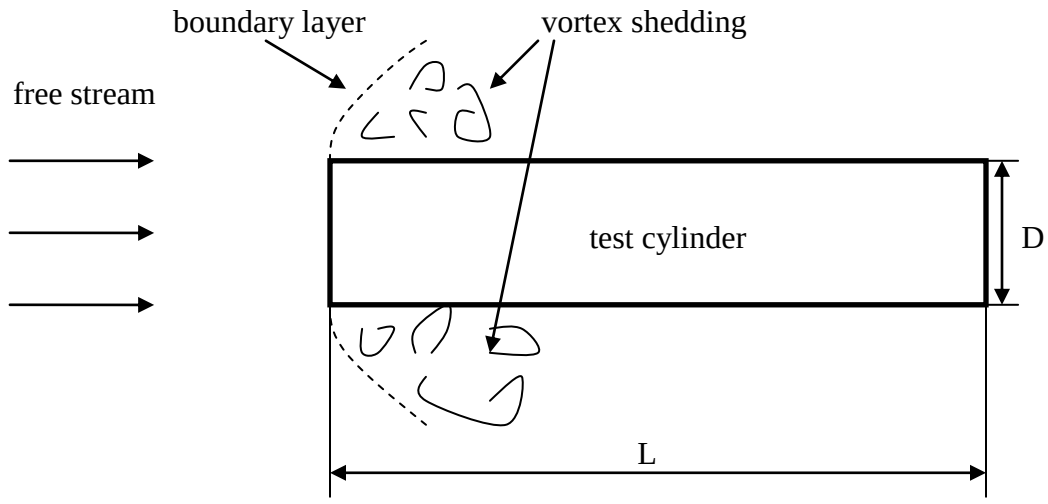

Figure 2.4 Illustration of axially aligned cylinder in cross flow

Higuchi (2006) reported a flow field analysis from an axially assigned cylinder in cross flow. The experiments were performed in water and air to observe the overall wake structure, the leading-edge shear layer and reattachment phenomena. For the experiment in air, a magnetically suspended model was initiated. As the primary influential factor, fineness ratio (L/D) was selected at 0.67, 1.5, and 3.0. It is indicated by experiments that for both L/D = 1.5 and 3.0, the separated leading edge shear layer reattached at approximately the same location, and a large scale of vortex motion was found just beyond the reattachment point. The recirculation region decreased from L/D = 0.67 to L/D = 1.5. The recirculation region for L/D = 3.0 was similar to that for L/D = 1.5, but the vortex shedding in the wake was significantly reduced.

Although no heat transfer results are reported for axially assigned cylinder in cross flow, velocity field of the flow is presented by some researchers. An agreement is reached that fineness ratio L/D is the dominant factor for the velocity field and wake mode. Therefore, the heat transfer is also strongly correlated to fineness ratio L/D.

2.2.4 Experimental investigation on the moving human

Danielsson (1993) investigated the convective heat transfer in clothing air layer of the human body. Convection coefficient and air speed at the external and internal air layers of a clothed human were studied for combinations of walking and wind speeds. A human subject was walking on a treadmill in the wind tunnel with the dimension of 1.7m (width), 2.4m (height), and 7.2m (length). Two large fans, one above the other, drew air through the tunnel. The operation wind speed of the wind tunnel was from 0 to 3m/s. The turbulence level of the wind tunnel was about 13% and 7% at 0.9m/s and 1.9m/s, respectively, which was measured by a hot wire anemometer. The clothing ensemble consisted of boots, stockings, briefs, trousers and jacket. The measuring sites for the heat flux and the air speed sensors were upper trunk, mid trunk, lower trunk, upper arm, lower arm, thigh, and lower leg. For the external heat convection measurements, each part of the body was investigated at eight points around the perimeter, distributed to cover the various angles to the wind.

For external convection coefficient, Danielsson conducted four experiments: the human subject standing in still air, standing in a wind, walking in still air, and walking in a wind. The first experiment was for natural convection investigation, and other three experiments studied forced convection. All signals from the temperature and heat flux sensors were recorded every 20 seconds, and the measurements were averaged over each minute. The results were reported as the mean value of the previous five minutes. Heat convection measurements were performed for the above four activities. To avoid condensation in the clothing layer, the environmental temperature was kept at 14.5°C, and each walking period was preceded by ten minutes of standing still. It was found that quasi-stationary conditions of clothing layers were reached within two minutes. The walking and wind speed used for experiments were 0.9, 1.4, and 1.9m/s.

The local convective heat transfer coefficients were reported for monitored body parts with different angles for all cases. The results of clothed human were compared to the data of nude body reported in literature. Among four cases, we are interested in two cases: human standing in a wind and walking in a wind, because our experiment is to study a moving cylinder in cross flow. Figure 2.5 and 2.6 show the convection coefficients of lower arm for a human standing in a wind and walking in a wind, respectively. The reason for choosing lower arm is

because the pivotal movement of a cylinder in our experiment is similar to the movement of swinging upper arm. It can be seen that the convection coefficient reaches maximal at stagnation point (0°), and decreases with the increasing of angle. At 140° to 180° position, the convection coefficient begins to slightly increase due to the separation of boundary layer.

Danielsson (1993) presented local convection coefficients for the moving human experimentally. These data could be compared to the results from our cylinder experiment, although some conditions of these two experiments were different. The comparison of results will be discussed in later chapters.

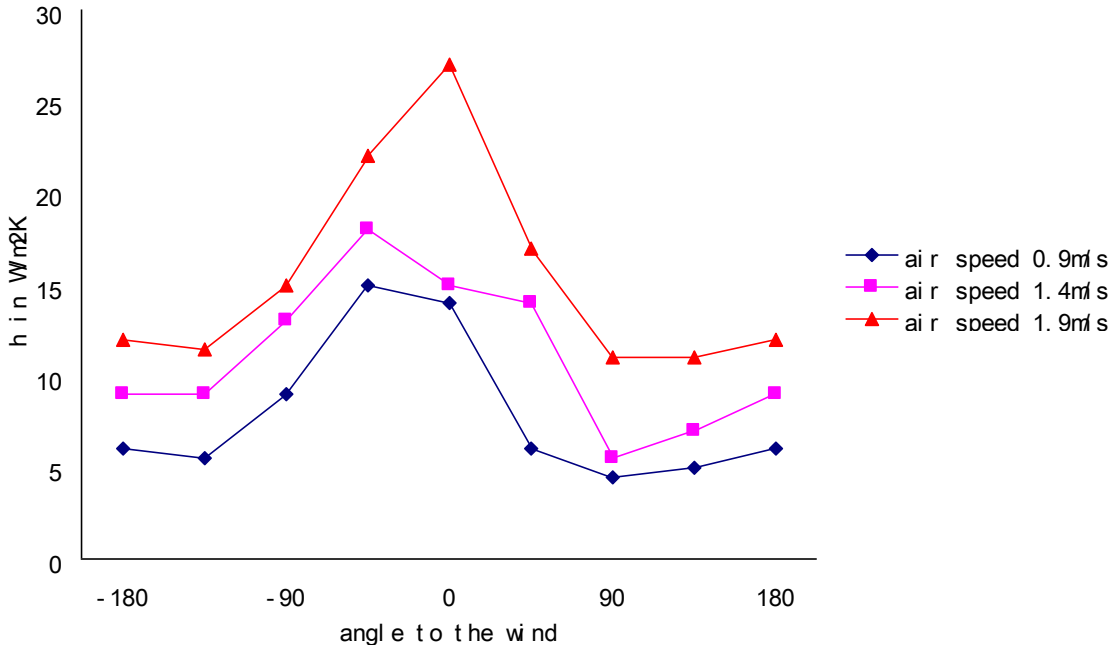

Figure 2.5 Convection coefficient of lower arm for standing human in a wind

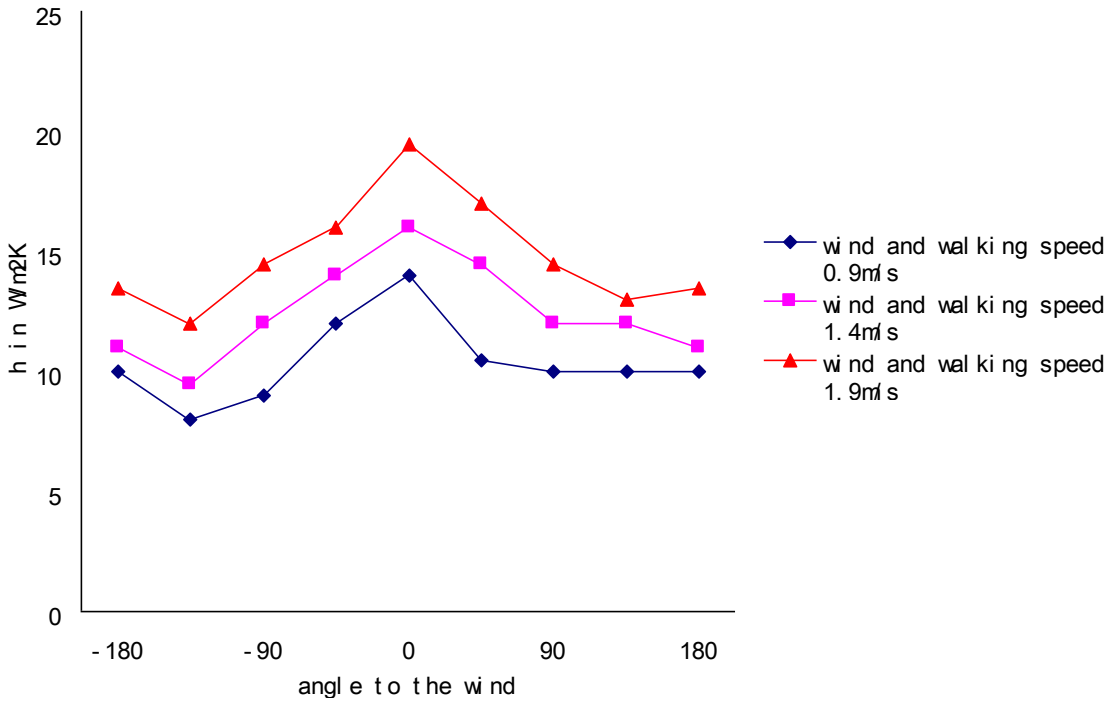

Figure 2.6 Convection coefficient of lower arm for walking human in a wind

Chapter 3 - Model development and solution method

In this chapter, a mathematical human thermal model will be introduced. The human thermal model consists of body model and clothing model. The body model simulates heat and mass transfer inside the body, and the heat and mass exchange between the human body and environment. Our body model is based on Smith's mathematical model, but allowing specified geometry of human body. In addition, more elements are used in our model, resulting in a better resolution of temperature contour of the human body. The clothing model used in this study is from Fu's clothing model (1995). No primary change has been made for clothing model, except that the local convective heat transfer coefficients over skin surface can be read from the data file, instead of constant convective heat transfer coefficients used in Fu's clothing model. In the next section, we introduce our model in three components: geometry, passive system, and controlling system, then the solution method to the differential equations for the passive systems is presented.

3.1 Body model

An integrated human thermal model consists of a geometry representation, passive system, and controlling system (called control system in Smith model). Geometry is a vital part of the body model, because it is a direct description of the human body. A geometry representation of real body shape is presented in terms of base elements. Each element is assigned with a specific element type, i.e. muscle, bone, blood vessel. Characteristics of these elements, such as element shape, surface area, and element volume, will be discussed through mathematical derivation. The controlling system refers to those body mechanisms, such as vasomotor, sudomotor, and shivering responses, which attempt to regulate heat and mass transfer of the passive system. These mechanisms are related to physiological issues of the human body, and can be considered as "driving force" for the heat and mass transfer inside the human body. The passive system is such a system which is affected by controlling system. The passive system determines the heat and mass transfer among tissue elements, blood vessels, respiratory tracts,

and the ambient environment. To develop the body model, we need to study on the physiological correlations for the controlling system, and then build the heat and mass transfer equations for the passive system.

3.1.1 Geometry representation

It is difficult to represent the human body because of its irregular shape and complicated structure of tissues and organs. As discussed in the introduction, the models of Gagge (1971), and Stolwijk (1970) models are lumped parameter models, using bulk properties, i.e. bulk temperature, for individual parts or segments, making these models unable to calculate temperature distribution throughout the body. Wissler (1985) and Smith (1991) used the finite element method to model body parts. As shown in Figure 3.1, Smith used 15 cylinders to represent 15 major body parts, just as Wissler did, and then divided each part into several elements in axial, angular, and concentric directions. Smith's model gave a close estimation of temperature distribution of the human body when the simulation results were compared with Hardy (1966), Hall (1969), and Saltin's (1966) experimental results. However, Smith's model is also limited to cylindrical body segments and not all parts of the body can be represented by strict cylindrical shapes.

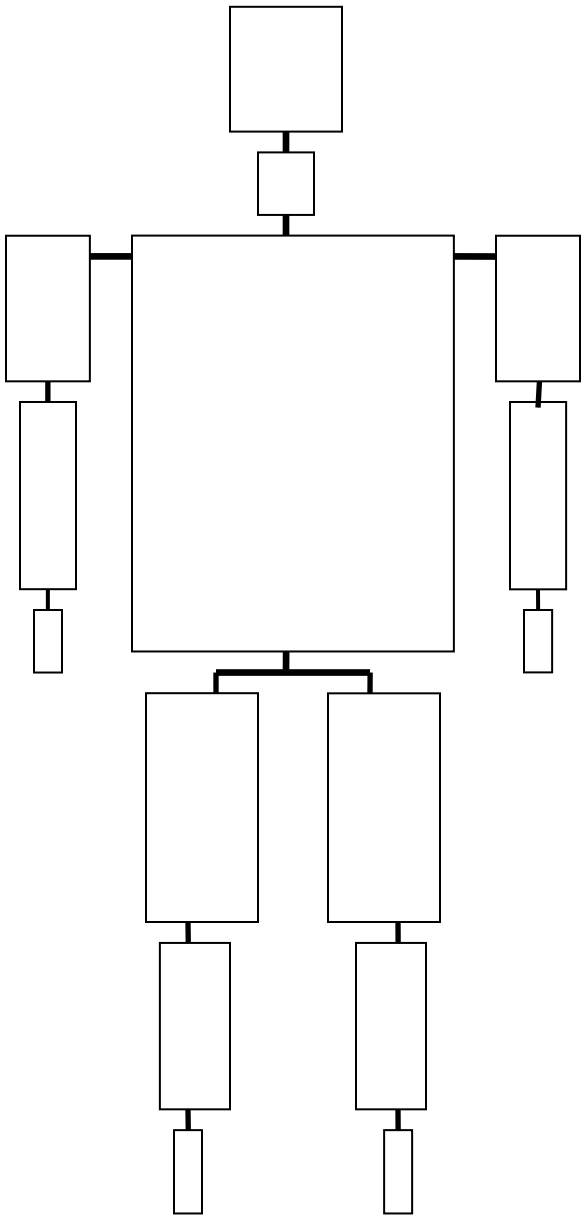

Figure 3.1 Fifteen body parts in Smith's model

The current model is based on finite element method (FEM). The reasons for choosing FEM are because (1) FEM is an accurate method to solve partial differential equations (2) FEM is better in handling complicated domain geometries of heat conduction and low-speed fluid problems in the human body (3) FEM can deal with domain changes (with moving boundaries), which will be one of our future issue for the simulation of moving human body. Like the Smith

model, the human body was divided into 15 parts, but the parts were no longer limited to cylindrical shapes. Figure 3.2 shows our shaped body parts compared to previous cylindrical body parts in Figure 1. Figures 3.3 and 3.4 show a layout of the upper arm and two types of elements, respectively. The cylinder was angularly divided into four slices, and the angle for each slice was 90°. Generally, the shape of a segment was described by a series of radius (i.e. r_1 - r_4 in Figure 3.3b), and all of these radius data were stored in a pre-set shape-description file. Therefore, it was possible to change the shape of body segments for individuals, who had different body shapes, just by changing the radius data in this pre-set file. For each simulation, this shape-description file was read as input, and all parameters and dataset arrays concerning body shape were recalculated or updated for this case.

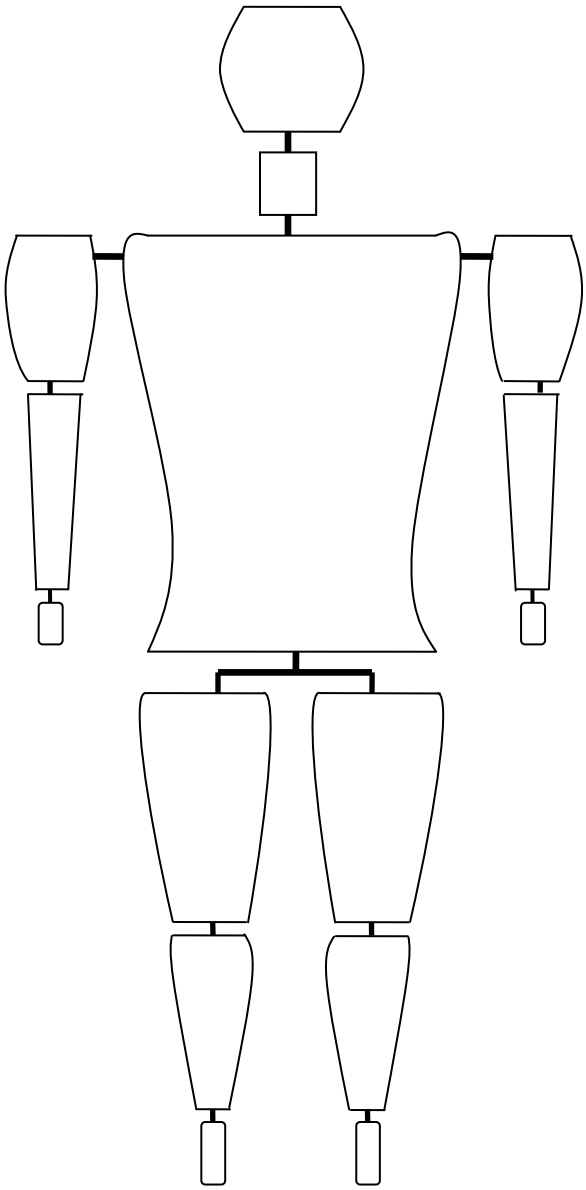

Figure 3.2 Shaped human body in our model

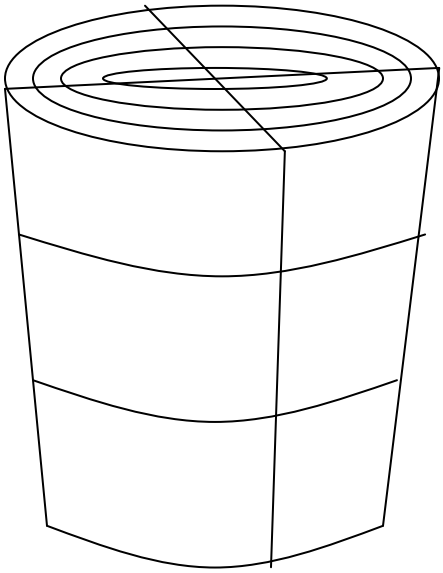

Figure 3.3a Layout of upper arm

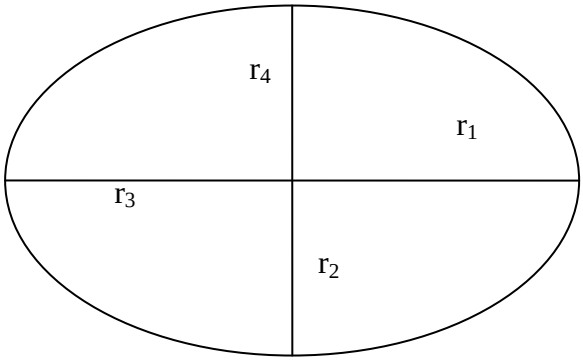

Figure 3.3b Cross-section of upper arm

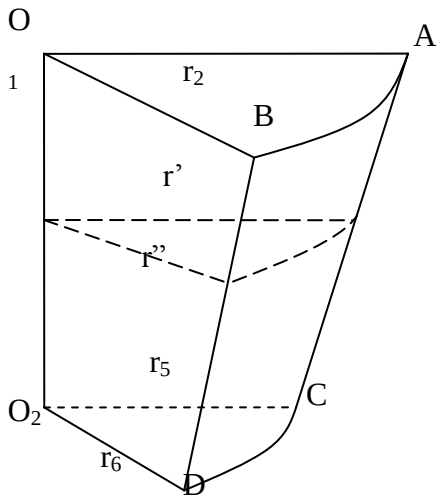

Figure 3.4a Triangular 3-D element

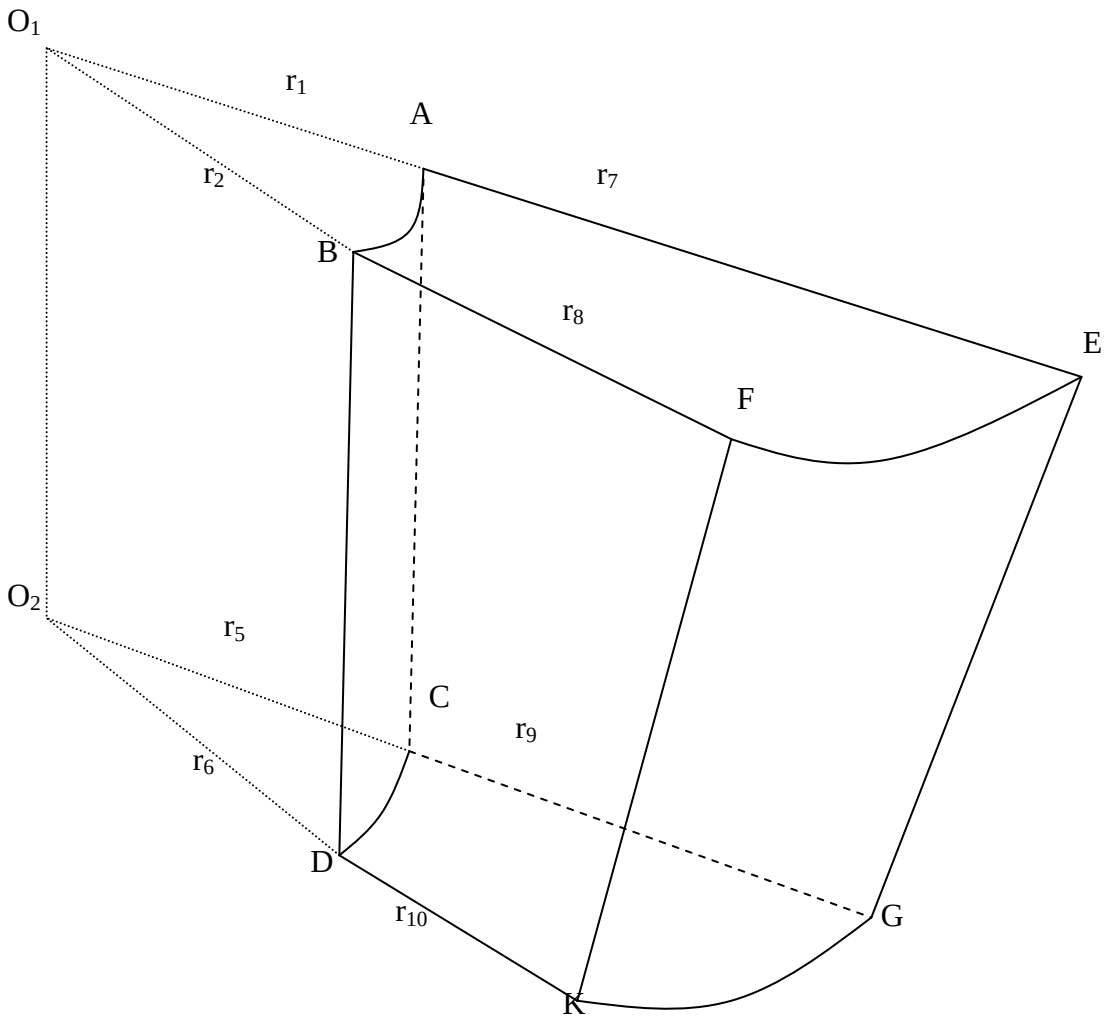

Figure 3.4b Rectangular 3-D element

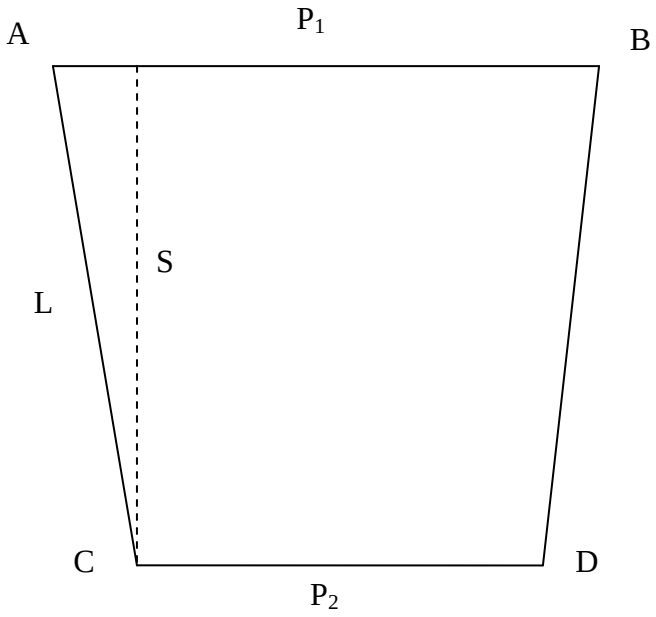

Figure 3.5 Approximation of 3-D surface in upper arm element

Since our model was based on the finite element method, surface area and volume of each element needed to be evaluated, as shown in Figure 3.4a and 3.4b. It was assumed that (1) curve AB was an ellipse with r_1 and r_2, (2) curve CD was an ellipse with r_5 and r_6, (3) on any cross-section of the element, the curve was ellipse (Figure 3.4a), (4) the curved surface A-B-C-D was continuous and smooth. There are two types of 3-D element. The triangular 3-D element (element I) in Figure 3.4a is located in the center of the segment, representing core substance, i.e. bone or brain. The rectangular 3-D element (element II) in Figure 3.4b denotes other elements outside the core elements, for example, muscle, fat, and skin. The skin elements include top, bottom, and lateral surfaces of the elements. By noting that angle A-O1-B is 90°, the top or bottom surface area can be determined by

$$A_s = \frac{1}{4}\pi r_1 r_2 \qquad \text{for element I} \qquad 3\text{-}1$$

$$A_s = \frac{1}{4}\pi (r_7 r_8 - r_1 r_2) \qquad \text{for element II} \qquad 3\text{-}2$$

The lateral surface area needs to be calculated for outside element (element II) in Figure 3.4b. By assumptions (1) - (4), the lateral surface area (3-D) can be approximated as a 2-D surface as shown in Figure 3.5. P_1 and P_2 are perimeters of quarter ellipses EO1F and GO2K. A good approximation to ellipse perimeter was given by Ramanujan (1913) as follows

$$P_1 = \frac{1}{4}\pi[3(r_7 + r_8) - \sqrt{(r_7 + 3r_8)(3r_7 + r_8)}] \quad 3\text{-}3$$

$$P_2 = \frac{1}{4}\pi[3(r_9 + r_{10}) - \sqrt{(r_9 + 3r_{10})(3r_9 + r_{10})}] \quad 3\text{-}4$$

The lateral surface area in Figure 3.5 can be given by

$$A_s = \frac{1}{2}S(P_1 + P_2) \quad 3\text{-}5$$

Where S is vertical height of trapezoid EFKG in Figure 3.5.

To approximate S, we assumed circle shape for top and bottom surfaces, that was, $r_7 = r_8$ and $r_9 = r_{10}$. So vertical height S was expressed in terms of side length L as

$$S = \sqrt{L^2 - (\frac{P_1 - P_2}{2})^2} \quad 3\text{-}6$$

Where L can be obtained from geometrical calculation as

$$L = \sqrt{H^2 + (r_7 - r_9)^2} \quad 3\text{-}7$$

When applying to general cases (arbitrary $r_7 - r_{10}$), it is a good approximation to replace r_7 and r_9 in Equation 3-7 with average radius $\frac{r_7 + r_8}{2}$ and $\frac{r_9 + r_{10}}{2}$, respectively, yielding

$$L = \sqrt{H^2 + (\frac{r_7 + r_8}{2} - \frac{r_9 + r_{10}}{2})^2} \quad 3\text{-}8$$

By substituting Equation 3-3, 3-4, 3-6, and 3-8 into Equation 3-5, lateral surface area can be calculated for every surface element.

The element volume was calculated for two types of element respectively. Note that $r_7 - r_{10}$ were also radius from the center point to the edge. Yet by assumptions (1) - (4), the element volume can be obtained by the following integral

$$V = \int_{h=0}^{H} Adh \quad 3\text{-}9$$

Where A is the cross-section area of the element, H is height of the element.

Equation 3-9 is the general formula to calculate element volume. It is also assumed in our model that the cross-section has a linear change from top surface to the bottom one, so the radius on any cross-section can be calculated by applying linear interpolation of two radii on top and bottom surfaces, as shown in Equation 3-10 and 3-11.

$$r' = r_1 + (r_5 - r_1)\frac{h}{H} \qquad 3\text{-}10$$

$$r'' = r_2 + (r_6 - r_2)\frac{h}{H} \qquad 3\text{-}11$$

Where r', r'' are radius of arbitrary cross-section shown in Figure 3.4a, and the elliptic cross-section area can be calculated as

$$A = \frac{1}{4}\pi r' r'' \qquad 3\text{-}12$$

By substituting Equation 3-10, 3-11, and 3-12 into Equation 3-9 and integrating, the element volume for triangular and rectangular elements can be obtained as shown in Equation 3-13 and 3-14.

$$V = \frac{1}{12}\pi H(r_1 r_2 + r_5 r_6 + \frac{1}{2}r_2 r_5 + \frac{1}{2}r_1 r_6) \quad \text{for element I} \qquad 3\text{-}13$$

$$V = \frac{1}{12}\pi H(r_7 r_8 + r_9 r_{10} + \frac{1}{2}r_8 r_9 + \frac{1}{2}r_7 r_{10} - r_1 r_2 - r_5 r_6 - \frac{1}{2}r_2 r_5 - \frac{1}{2}r_1 r_6)$$

for element II 3-14

It should be noted that Equations 3-5, 3-13, and 3-14 are based on mathematical approximation, and are capable of obtaining relatively accurate results as long as the body parts are not "extremely irregular", which means the shape of top and bottom surfaces is roughly similar and the lateral curved surface is not twisted. In reality, most body parts of a human are continuous and smooth, except the hand and foot, so Equations 3-5, 3-13, and 3-14 are applicable to those parts. The irregular parts, hand and foot, are still treated as “cylinders” for the sake of simplicity.

3.1.2 Passive system

According to Smith's model, with the element area A_s and the element volume V, an energy balance equation can be written for any tissue element in Figures 3.4a and 3.4b:

$$\rho c_p \frac{\partial T}{\partial t} = k\vec{\nabla}^2 T + \frac{q'}{V} \qquad 3\text{-}15$$

Where the term on the left-hand side of Equation 3-15 is heat storage in element, the first term on the right-hand side is heat conduction throughout this element, and the second term is heat generation rate (J/m^3) in tissue, The solution method for Equation 3-15 will be discussed in the next section.

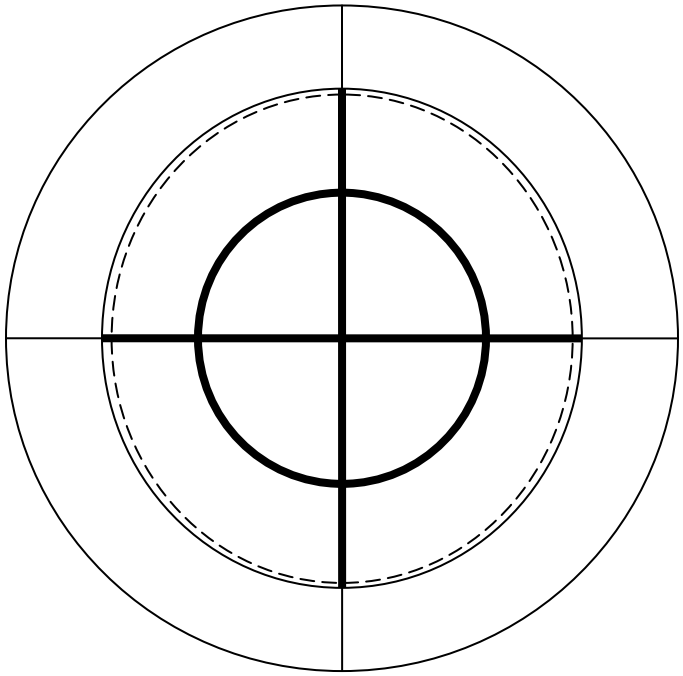

Figure 3.6a. Top view of vascular network for upper arm

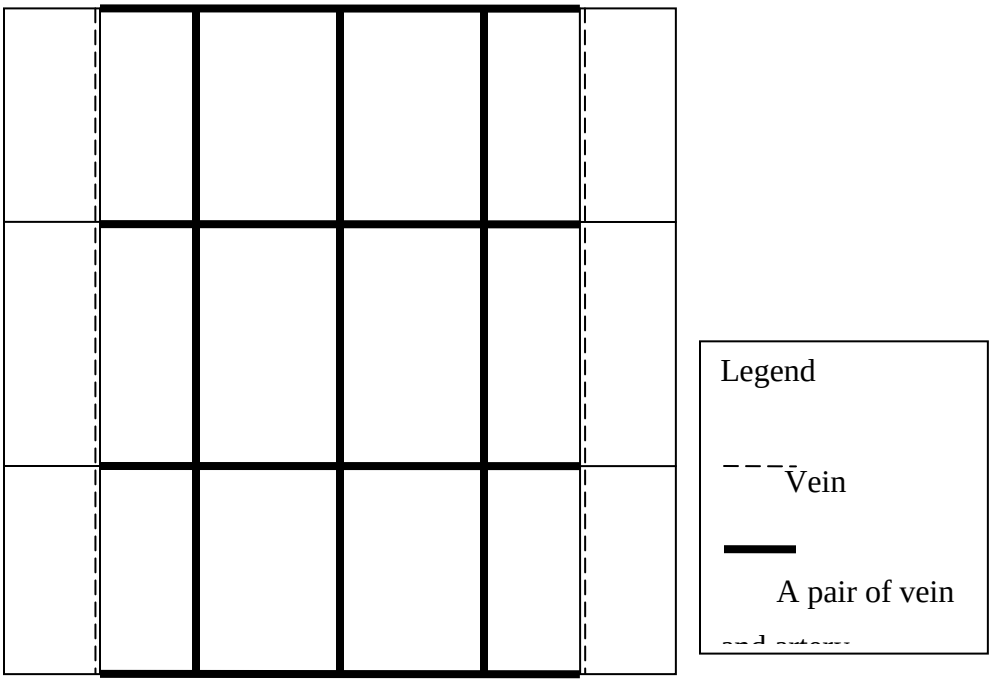

Figure 3.6b. Cross-section view of vascular network for upper arm

The circulatory system was modeled as a network of blood vessels – veins and arteries, as was also done by Smith (1991). Figures 3.6a and 3.6b illustrate blood vessel distribution in the upper arm. A pair of blood vessels (one artery and one vein) was assigned between two adjacent nodes of the element, except for the nodes of the skin elements, since there were only superficial veins on the skin. In this work, blood vessel elements were considered 1-D elements for simplicity. Blood originated from the left ventricle, flowing everywhere through arteries, exchanging mass and nutrition with tissue, then returning to the right atrium through veins. An energy balance can be built for any blood vessel element as

$$\rho c_P \frac{\partial T}{\partial t} = k \frac{d^2 T}{dz^2} - \rho c_P v_{bl} \frac{dT}{dz} \qquad 3\text{-}16$$

In Equation 3-16, v_{bl} is mean blood velocity, which depends on cardiac output, blood pressure, and blood radii. ρ, c_p, and k are density, specific heat, and thermal conductivity of blood, respectively.

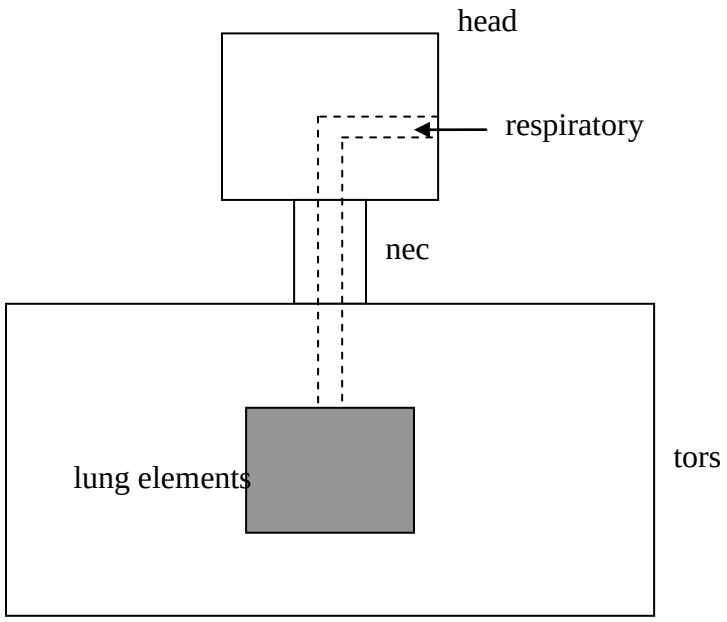

Figure 3.7 Schematic of respiratory system

The respiratory system was modeled as an inhale-exhale tract as shown in Figure 3.7. Similar to the blood vessel element, respiratory tract elements were also 1-D elements. For any given tract element, the energy equation was written as

$$\rho c_P \frac{\partial T}{\partial t} = k \frac{d^2 T}{dz^2} - \rho c_P v_{resp} \frac{dT}{dz} \qquad 3\text{-}17$$

Equation 3-17 has the same form as Equation 3-16, except that air velocity v_{resp} was substituted for blood velocity v_{bl}. ρ, c_p, and k are the same properties of the air. To solve Equation 3-16 and 3-17, blood velocity v_{bl} and air velocity v_{resp} needed to be evaluated. The method to obtain v_{bl} and v_{resp} will be discussed in Section 3.3.

3.1.3 Controlling system

As discussed in the last section, there were three types of elements in our model: tissue, blood vessel, and respiratory tract. Tissue elements were 3-D. All body tissue and organs, such as bone, muscle, fat, skin, brain, lung, etc., were modeled as tissue elements. Blood vessel and

respiratory elements were 1-D. Equations 3-15 was written for 3-D tissue elements, and the properties were obtained for different tissue types. The heat generation, $\frac{q'}{V}$, was a summation of three effects: metabolic rate, physical activity level, and shivering, and can be expressed as

$$\frac{q'}{V} = M_{basal} + M_{activity} + M_{shivering} \qquad 3\text{-}18$$

The basal metabolic generation M_{basal} were obtained from the work of Charney (1987), Ganong (1983), and Gordon (1974), shown in Table 3.1. The metabolic generation due to physical activity, $M_{activiy}$, is shown in Table 3.2, from the work of Benzinger (1970). The metabolic generation due to shivering, $M_{shivering}$, was also calculated from Benzinger's work.

Table 3.1 Basal metabolic heat generation rate of different tissues

Tissue Type	Basal Metabolic Heat Generation Rate, J/100g min
brain	76.15
abdomen	23.00
lung	4.03
bone	0
muscle	4.03
fat	0.024
skin	6.03

Table 3.2 Typical metabolic generation rate for various activities

Activity	Metabolic Generation (W/m2)	Met*
sleep	40	0.7
seated	60	1.0
walking (0.9m/s)	115	2.0
calisthenics	175	3.0
heavy machine work	185	4.0
basketball	290	5.0

Source: ASHRAE handbook -Fundamentals (2005)

* 1 MET = 58.1 W/m^2

In Equation 3-16, mean blood velocity v_{bl} needs to be determined for every blood vessel element. The blood flow in circular vessels can be considered as a pressure-driven flow problem, which was described in the Hagan-Poiseuille problem. The mean blood velocity can be expressed in terms of pressure gradient, $-\frac{dP}{dz}$, in Equation 3-19. By assuming (1) blood flow is continuous and steady, and (2) cross-section of blood vessel remains constant along any 1-D blood vessel element, Hagan-Poiseuille problem reduces to Equation 3-20. With the proper boundary conditions, $-\frac{dP}{dz}$ can be solved from Equation 3-20, and then substitute back into Equation 3-19 to obtain v_{bl}.

$$v_{bl} = \frac{-r_0^2}{8\mu}\frac{dP}{dz} \qquad 3\text{-}19$$

$$\frac{-r_0^2}{8\mu}\frac{d^2P}{dz^2} = 0 \qquad 3\text{-}20$$

Equation 3-17 is an energy balance equation for the respiratory tract element. In addition, the mass balance equation needed to be established in terms of the humidity ratio, w_{air}, which is

defined as the quantity of water vapor in a mixture relative to the amount of dry air present. For any respiratory tract element, the mass balance equation is written as

$$D\frac{d^2W}{dz^2} - v_{resp}\frac{dW}{dz} = 0 \qquad 3\text{-}21$$

Where D is the constant diffusivity of air. The air velocity, v_{resp}, can be calculated from the oxygen consumption rate as shown in Equation 3-22.

$$v_{resp} = \frac{\dot{V}_{O_2}}{\pi r_0^2} \qquad 3\text{-}22$$

ASHREA Handbook (ASHREA 2005) gives a correlation of $\dot{V}_{O_2}$ in terms of metabolic generation as

$$\dot{V}_{O_2} = \frac{M}{21.12(0.23RQ + 0.77)} \qquad 3\text{-}23$$

RQ is called respiration quotient, varying between 0.7 for light work and 1.0 for heavy work.

3.2 Clothing model

The clothing model, used in our simulation, was developed by Fu (1995). Fu's model has the following advantages: (1) simulates both heat and mass transfer , and provides history of temperature and humidity gradient on clothing surface (2) takes many phenomena into consideration, such as non-flat cloth, mass transfer in fabric interstices, fiber adsorption, etc (3) is able to handle multiple clothing ensembles, i.e. hat, scarf or vest. This transient model also allows users to create new clothing ensembles by combining different fabrics. In order to simulate clothing used in Zhang's experiment (Zhang 2003), we created a new "leotard ensemble" by combining dimensions and thermal properties of leotard fabric. The insulation values for each body part were from Zhang's report. Detailed information about leotard ensemble used in the model is included in Appendix A.

3.2.1 Heat and Mass transfer in clothing model

In Fu's clothing model (1995), clothing surface is discretized into small pieces (elements),

and differential equations are written for each element. Mass transfer is the dominant phenomenon in clothing model because heat transfer amount is highly dependent on mass transfer rate. There are other factors which contribute to heat transfer, such as heat conduction, heat convection, adsorption, condensation, etc, but in usual condition they are negligible, if compared to the heat transfer due to the mass transfer. The reason is that the latent heat for evaporation is much higher than heat transfer from other phenomenon. To derive mass transfer equation, Fu combined Henry (1939) and Jones' (1993) theories. Henry (1993) considered moisture concentration as the driving force in mass transfer, while Jones took vapor pressure as driving force. Fu's model used "real" driving force: chemical potential of vapor, shown in Equation 3-24.

$$J = -Bc\frac{\partial \mu}{\partial x} \qquad 3\text{-}24$$

where J is mass transfer rate, B is mobility, μ is chemical potential, and c is moisture concentration. To find the derivative of chemical potential of water vapor, an assumption is made as following: the water vapor is treated as ideal gas, if the temperature and pressure of water vapor is not too high. This assumption is always reasonable for the human model because the temperature and pressure of vapor around human body are always within normal range. Thus, the ideal gas equation for water vapor can be written as

$$\mu = \mu^0 + R_{H_2O}TLn(P/P^0) \qquad 3\text{-}25$$

where R_{H_2O} is gas constant, T and P are temperature and pressure, respectively, μ^0 and P^0 are chemical potential and pressure at reference point (0℃ or 20℃). In Equation 3-25, take derivative with respect to x on both sides, gives

$$\frac{\partial \mu}{\partial x} = R_{H_2O}[Ln(P/P^0)\frac{\partial T}{\partial x} + \frac{T}{P}\frac{\partial P}{\partial x}] \qquad 3\text{-}26$$

The temperature gradient along the clothing layers has been proved negligible, so $\frac{\partial T}{\partial x}$ vanishes. Substitute ideal gas relation $\frac{T}{P} = \frac{1}{R_{H_2O}c}$ into Equation 3-26 yields

$$\frac{\partial \mu}{\partial x} = \frac{1}{c}\frac{\partial P}{\partial x} \qquad 3\text{-}27$$

Equation 3-27 implies that both pressure and concentration are driving forces because

they have a simple multiplication relation to the chemical potential. Equation 3-27 can be used if temperature gradient is negligible. In some condition that the temperature along the cloth can not be neglected, the complete expression of Equation 3-26 need to be utilized.

The validation of chemical potential is done in Equation 3-27. With the consideration of cylindrical geometry of human body, moisture adsorption in air gap, and diffusion effect from condensation, transient 1-D heat and mass transfer equations can be written in cylindrical coordinates as following:

$$\rho_{fab}\frac{\partial R}{\partial t}+\varepsilon_{fab}\frac{\partial c}{\partial t}=\frac{t_{fab}}{R_{d,fab}}\left(\frac{1}{r}\frac{\partial P}{\partial r}+\frac{\partial^2 P}{\partial r^2}\right) \qquad 3\text{-}28$$

$$C_{P,fab}\rho_{fab}\frac{\partial T}{\partial t}=\frac{t_{fab}}{R_{d,fab}}\left(\frac{1}{r}\frac{\partial T}{\partial r}+\frac{\partial^2 T}{\partial r^2}\right)+\rho_{fab}(\Delta H)\frac{\partial R}{\partial t} \qquad 3\text{-}29$$

where subscription "fab" denotes properties for fabrics. Equation 3-28 is the mass transfer equation. The left hand side of the Equation 3-28 denotes the mass of water (vapor) stored on the clothing surface, while the right hand side denotes the mass gradient along the fabrics due to the driving force -- chemical potential. Equation 3-29 is 1-D transient energy equation, which combines heat conduction and condensation effects, corresponding to the two terms in the right hand side, respectively. The boundary conditions for Equation 3-28 and 3-29 are from the simulation results of body model on skin side and environment condition on clothing surface. The mass and energy equation can be solved by numeric method.

3.2.2 Fiber adsorption

The term $\frac{\partial R}{\partial t}$ in Equation 3-29 is an overall effect of the fiber adsorption, film resistance, and heat generation in fiber. According to Fu's literature research, this process is very complicated because they have effect on each other. Since the primary goal of this paper is to develop a shaping model, no more work has been done to Fu's clothing model. For more information, please refer to Fu's thesis (Fu 1995).

3.3 Solution method

Passive system equations were shown in last section. The finite element technique, which was described in Segerlind's book (Segerlind 1984), was used to solve the differential equations for the passive system. To discretize governing equations which have first-order or higher derivatives, Galerkin's method of weighted residual was applied to PDEs of pressure in Equation 3-20, humidity ratio Equation 3-21, and temperature distribution Equation 3-15.

For pressure distribution in Equation 3-20, Galerkin's method was applied and gave

$$-\frac{r_0^2}{8\mu}\int_V [N]\frac{d^2P}{dz^2}dV = 0 \qquad 3\text{-}30$$

Where dV is the differential element volume and $[N]$ is a one-dimensional array of the shape functions, and where z is the axial direction of 1-D blood vessel element, or

$$[N] = [{}^{N_1}_{N_2}]$$

$$N_1 = \frac{\Delta z - z}{\Delta z}$$

$$N_2 = \frac{z}{\Delta z}; \qquad 3\text{-}31$$

Then the local pressure of any element, P, can be expressed in terms of the nodal pressure array $\{P\}$ and the shape function $[N]$

$$P = [N]^T \{P\}^e \qquad 3\text{-}32$$

where

$$\{P\}^e = \begin{Bmatrix} P_1 \\ P_2 \end{Bmatrix} \qquad 3\text{-}33$$

In order to lower the order of the derivative and evaluate the integral for Equation 3-30, Green's first theorem was applied. The integral of $\frac{d^2P}{dz^2}$ over element volume was broken into two parts, the integral of $\frac{dP}{dz}$ over element surface and integral of $\frac{dP}{dz}$ over element volume as follows

$$-\int_V [N]\frac{d^2P}{dz^2}dV = -\int_{A_s} [N]\frac{dP}{dn}dA_s + \int_V \frac{d[N]}{dz}\frac{dP}{dz}dV \qquad 3\text{-}34$$

Combining Equation 3-30 and 3-34 yielded the first-order integral form of a pressure distribution equation:

$$\frac{r_0^2}{8\mu}\int_V \frac{d[N]}{dz}\frac{dP}{dz}dV - \frac{r_0^2}{8\mu}\int_{A_s}[N]\frac{dP}{dn}dA_s = 0 \qquad 3\text{-}35$$

Boundary conditions shown in Equation 3-36 and 3-37, were evaluated at the left ventricle and right atrium, where the blood flow rate equals the cardiac output, CO, respectively. Cardiac output, CO, is basically a function of skin temperature and core temperature, according to the thermal state of the human body (vasoconstriction or vasodilation).

$$-\frac{r_0^2}{8\mu}\int_{A_s}\frac{dP}{dn}dA_s = -\begin{bmatrix} CO \\ 0 \end{bmatrix} \qquad 3\text{-}36$$

$$-\frac{r_0^2}{8\mu}\int_{A_s}\frac{dP}{dn}dA_s = \begin{bmatrix} CO \\ 0 \end{bmatrix} \qquad 3\text{-}37$$

Humidity ratio in Equation 3-21 and temperature distribution in Equation 3-15, 3-16, and 3-17 are transformed to integral forms by applying similar technique for pressure equation above. More details can be found in Smith's thesis (Smith 1991).

Our computer program is capable of simulating thermal status of the human body in a stage-change environment, with different air temperatures and physical activity levels in different stages. Input variables are: shape information and initial temperature distribution of the human body (read-in files), controlling parameters for stage-change environment and activity levels, and local heat transfer coefficients for convection and radiation. Controlling parameters include timeline, air temperature, humidity ratio, mean radiant temperature, internal heat generation (in MET) etc. for each environment interval and activity level. The output of simulation include temperature distribution, blood pressure, humidity ratio for respiratory tract, latent and sensible heat losses, regional blood flow rate, etc.

Chapter 4 - Simulation results and discussion

In this section, our simulation results were compared with Zhang's experimental data (Zhang 2003) for transient and steady-state cases. For transient comparison, sets of initial condition for simulation were created according to Zhang's experimental setup. By using these initial conditions, transient temperature history of head, trunk, hand, foot, etc. were calculated and compared to those experimental data reported by Zhang for neutral, cold and warm environments. For steady-state comparison, the temperature distribution of all body parts obtained by our shaped model was compared with Smith's cylindrical model and Zhang's experimental data. Moreover, temperature contour for upper arm by our refined model (more elements generated) was compared to Smith's cylindrical model (less elements), to show the advantages of our new model.

4.1 Initial conditions for transient case

Zhang presented two types of data in his work (Zhang 2003). First, he presented steady state values for the temperature distribution through the body after the subjects had been exposed to the specified conditions for 2 hours. Second, Zhang presented transient temperature distribution in segment of the body. To perform a detailed simulation that accurately models the experimental work of Zhang, many environmental and initial conditions must be set in the model. The next paragraph describes how these parameters and initial conditions were set.

The simulation was performed at the three different conditions: neutral, warm, and cold environments. The digital body was assumed to wear a leotard, and generate 23.1 J/cm2·h (1.1 MET). The leotard covers the whole body except face, hands, and feet (covered by socks). The clothing insulation values of leotard are from Zhang's thesis (Zhang 2003), and coded into our clothing database to generate a new ensemble. The heat transfer coefficients for convection and radiation were 2.24 and 1.7 J/cm2 hr °C, respectively. The ambient temperatures were set at 26.9 ºC, 31.5 ºC, and 16.0 ºC for neutral, warm, and cold environment, respectively. The metabolic rate is 1.1 MET for both Zhang's test and our simulation.

Zhang used a bathtub (Zhang 2003) to precondition the human subjects before entering chamber, giving the subjects a more uniform thermal state before starting the study. One important consideration in the body model is the initial temperature of every element in the body. Obviously Zhang did not report such detailed information on the human subjects. To arrive at a realistic initial condition for the digital body, a preconditioning process was also simulated. Our simulation process is : (1) simulate "bathtub precondition process", until a steady state temperature has been achieved and then output the temperature distribution; (2) simulate transient and steady-state human thermal process by using the body temperature distribution from the last step as the initial condition.

The pre-conditioning step was not negligible in our simulation because this process was used to precondition skin temperatures of subjects in Zhang's experiment, and it was proved that the skin temperatures changed during this process, especially for cold environment test. The ambient temperatures were set the same as bathtub's temperatures: 34.5 ºC, 35.6 ºC, and 31.6 ºC for neutral, warm, and cold environments, respectively. All the thermal properties of air, such as conductivity, viscosity, density etc., were replaced with those of water to simulate bathtub environment. It took several hours (simulation time) for skin temperatures to reach steady state. Figure 4.1, 4.2, and 4.3 show the transient average skin temperatures in the preconditioning simulation for neutral, warm and cold environment. Table 4.1 gives temperature comparison (steady state) of preconditioning between our simulation and Zhang's experiment for three environments.

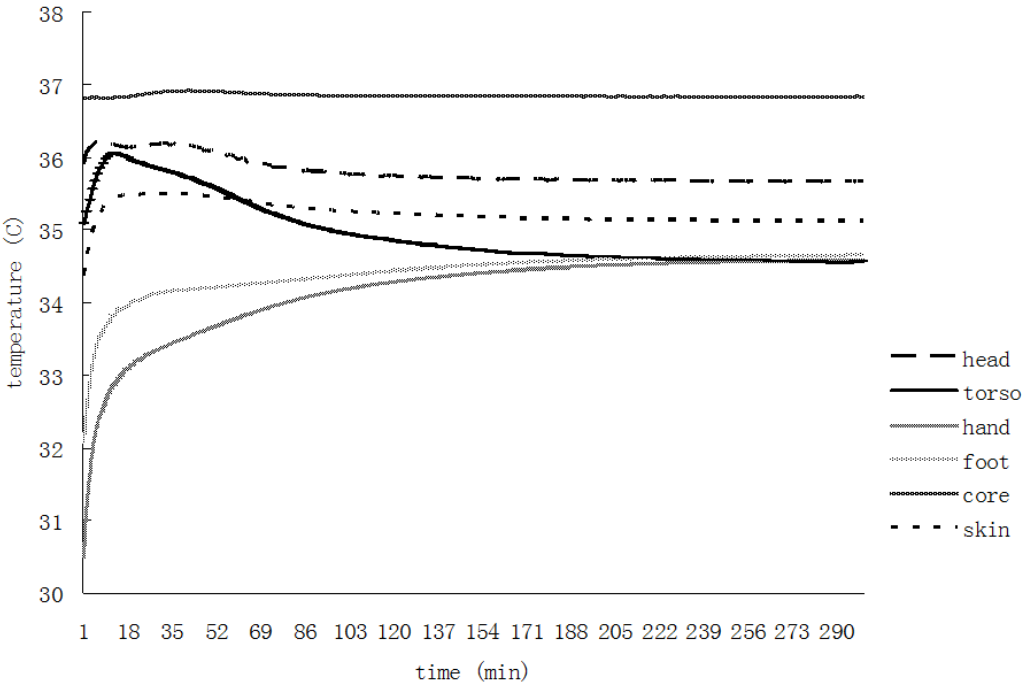

Figure 4.1 Transient temperatures of preconditioning for neutral environment

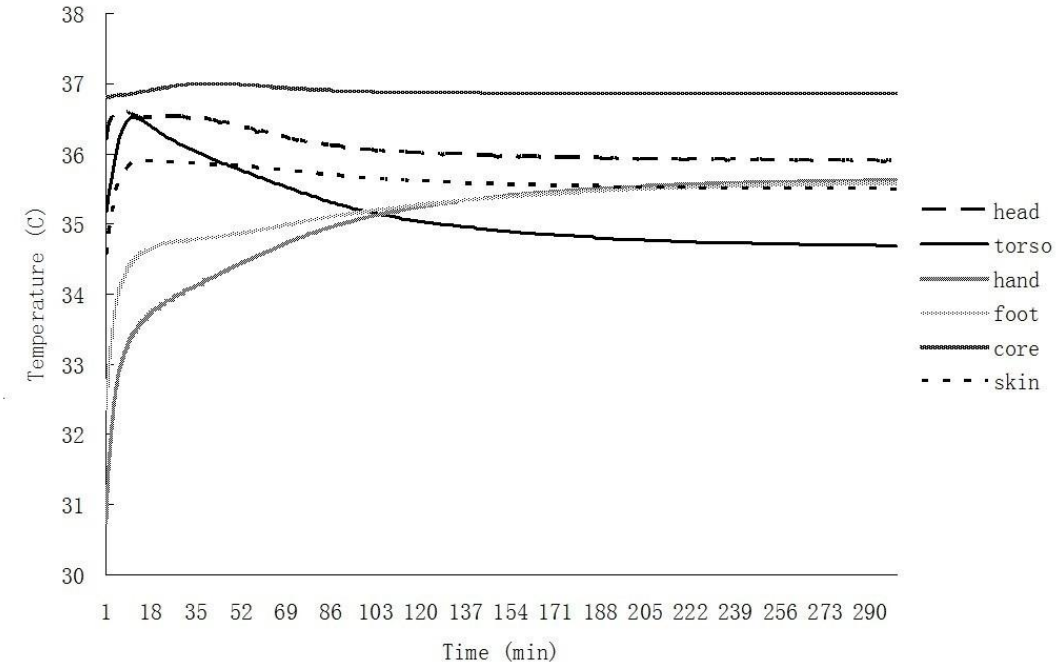

Figure 4.2 Transient temperatures of preconditioning for warm environment

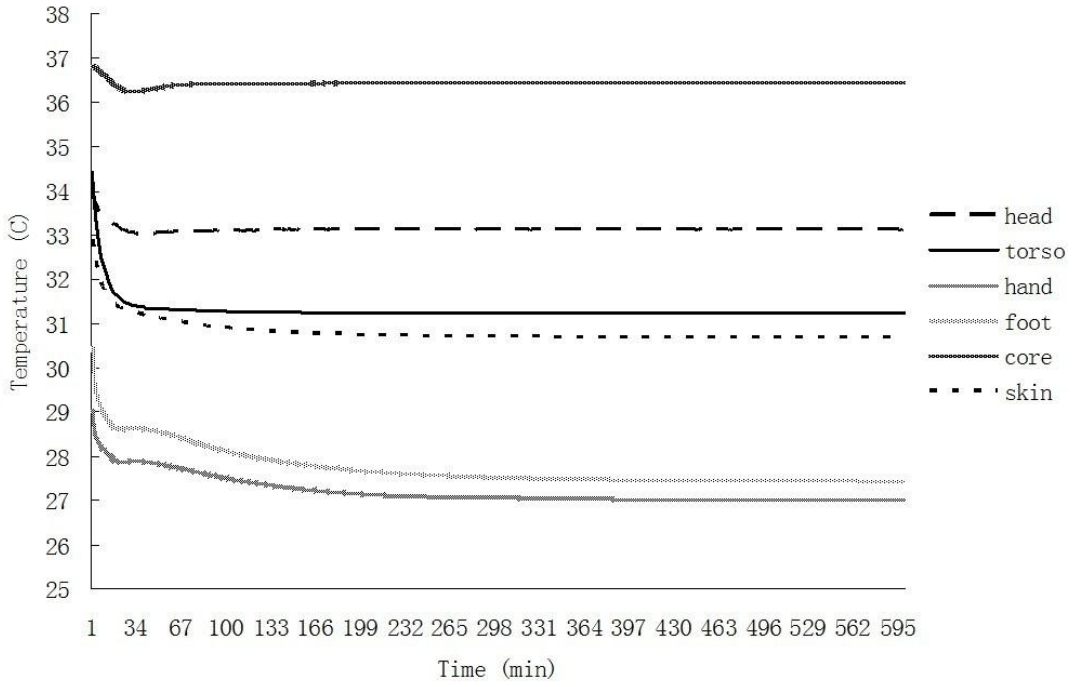

Figure 4.3 Transient temperatures of preconditioning for cold environment

Table 4.1 Temperatures of body parts after preconditioning in three environments

	Neutral		Cold		Warm	
	Current	Zhang's	Current	Zhang's	Current	Zhang's
Head	35.8	35.6	33.1	31.5	36.0	36.5
Torso	34.8	35.7	33.1	29.1	34.8	35.5
Hand	34.4	n/a	27.0	26.5	35.6	35.5
Foot	34.5	34.5	27.2	26.8	35.5	35.6
Core	36.9	37.7	36.4	37.4	37.0	37.4
Skin	33.9	35.0	30.7	n/a	35.8	n/a

For the neutral environment, temperatures tend to reach steady state after about 2 hours (Figure 4.1). Our simulation shows a good prediction on head and foot, which are less than 0.2 ° C to Zhang's data; while our mean skin temperature is 1.1 °C lower than that found by Zhang. For cold environment, the temperature curves converge after 10 hours, longer than neutral and warm cases. The temperatures of hand and foot are very close to experimental data, but at head and torso the temperatures differences exceed 1.5 °C, and our core temperature is 1 °C lower than Zhang's data. Our simulation gives a good prediction in warm environment, and all the temperature differences are less than 0.7 °C: 0.5 °C for head, 0.7 °C for torso, 0.1 °C for hand and foot, 0.4 °C for core temperature. It is observed from Table 4.1 that our preconditioning simulation provides a relatively good prediction of temperatures for three environments, so the temperature distributions of preconditioning can be used as initial condition for the main simulation.

4.2 Transient simulation discussion

The initial conditions of simulation are given in Table 4.2. The simulation time is 120 min, the same as the time used in Zhang's experiment. The transient results for neutral, cold and warm condition are shown in Figure 4.4, 4.5, and 4.6.

Table 4.2 Parameters used for simulation

Parameter	Value	Unit
simulation time	120	minute
convective H. T. coefficient	2.24	J/cm2 hr °C
radiant H. T. coefficient	1.7	J/cm2 hr °C
relative humidity	50%	
metabolic generation	1.1	MET

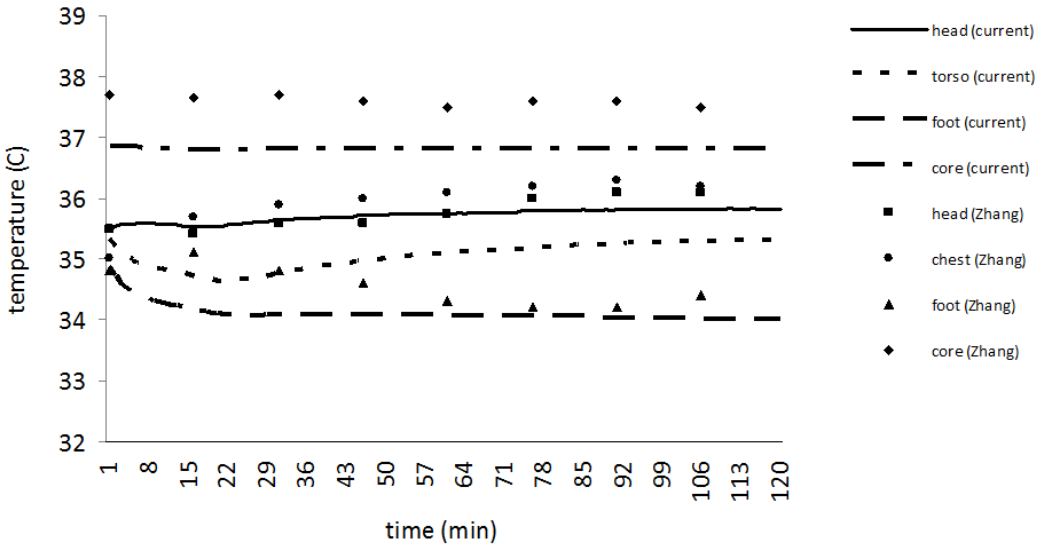

Figure 4.4 Comparison of transient temperatures in neutral environment

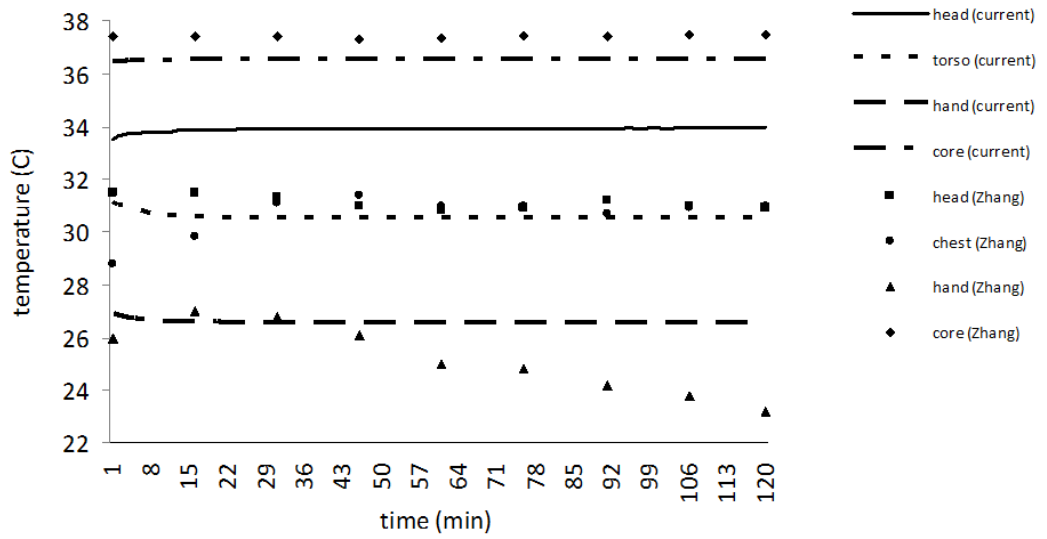

Figure 4.5 Comparison of transient temperatures in cold environment

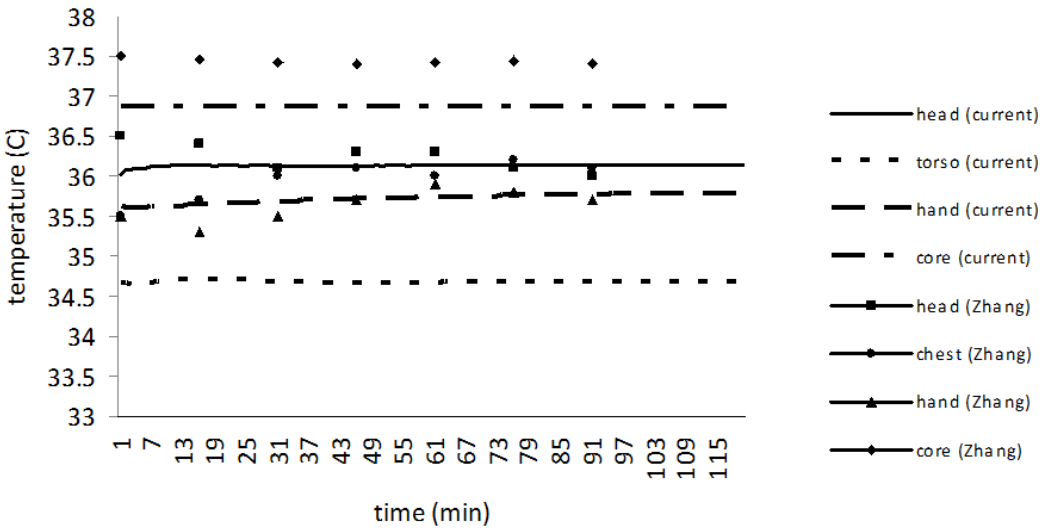

Figure 4.6 Comparison of transient temperatures in warm environment

It can been seen from Figure 4.4 that head and foot temperatures capture the experimental data very well; torso (chest) and core temperatures are about 1 °C lower than experiment, but the trend is the same as experiment: torso temperature goes up within 120 minutes, while core temperature keeps constant. In the cold environment shown in Figure 4.5, torso temperature is comparable to experimental data. Head and core temperatures are 2 and 1 °C lower than experiment, respectively. Hand temperature in our simulation shows a constant trend, while in experiment it drops dramatically after about 30 minutes. For warm condition shown in Figure 4.6, it is similar to neutral condition: head and hand temperatures agree with experiment data, while core and torso temperatures are slightly lower, but keep the consistent trend with experiment measurement. It is concluded that for neutral and warm environments, our simulation provide a good prediction (less than 1 °C) on both skin and core temperatures; while for cold environment, our simulation are 1-2 °C lower than experiment, especially for extremities such as hand and foot. There are two possible reasons for the temperature discrepancy in cold environment: (1) some body parts, such as hand and foot, are of complicated shapes, and the surface area of these parts is much larger than those used in simulation. When subject to cold environment (16 °C), the heat is easier to dissipate to ambient due to larger skin area, so the extremity's temperatures from experiment are lower than those by our simulation. (2) Vasoconstriction occurs when human stays in cold ambient for 10-15 minutes, and some superficial blood vessels are shut off to avoid more heat transfer on skin surface. Meanwhile, shivering also occurs to increase metabolic rate generation inside the human body, so that core temperature can keep on a safe level. Although these two phenomenons are simulated in our model, there is still room to improve them in order to get more accurate results.

4.3 Steady state simulations

Zhang presented temperature distribution for only a few body parts in transient process, but he presented temperature data for all body parts in steady state, so it was very significant to compare our simulation results and Zhang's data in steady state.

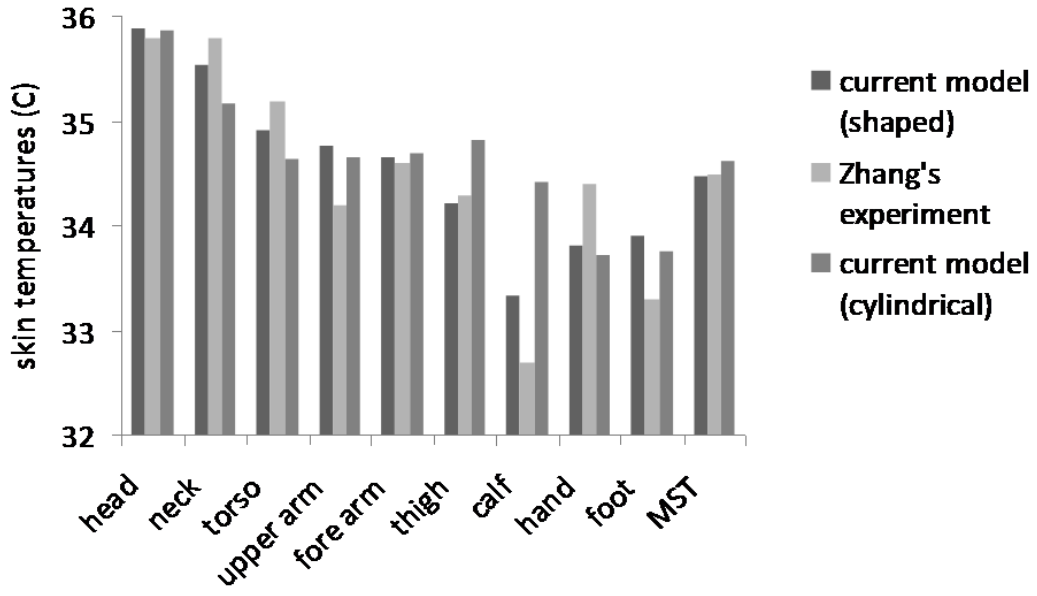

Figure 4.7 Comparison of simulation and experiment in neutral condition

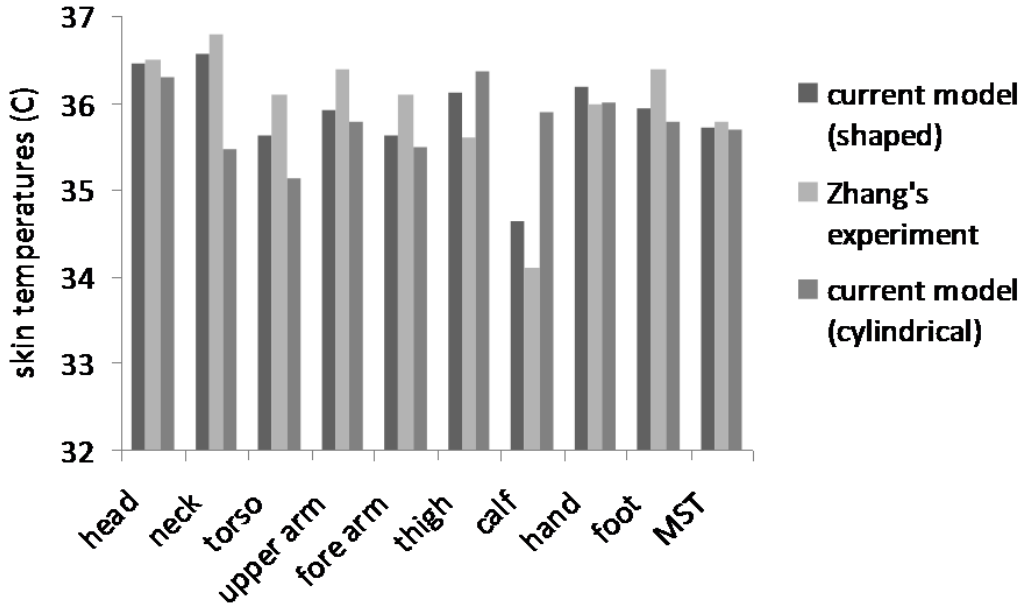

Figure 4.8 Comparison of simulation and experiment in warm condition

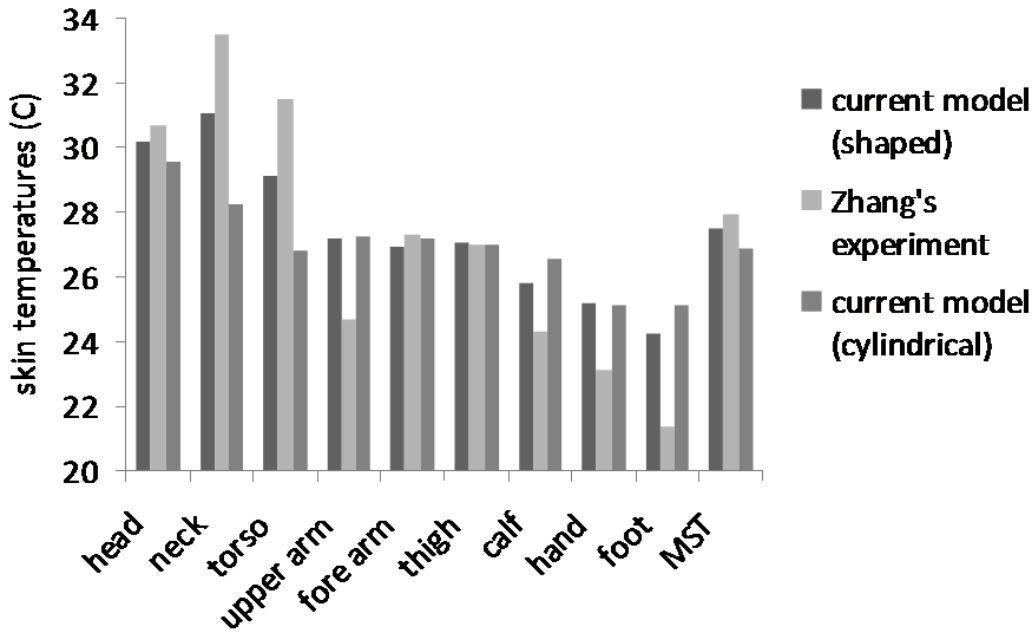

Figure 4.9 Comparison of simulation and experiment in cold condition

Figures 4.7, 4.8, and 4.9 show the mean skin temperatures of different body parts in steady state. Zhang's experiment data (Zhang 2003) and our simulation result with cylindrical body parts and shaped body parts were performed to make comparisons. Mean skin temperature (MST) was also calculated for each case by Hardy and Dubois (Hardy 1938) seven-point formula. In neutral condition shown in Figure 4.7, the skin temperatures of neck, torso, thigh, and calf, predicted by refined shape model, showed much better agreement with Zhang's experimental data than those predicted by cylindrical model. Temperatures at the head and forearm, predicted by both model, were very close to Zhang's data, while temperatures at upper arm, hand, and foot from two numerical models show some differences with Zhang's data. Overall, both refined-shape model and cylindrical model showed good predictions of mean skin temperature (MST), compared to Zhang's data. In warm condition shown in Figure 4.8, the situation was similar: skin temperatures at neck, torso, and calf from refined shape model were closer to Zhang's data than those from cylindrical model; both models gave good prediction at head and hand, as well as MST. But for other body parts such as arm, thigh, and foot, skin temperatures from these two models resulted in an error up to 0.5°C – 1.5°C compared to Zhang's data. In cold condition shown in Figure 4.9, two numerical models showed very good prediction at the forearm and thigh; at head, neck, and torso, the refined-shape model gave better results than cylindrical model; at limb and on extremity such as upper arm, calf, hand, or foot, both numerical models brought a 1.0°C – 2.5°C error compared to Zhang's data. The MST predicted by the refined-shaped model was 0.3°C lower than Zhang's data, while the MST by cylindrical model is about 1.0°C lower.

It can be seen that under neutral and warm conditions, the numerical results of the refined body shape showed good agreement with Zhang's experiment data (Zhang 2003) for most body parts. In contrast, results from the cylindrical body shape showed disagreement with Zhang's data at several body parts, such as neck, torso, and calf. In Figure 4.9, this contrast became even more obvious. There might be two reasons for above observation: (1) the refined-shape model described a human body in a more accurate way than cylindrical model, especially for those body parts which had more complicated shapes other than cylinders, such as head, torso, calf, etc.; (2) in refined-shape model, the radius of the main artery at vasodilation process and blood flow rate through the neck were replaced by the new data according to the fact that the vasodilation phenomenon was stronger at the neck than at other body parts, so that the neck kept

relative high temperatures at both warm and cold conditions. Under cold condition, the temperature prediction by the two numerical models at upper arm, calf, hand, and foot were much lower than Zhang's data. This may be because the vasoconstriction effect of limb and extremity were overestimated so that the heat generation, used for calculation, by vasoconstriction in a cold environment is higher than the body's physical situation. It is possible to improve the prediction in these body parts, if more study is conducted on the mechanism of vasomotor responses. The predictions at neck and torso were still much lower than the experimental data, although the refined-shape model showed some improvement. It was indicated that neck and torso were capable of generating and restoring heat in cold condition and the vasoconstriction effect at neck and torso should be re-evaluated. Mean skin temperature predicted by the refined-shape model showed better agreement with Zhang's experimental data than cylindrical model, especially in cold condition, which is a reflection of overall improvement of our new model.

Our refined-shaped model not only handled new data of body shape, but also provided more details of temperature in longitudinal direction of body parts. In general, the more slices were divided in longitudinal direction, the more details were shown, and the resolution of temperature map increased. Figures 4.10a and 4.10b show the skin temperature map of torso obtained by old and new models, and the longitudinal divisions of the old and new model were 6 and 12, respectively. It was observed that the new model in Figure 4.10b showed more details of variation of temperature in longitudinal direction than the old model in Figure 4.10a. If necessary, more longitudinal divisions could be made to raise the resolution of the temperature map in simulation. This new feature provided a more accurate way of observing temperature variation longitudinally. More comparison graphs are shown in Appendix D for other body parts.

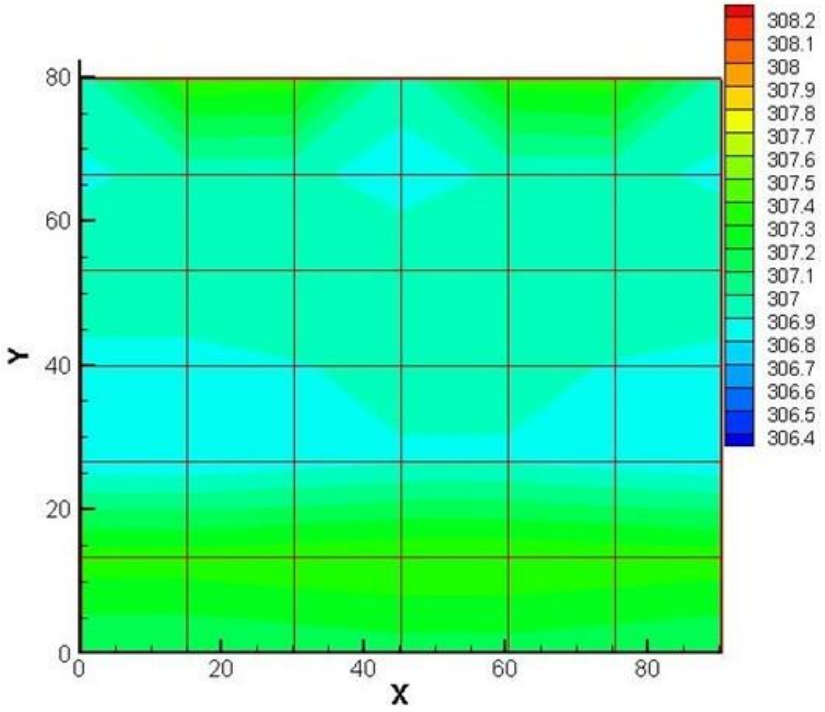

Figure 4.10a. Torso temperature map of old model

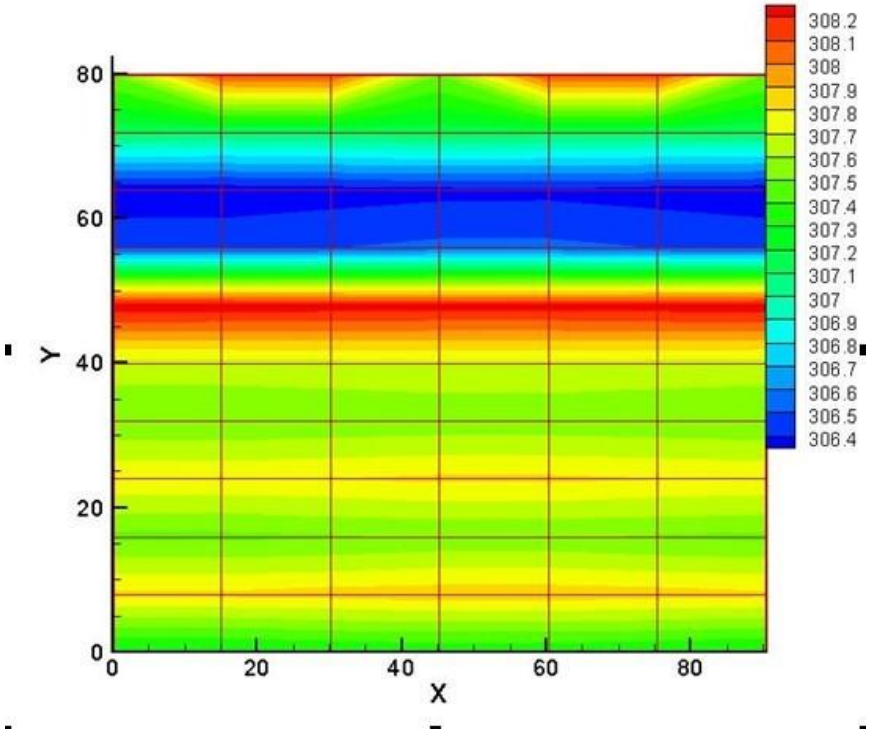

Figure 4.10b. Torso temperature map of new model

Chapter 5 - Experiment facilities and methods

In the previous chapters, a human thermal model was developed to predict the thermal status of human body in various environments. Energy equations are written for tissue and vessel elements (blood vessel and respiratory tract). Vessel equation is a 1-D equation, by assuming that the temperature varies only in the axial direction. The equation includes terms for heat storage, heat conduction, and advection. For the inside tissue element, energy equation includes terms for heat storage, heat conduction, and internal heat generation; while for the surface element, an additional convection terms is added to represent heat convection effect between surface and environment. A constant convective heat transfer coefficient, which varies only with velocity of wind or driving temperature difference, is used in our model. Although convective heat transfer coefficient due to natural convection varies with the location of the human body, it is accurate to use constant coefficient, because it can be solved analytically. However, in practical application, the humans is moving in most of time with activities, and the heat transfer due to forced convection is much more than that due to natural convection. The local heat transfer coefficient also varies significantly with locations. As mentioned in model section, one of our future objectives is to develop a thermal model which is able to simulate moving human body. It is very important to find accurate heat transfer coefficients experimentally for the body parts in forced convection environment, since the analytical solution is not available for complicated convection problems. In this section, we studied the heat transfer phenomenon of a moving cylinder in air flow experimentally. A validation experiment for stationary cylinder in cross-flow was conducted in wind tunnel, and then the data for two types of movement, oscillating and pivot, were obtained.

5.1 Experiment description

A series of experiments were performed to measure the Nusselt Number (Nu) of a heated cylinder in air flow.

1) Stationary cylinder in cross flow (stationary experiment)
2) Transverse oscillating cylinder in cross flow (oscillating experiment)
3) Pivotal movement of cylinder in cross flow (pivot experiment)

The stationary experiment measured the Nusselt Number from a stationary cylinder in cross flow for different airflow speeds, and then we compared our results with Churchill (1977), Hilpert (1933), and Zukauskas' (1972) correlation results. By conducting the stationary experiment, the accuracy and consistency of our experiment design, apparatus, and wind tunnel were validated. The oscillating experiment measured the Nusselt Number of a transverse moving cylinder. The cylinder was also at a cross-flow position as in the stationary experiment, but took a vertical transverse oscillation controlled by Sinusoid function. The period of one cycle movement was nine seconds. "One cycle movement" means that the cylinder starts moving from the origin point, travels through the distance, and then returns back to the origin point. Experiments were conducted for wind speeds of 1.95m/s and 4.78m/s. For each wind speed, two amplitudes $A/D = 3$ and $A/D = 4.5$ were measured, so there were 4 cases in total. (3) The pivot experiment was the most important experiment in our study. It simulated the natural movement of human arms towards air flow, and would provide experimental data for the convective heat transfer coefficient on a moving human. In this experiment, the cylinder was positioned parallel to the wind direction. The back of the cylinder was fixed in the wind tunnel, and is able to lift and lower from a fixed point (or origin point). When the experiment was running, the cylinder moved on the origin point, covering 1/4 circumference. The movement was also controlled by Sinusoid function. The periods of the pivot movement were 14 seconds and 28 seconds, and the wind speed was 2.85m/s, 6.01m/s and 10.71m/s for each period. For pivot experiments, there were six tests in total.

5.2 Experiment facilities

5.2.1 Wind tunnel

The layout of the wind tunnel is shown in Figure 5.1. The operation speed of the wind tunnel is from 0.1m/s to 100m/s. The test section is 2 feet long (0.61 m), and the cross-section is 12 inches (0.305 m) square. The honey comb at entrance regulates the air flow, reducing the

turbulence level of the air drawn in from the surroundings. A fan is positioned at the tail of the wind tunnel, and draws air through the test section. The fan is controlled by a computer software which also shows the pressure and drag force in the wind tunnel. The turbulence level of the wind tunnel varies from 0.5% (1m/s) to 2% (10m/s), depending on the operation wind speed.

Reynolds number, with cylinder diameter as characteristic length, is defined as $\mathrm{Re}_D = \frac{\rho v D}{\mu}$. v is the mean velocity of air flow; D is diameter of the cylinder as characteristic length; ρ and μ are density and viscosity of the air, respectively. The velocity used in our experiment is from 1m/s to 10m/s, which is measured by a hot wire probe. Density ρ and viscosity μ are functions of ambient temperature, but in our experiment they can be considered constant because air temperature in the wind tunnel is always fixed at about 20℃. In our experiment, Re_D ranges from 3,000 to 36,000.

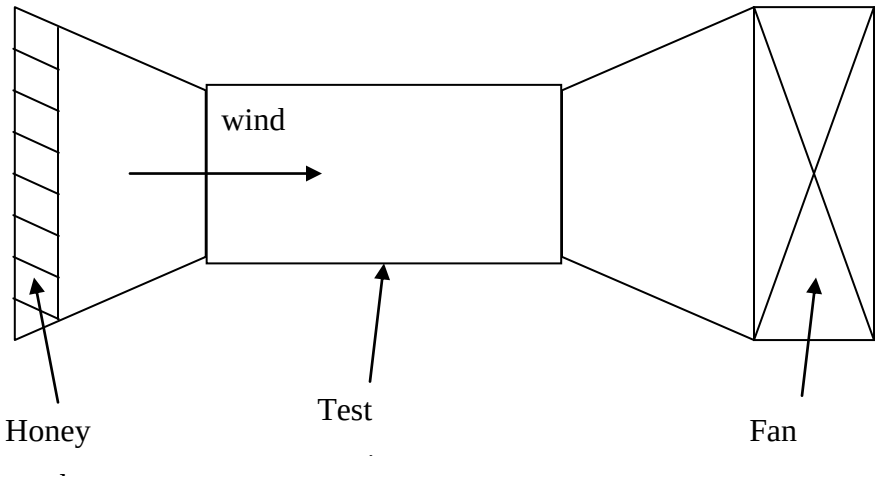

Figure 5.1 Layout of wind tunnel

5.2.2 Test cylinder

The test cylinder used in our experiment is shown in Figure 5.2. It is made of stainless steel. The initial cylinder was made of iron, but it was found that the cylinder rusted on the

surface after a couple of weeks. Although the change of material does not influence the heat transfer coefficient on the cylinder surface, the uneven surface of the initial cylinder changed the type of air flow around the cylinder, resulting in a heat transfer change on the surface. The dimensions of the test cylinder are 2 inches (0.0508 m) in outer diameter, 1.8 inches (0.0457 m) in inner diameter, and 10 inches (0.254 m) in length. The cross-section view of the cylinder in Figure 5.2 shows the arrangement of grooves and measuring devices. Five grooves are evenly distributed on the cylinder surface, and heat flux sensors and thermocouples are embedded in the center pool of grooves. All the grooves are sealed by silicon glue, and then the cylinder surface is sanded smooth so that no extra drag force is added due to the rough surface. The test cylinder is hollow so that a heater can be mounted inside. In our experiment, we use heater tapes to heat the cylinder. The heater tapes are wrapped around a copper tube, which fits inside the cylinder. The details of heater will be discussed in a later section.

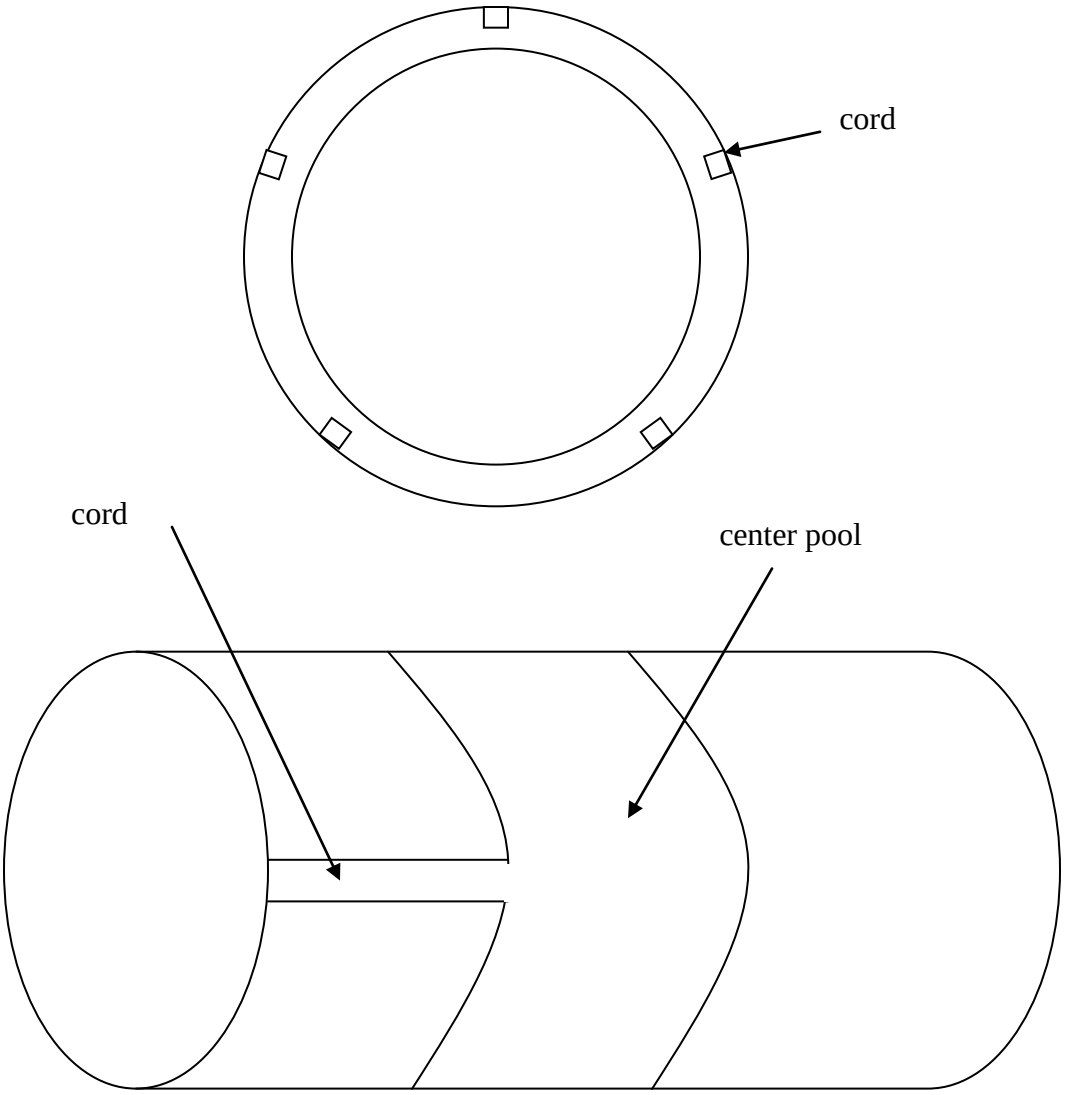

Figure 5.2 Layout of the test cylinder

Figure 5.3 shows the arrangement of heat flux sensors and thermocouples in the center pool of grooves. The five heat flux sensors are glued over the circumference of the cylinder, close to each other as shown in Figure 5.3. The cords of heat flux sensors and thermocouples go through the cord groove, and are collected at the tip of cylinder shown in Figure 5.2. Each sensor takes 1/5 of circumference of the cylinder, or 72°. The thermocouples are just above the heat flux sensors, but do not contact the sensors. Each heat flux sensor reads the average heat flux through 1/5 of the circumference, and thermocouples reads local temperature at the midpoint of the heat flux sensor.

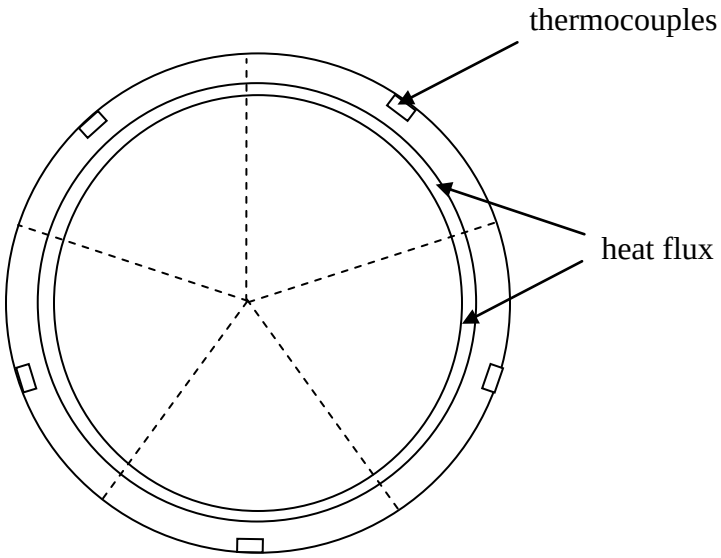

Figure 5.3 Arrangement of heat flux sensors and thermocouples

The advantages of this design are: (1) the smooth surface of the cylinder doesn't disturb laminar air flow. The traditional experiments attached heat flux sensor or thermocouples on cylinder surface directly, and the uneven surface may ruin the laminar boundary layer. (2) Both heat flux sensors and thermocouples read temperatures, so the readings can still be obtained in case one of them is not functioning. (3) Five heat flux sensors cover all area of the cylinder surface, so we are able to calculate both overall and local Nusselt numbers from the cylinder.

5.2.3 Heat flux sensor (HFS) and thermocouples

Our experiment used HFS-4 heat flux sensor from Omega Corporation. The dimension of HFS-4 is shown in Figure 5.4. 0.18 mm (0.007 inches) thickness of the sensors ensures that they can be mounted in grooves. The thermal resistance and sensitivity are 0.01℉/btu/ft^2-Hr and 6.5μV/btu/ ft^2-Hr. Omega HFS-4 heat flux sensor was chosen because: (1) it can be mounted on flat or curved surfaces, and employs butt-bonded junctions with a very low thermal profile for efficient reading. (2) It is capable of precise measurement with high sensitivity and wide temperature range (-330 to 300℉). (3) HFS-4 is able to measure temperature and heat flux simultaneously, providing additional temperature readings to the data collection. The specifications of HFS-4 performance are shown in Table B.1 in Appendix B.

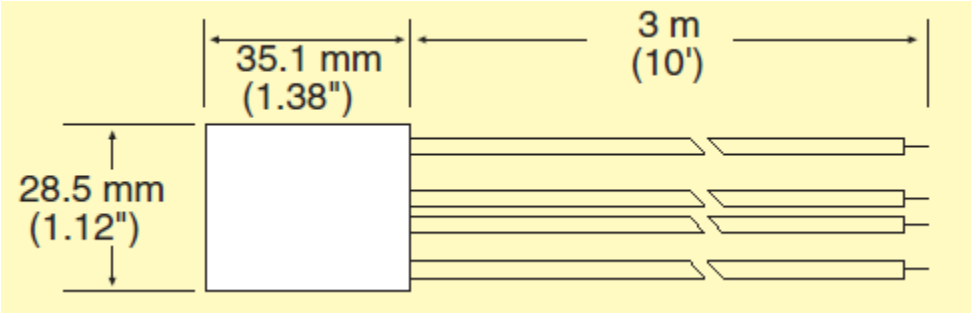

Figure 5.4 Dimension of heat flux sensor (HFS-4)

Surface K-type thermocouples were used to measure the surface temperature, although there were built-in thermocouples in the heat flux sensor. The thermocouples were thin enough to be mounted in the grooves. The reasons for the use of separate thermocouples are: (1) the heat flux sensor stays on the groove bottom, which is 0.1 inch (0.00254 m) from the cylinder surface. There is a temperature gradient through this thin silicon crust due to heat conduction. Therefore, surface thermocouples show more accurate temperatures than heat flux sensors do. (2) The accuracy for heat flux sensors and thermocouples is 0.2℃ and 0.1℃, respectively. Thermocouples are more reliable than heat flux sensor for temperature reading.

Both heat flux sensors and thermocouples are wired to an HP unit for readings. The HP unit is able to read the K-type thermocouple directly. For the heat flux sensor, HP unit reads a volt signal from the sensors, and then a calculation is needed to obtain heat flux. For example, if

a HFS-4 is installed with a sensitivity coefficient of 6.37 microvolts per Btu/ft^{2}Hr, and a reading of 100mV is read from HP unit, then the heat flux is

$$q''_{reading} = \frac{100 \times 10^{-3}}{6.37 \times 10^{-6}} = 15699 \text{ Btu/ft}^2\text{Hr} \qquad 5\text{-}1$$

It is noted that the reading of the heat flux sensor also depends on ambient temperature, so the actual heat flux is the product of heat flux readings and correction factor γ. Correction factor γ is valued in the users' manual, as shown in Equation 5-2.

$$q''_{corrected} = q''_{reading} \times \gamma \qquad 5\text{-}2$$

The HP unit was connected to a computer, and controlled by software LABVIEW. To measure steady-state data, the HP unit scanned data continuously for 10 minutes, with 2 data scanned per second, and 1200 data points were collected for every measuring point. The transient process was monitored by LABVIEW. Generally, it took 20-30 minutes for the cylinder to reach steady state after the thermal status was changed. In our experiment, we started collecting data 40 minutes after thermal status of cylinder was changed.

5.2.4 Heater

The experiment requires a heat source to provide a stable heat flow to the cylinder. We chose heat tapes to heat the cylinder. The reasons are: (1) heat tapes use both radiation and conduction mechanisms, so the cylinder is heated evenly if the inner temperature is not very high. (2) The input power is controlled by a power supply, so it is possible to calculate the total heat exchange between the cylinder and air flow. (3) Heat tapes create a fixed heat flux source, providing convenience to numerical simulation.

5.2.5 Hot wire probe

There are many types of anemometers for experimental use. We chose hot wire probe as our primary anemometer for its high accuracy. The hot wire probe is from Dantec Company with the model number 55P16, as shown in Figure 5.5. It is a cable-equipped miniature wire probe with a protection sleeve that fully protects the wire when not in use. It can be used with all standard CTA anemometers.

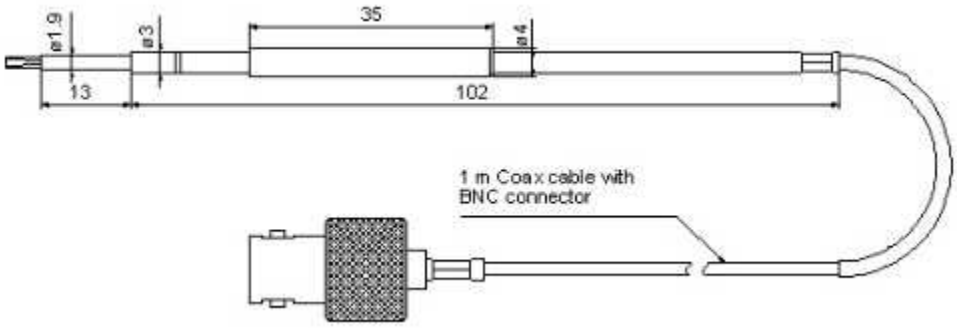

Figure 5.5 Cable-equipped hot wire probe (55P16)

Each hot wire probe needs to be calibrated before use. We used Probe Calibrator 1125 from TSI for all calibrations. The calibration system has three nozzles D1-D3, providing different velocity ranges for various calibrations. The velocity ranges for D1-D3 are 0.01 - 0.1m/s, 0.1 - 20m/s, and 20 - 100m/s, respectively. For our experiment, D2 nozzle with 1 - 20m/s is the best choice, since the velocity used in our experiment is from 1m/s to 10m/s. The probe calibrator connects to an air pump, which feeds air flow. A valve in the calibrator controls air velocity (shown by air pressure) into the nozzle. When calibrating, the hot wire probe is positioned in the middle of the nozzle chamber, and air pressure varies from low to high to cover the desired range of wind speed. The plot of nominal pressure difference ΔP (inch of H_2O) and nominal velocity V (ft/s) of calibrator is shown in Figure 5.6.

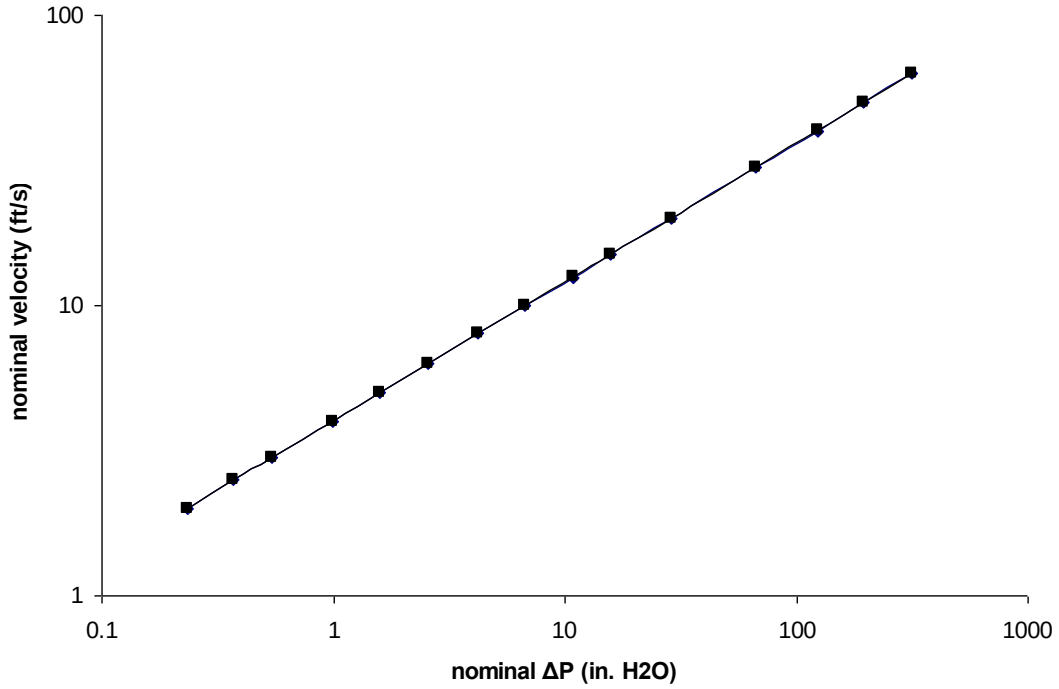

Figure 5.6 Nominal ΔP Vs nominal velocity V

The nominal pressure ΔP can be measured by a pressure transducer hooked on the nozzle. At a certain point, the hot wire probe reads a voltage signal (U), while ΔP is obtained from a pressure transducer (Omega PX-653). According to Figure 5.6, each ΔP corresponds to a nominal velocity. Therefore, a relationship between U and V is built. Table 5.1 shows the 15-point calibration data for the hot wire probe. We use 5^{th} order polynomial to interpolate V in terms of U. The results are shown in Table 5.2.

Table 5.1 15-point calibration for hot wire probe

Data point	ΔP(inch H_2O)	Velocity(ft/s)	Voltage(U)
1	0.33	2.37	2.94
2	1.41	4.73	3.12
3	2.78	6.55	3.22
4	4.61	8.33	3.31
5	7.75	10.69	3.40
6	12.33	13.35	3.49
7	18.36	16.14	3.57
8	24.37	18.49	3.64
9	30.71	20.65	3.70
10	36.72	22.49	3.75
11	42.61	24.15	3.78
12	48.81	25.77	3.82
13	54.71	27.22	3.85
14	60.68	28.60	3.88
15	66.53	29.88	3.90

Table 5.2 Regression analysis for hot wire probe

Regression Statistics	
Parameters	*Coefficients*
Intercept	284.871
U	-324.837
U^2	138.828
U^3	-26.733
U^4	2.011

Table 5.2 gives the values for each parameter in the polynomial. The complete correlation for velocity V of hot wire probe can be written as

$$V = 284.871 - 324.837U + 138.828U^2 - 26.733U^3 + 2.011U^4 \qquad 5\text{-}3$$

In Equation 5-3, wind velocity V is in meter per second, and reading from the hot wire probe U is in volt. The validation procedure is shown in Table 5.3. The second column, predicted V, is calculated by Equation 5-3, while actual V is from measurement. It can be seen that the maximal error occurs at Point 2, with the error 1.5%, and the errors of other points are below 1%. Therefore, Equation 2-3 is a good approximation to wind velocity.

Table 5.3 Validation for Equation 2-1

Validation

Voltage(U)	predicted V	actual V	% of error
2.94	0.73	0.72	0.70
3.12	1.42	1.44	-1.54
3.22	2.00	2.00	0.30
3.31	2.56	2.54	0.83
3.40	3.27	3.26	0.36
3.49	4.06	4.07	-0.31
3.57	4.90	4.92	-0.52
3.64	5.64	5.64	0.03
3.70	6.31	6.29	0.24
3.75	6.85	6.86	-0.05
3.78	7.36	7.36	-0.04
3.82	7.85	7.86	-0.10
3.85	8.32	8.30	0.24
3.88	8.74	8.72	0.30
3.90	9.08	9.11	-0.35

5.3 Experiment setups

5.3.1 Stationary experiment

As mentioned in experiment description, we designed three experiments: stationary experiment, oscillating experiment, and pivot experiment. Stationary experiment is for the purpose of validation. The setup is simple because the cylinder is not moving. The schematic of stationary experiment is shown in Figure 5.7.

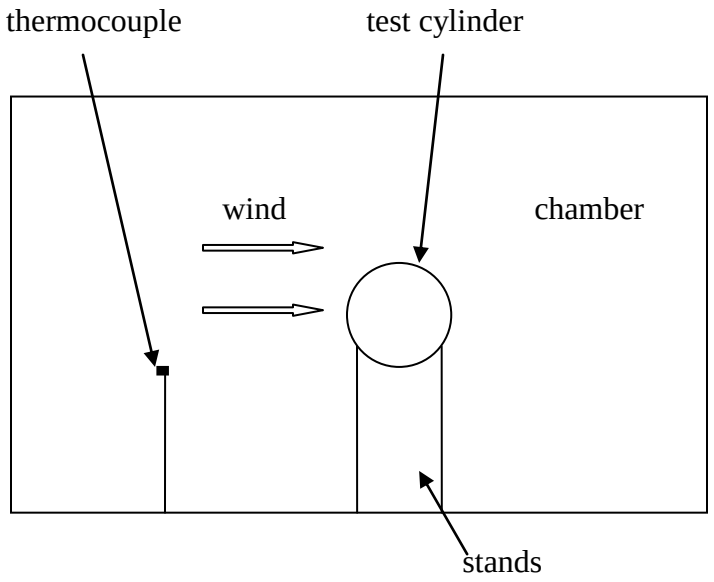

Figure 5.7 Schematic of stationary experiment

As shown in Figure 5.7, the cylinder is horizontally positioned on two small stands, which support two ends of the cylinder. This setup guarantees that the stands don't disturb the air flow in the central measuring area. There is a metal disk on the bottom of the wind tunnel, and this disk can be taken off from the bottom. All the wires from the thermocouples, heat flux sensors, hot wire probe and heaters are bound together and pass through the slot on the disk. The procedure of the stationary experiment is as follows:

(1) Five heat flux sensors are labeled 1 through 5 in advance. Turn the cylinder so that the heat flux sensor No.1 is at leading edge. Angle finder is used for this step.

(2) Turn on the wind tunnel, and use the hot wire probe to find desired wind speed. The hot wire probe and additional thermocouple are positioned in front of the cylinder to measure the infinite flow velocity and ambient temperature.

(3) Make sure the wind tunnel is sealed (no air coming out). Turn on the heaters and start LABVIEW software to monitor the surface temperature and heat flux.

(4) Wait 20 - 40 minutes till the steady state is reached (surface temperature and heat flux convert). Start LABVIEW scanning program for 10 minutes, getting 600 data points (1 data point per second) for the surface temperature, heat flux for each heat flux sensor. Meanwhile, the ambient temperature is captured and recorded.

(5) Turn the cylinder around without stopping wind tunnel and heater so that the heat flux sensor No.2 is at leading edge. Repeat Step (1) - (4).

(6) After heat flux sensor No. 1-5 are positioned at leading edge, stop the wind tunnel and heater. Do the data processing and prepare for the next experiment.

5.3.2 Oscillating experiment

Oscillating experiment and pivot experiment use separate mechanical setups because the moving styles are different. The schematic of oscillating experiment is shown in Figure 5.8.

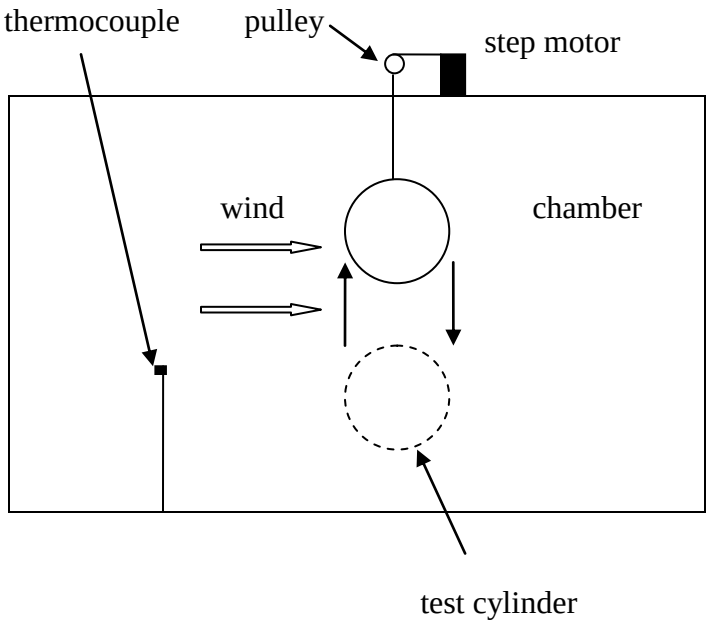

Figure 5.8 Schematic of oscillating experiment

The cylinder is also horizontally positioned, and two ends are tied to a pulley above the chamber. The pulley is driven by a step motor sitting behind. The step motor is also controlled by LABVIEW software. When the experiment goes on, the step motor drives the pulley at a certain speed, and the cylinder reciprocates up and down in the chamber. The speed curve of step motor obeys sinusoid function, so the displacement of the cylinder is a cosine curve, which is shown in Figure 5.9. The reason we use sinusoidal curve for the cylinder movement is because sinusoidal movement is widely used by previous researchers, and it is easier for us to compare our results with others' results. The period of cylinder movement depends on the motor speed. One period means the time that the cylinder starts moving from the original point and move back to this point again. In this experiment the period of cylinder is 10 seconds.

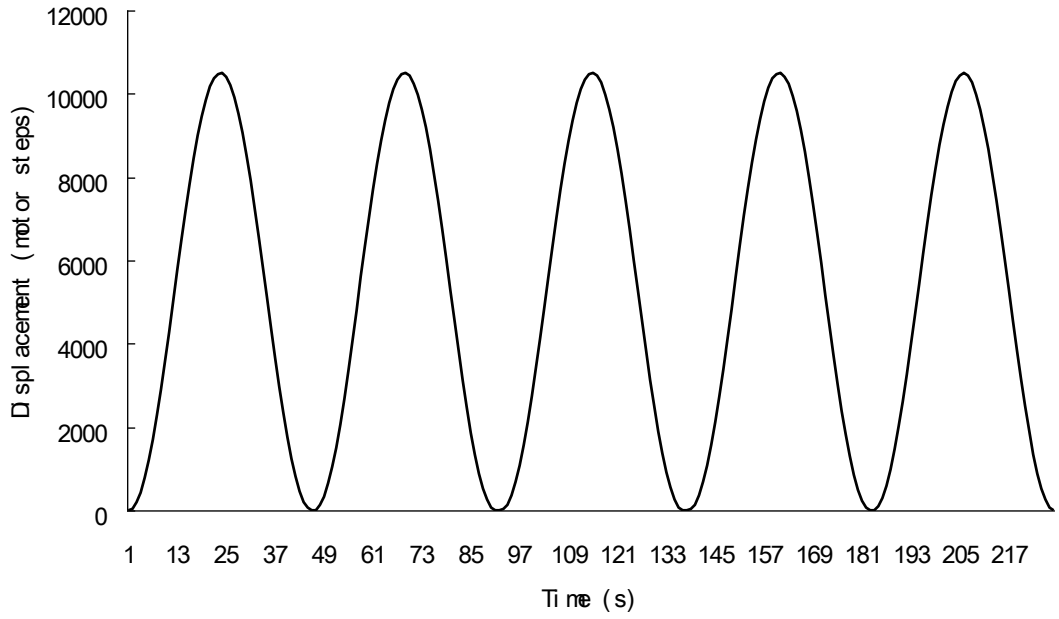

Figure 5.9 Cylinder displacement versus time

The procedure of oscillating experiment is similar to that of stationary experiment except some minor differences.

(1) Put heat flux sensor No.1 at leading edge.

(2) Turn on wind tunnel and find the desired wind speed by hot wire probe.

(3) Open LABVIEW for monitoring and recording purposes.

(4) If necessary, record a set of data for stationary cylinder.

(5) Start oscillating system, and let the cylinder do reciprocating movement vertically. Wait 20 - 40 minutes till steady state is reached. Use LABVIEW to record 10 minutes data for the surface temperature, ambient temperature, and heat flux for each heat flux sensor. Also record the cylinder movement with time because it is useful for transient data analysis. Stop cylinder movement after the data collection.

(6) Turn the heat flux sensor No.2 at leading edge, and repeat step (2) through (5).

(7) After all five heat flux sensors are tested, stop all devices.

5.3.3 Pivot experiment

The pivot experiment simulates the human arm movement, so the cylinder is positioned in the same direction of wind, not in cross-flow direction as before. The schematic of pivot experiment is shown in Figure 5.10.

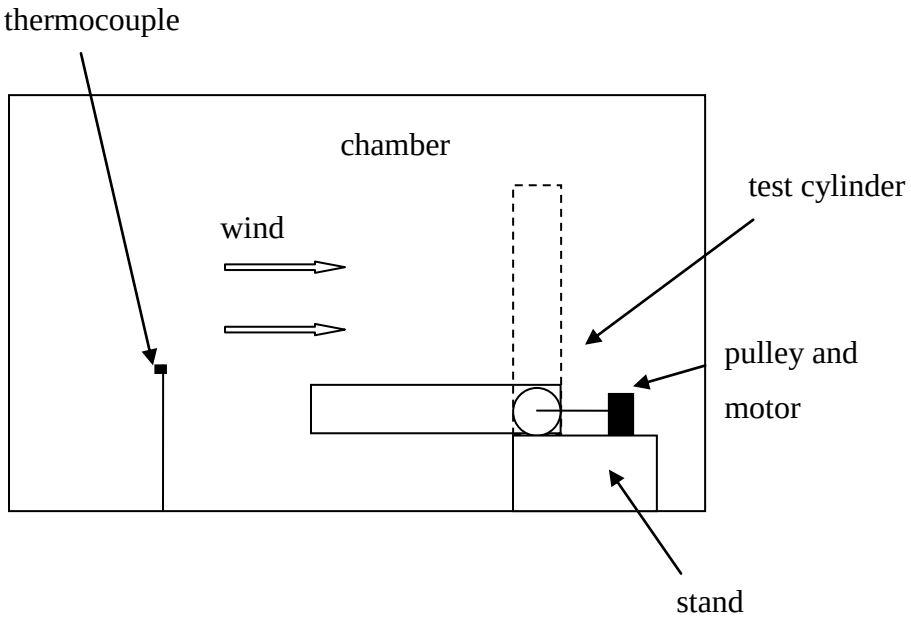

Figure 5.10 Schematic of pivot experiment

One end of the cylinder is fixed on the bottom and bolt to a pulley, but is able to rotate. This pulley connects to the step motor sitting above the chamber through a belt. When the experiment is running, the step motor drives the pulley to rotate through the belt, and the lower end of the cylinder moves at the same speed of pulley. The step motor movement is also controlled by sinusoid curve in Figure 5.9. The displacement of the cylinder covers 90°area as shown in Figure 5.10. We used two different motor speeds for the pivot experiment because we wanted to find the variation of heat transfer rate for different speeds. The periods of the cylinder movement are 14 seconds and 28 seconds, respectively. The procedure of the pivot experiment is:

(1) Put the heat flux sensor No.1 at top, as shown in Figure 5.10, since for the pivot experiment there is no leading edge as in the stationary and oscillating experiment.

(2) Turn on the wind tunnel and find the desired wind speed by the hot wire probe.

(3) Open LABVIEW for monitoring and recording purposes.

(4) Let the cylinder stay at horizontal position (0°), wait until steady state is reached. Record 10-minute data by LABVIEW.

(5) Then move the cylinder to vertical position (90°). Record 10-minute steady state date for this position.

(6) Start the pivot movement system, and let the cylinder reciprocates between 0° and 90° position. Wait until steady state is reached. Record surface temperature, ambient temperature and heat flux data, as well as movement data.

(7) Turn the heat flux sensor No.2 at top, repeat step (2) - (6). Do all five sensors at top position and record data.

5.4 Experiment analysis

5.4.1 Derivation of Nusselt number

The local Nusselt Number is defined in Equation 5-4, where h is the local convective heat transfer coefficient, D is the outer diameter of the cylinder as characteristic length, and k is the thermal conductivity of air.

$$Nu = \frac{hD}{k} \qquad 5\text{-}4$$

$$h = \frac{q''_{corrected}}{(T_{sur} - T_{amb})} \qquad 5\text{-}5$$

Using Newton's Law of cooling, convective heat transfer coefficient h can be obtained as shown in Equation 5-5. $q''_{corrected}$ is the corrected heat flux. T_{sur} and T_{amb} are the surface and ambient temperatures, respectively. Surface temperature can be read from the embedded thermocouple, and ambient temperature is taken from the thermocouple placed in front of the cylinder (upstream measurement), as shown in Figure 5.10. It should be noted that k and h in Equation 5-4 are dependent on ambient temperature T_{amb}. The thermal conductivity of air k, as a function of temperature, can be obtained from any thermal engineering handbook or empirical

correlations. For convective heat transfer coefficient h, substituting Equation 5-2 into Equation 5-5 yields

$$h = \frac{q''_{reading}\gamma}{(T_{sur} - T_{amb})} \qquad 5\text{-}6$$

$q''_{reading}$ is the reading from the heat flux sensors, and γ is the correction factor mentioned in Section 5.2.3. It is noted that the value of γ, provided by manufacturer, varies with different heat flux sensor. By substituting Equation 5-6 into Equation 5-4 gives the expression of Nusselt number as

$$Nu = \frac{q''_{reading}\gamma D}{(T_{sur} - T_{amb})k} \qquad 5\text{-}7$$

All the parameters in Equation 5-7 are from experiment measurements or correlations: $q''_{reading}$, T_{sur}, T_{amb}, and D are from measurements, while γ and k are from correlations. Equation 5-7 is the basic equation used to calculate Nusselt number shown in later sections.

5.4.2 Parameter corrections

As mentioned in the last section, some parameters are dependent on ambient temperature or other external factors. In Equation 5-7, thermal conductivity k, correction factor γ, and heat flux $q''_{reading}$ need to be corrected. This section will discuss how to determine these parameters.

5.4.2.1 Thermal conductivity

The thermal conductivity k of air is a function of temperature. There is a correlation which is generated based on Incropera' s book (2007) shown in Equation 5-9. It is a 3rd order correlation equation, and the applicable range of temperature is from 100K to 1600K, with T is in K and k is in $\mathrm{W/m \cdot K}$. In data process, we use the average of cylinder surface temperature and ambient temperature as calculation temperature for k, shown in Equation 5-8. The calculation temperature range in our experiment is from 20 to 60℃, and the corresponding k value is 0.0257 to 0.0287.

$$T_{cal} = (T_{sur} + T_{amb})/2 \qquad 5\text{-}8$$

$$k = 1.5207 \times 10^{-11} \times T^3 - 4.8574 \times 10^{-8} \times T^2 + 1.0184 \times 10^{-4} \times T - 0.00039333 \quad \text{5-9}$$

5.4.2.2 Correction factor

The correction factor γ is also a function of temperature. The characteristic curve provided by manufacturer is shown in Figure 5.11. A fitting curve is made to interpolate γ within the temperature range 0 to 120℃. This 4th order polynomial is given in Equation 5-10, with temperature unit in ℃. The temperature used for calculating γ is directly obtained from the thermocouples embedded in the heat flux sensors. It is noted that this characteristic curve is valid for all heat flux sensors, although each heat flux sensor has a separate sensitivity.

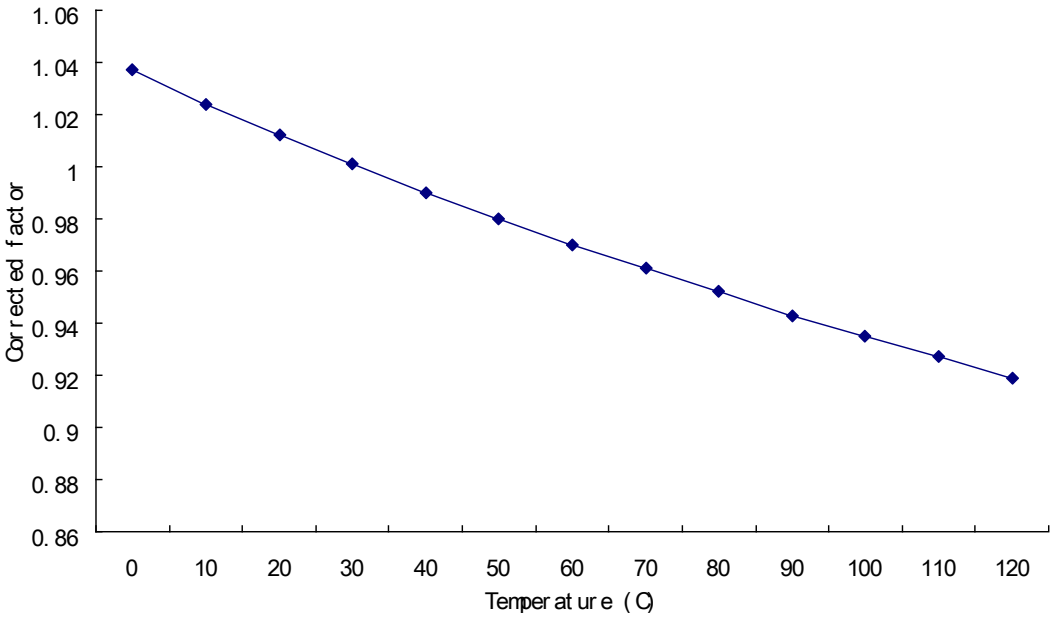

Figure 5.11 HFS characteristic curve of correction factor

$$\gamma = 1.03652 - 0.12909 \times (\frac{T}{100}) + 0.04079 \times (\frac{T}{100})^2 - 0.01830 \times (\frac{T}{100})^3 + 0.00511 \times (\frac{T}{100})^4 \quad \text{5-10}$$

5.4.2.3 Heat flux

The heat flux $q''_{reading}$ read from the heat flux sensor needs to be corrected because the heat flux sensor is located 0.1 inch from the cylinder surface, so the heat flux coming through the measurement plane (inner plane) is larger than that through the top surface. This difference is illustrated in Figure 5.12. For illustration purpose, the ratio of the inner to outer diameter is exaggerated. The inner and outer diameter of the cylinder is 1.8 inches (0.0457 m) and 2.0 inches (0.0508 m), respectively. The area enclosed by dashed line represents one heat flux sensor's coverage. The shadowed area represents the location of the heat flux sensor. The total heat flow Q, passing both inner and outer surface, is assumed to be constant. Therefore, the heat flux passing through the inner and outer surfaces can be calculated as shown in Equation 5-11:

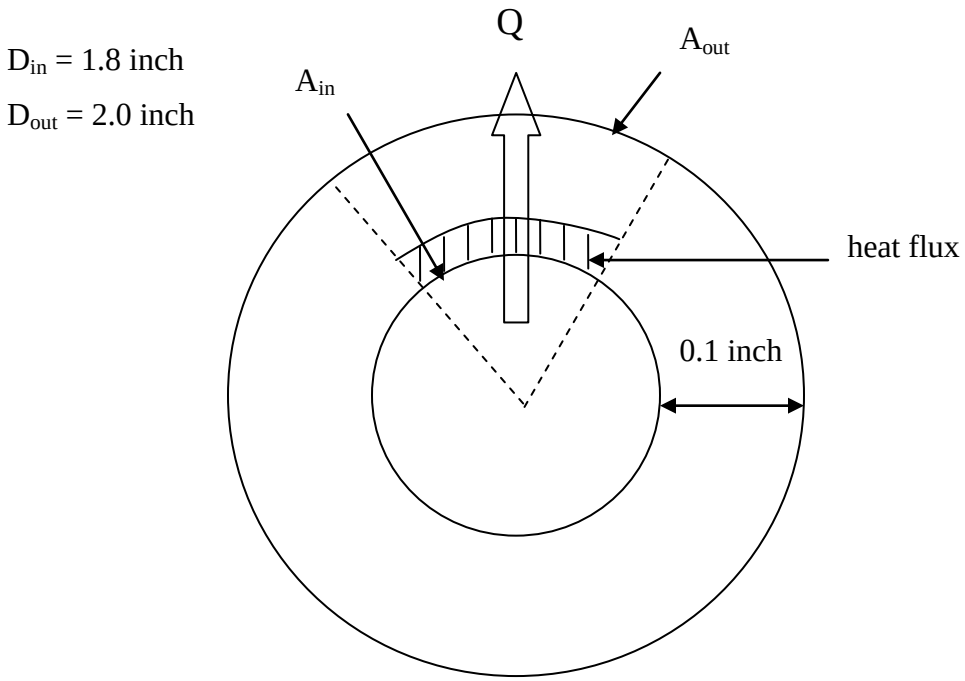

Figure 5.12 Illustration of heat flux correction

$$q_{in} = \frac{Q}{A_{in}}$$

$$q_{out} = \frac{Q}{A_{out}} \qquad \text{5-11}$$

Because the calculation of Nusselt number occurs on the cylinder surface (outer surface), so $q''_{reading}$ in Equation 5-7 should be replace by the heat flux on outer surface, q_{out}. From geometry knowledge, it is easy to obtain the relation between A_{in} and A_{out}. The derivative is shown in Equation 5-12.

$$A_{in} = \frac{1}{5}\pi D_{in} L\ ,\ A_{out} = \frac{1}{5}\pi D_{out} L$$

$$\frac{q_{out}}{q_{in}} = \frac{A_{in}}{A_{out}} = \frac{D_{in}}{D_{out}} = \frac{1.8}{2.0} = 0.9 \qquad 5\text{-}12$$

Substituting Equation 5-12 into Equation 5-7 yields the expression for Nusselt number, by noting that $q''_{reading}$ is replaced by q_{out}.

$$Nu = \frac{0.9 q''_{in} \gamma\, D}{(T_{sur} - T_{amb})k} \qquad 5\text{-}13$$

Equation 5-13 is the final expression used to calculate Nussult number in our experiment. q''_{in} is the reading directly from the heat flux sensor; T_{sur} and T_{amb} are temperature readings from the thermocouples on the cylinder surface and in ambient air; the evaluation of γ and k have been discussed before.

5.5 Uncertainty analysis

There are two types of measurement error, which lead to an system uncertainty, systematic and random. A systematic error, which is known as measurement bias, is associated with the fact that a measured value contains an offset. In general, a systematic error, regarded as a quantity, is a component of error that remains constant or depends in a specific manner on some other quantity. A random error is associated with the fact that when a measurement is repeated it will generally provide a measured value that is different from the previous value. It is random in that the next measured value cannot be predicted exactly from previous such values. Assume $z = z(x_1, x_2 ... x_n)$, where x_i is the independent variable in measurement, the uncertainty due to systematic error can be obtained by Equation 5-14, and the uncertainty due to random error is given by Equation 5-15.

$$\frac{\Delta z}{z} \approx \frac{1}{z}\sum_{1}^{n}\frac{\partial z}{\partial x_i}\Delta x_i \qquad 5\text{-}14$$

$$\frac{\Delta \bar{z}}{z} = \pm\frac{1}{z}\sqrt{\sum_{1}^{n}[(\frac{\partial z}{\partial x_i})\Delta x_i]^2} \qquad 5\text{-}15$$

Recall Equation 5-13. By noting that q''_{in}, γ, D, $\bar{T} = T_{sur} - T_{amb}$, and k are independent variables in measurement, the uncertainty of Nu due to systematic error is given by

$$\frac{\Delta Nu}{Nu} = \frac{1}{Nu}(\frac{0.9\gamma D}{\bar{T}k}\Delta q''_{in} + \frac{0.9q''_{in}D}{\bar{T}k}\Delta\gamma + \frac{0.9q''_{in}\gamma}{\bar{T}k}\Delta D - \frac{0.9q''_{in}\gamma D}{\bar{T}^2 k}\Delta\bar{T} - \frac{0.9q''_{in}\gamma D}{\bar{T}k^2}\Delta k) \qquad 5\text{-}16$$

Notation " Δ " in Equation 5-16 denotes the uncertainty for the separate variables. This uncertainty can be found from the manual or specifications of the measuring tools. For example, the uncertainty of heat flux $\Delta q''_{in}$ is 5% of the readings; ΔD is less than 10^{-5} m if electronic caliper is used; the uncertainty for $\Delta\bar{T}$ is from measuring error of thermocouples, which have a 0.2℃ in uncertainty. Uncertainties of $\Delta\gamma$ and Δk can be obtained from the average error of the correlations in Equation 5-9 and 5-10. Generally, the uncertainty of correlation is no more than 5%. Using appropriate parameters and data from experiment, the system uncertainty can be calculated for all data points. In the range of our experiment, the major source of uncertainty is from heat flux $\Delta q''_{in}$, and the maximal system uncertainty due to bias 4.1% is reached for lowest wind speed case ($v = 1m/s$). The uncertainty is inverse-proportional to wind speed or heat flux. At $v = 10m/s$, the uncertainty is 2.3%.

The uncertainty due to random error is given by substituting Equation 5-13 into definition Equation 5-15. The maximal random error is also achieved for low speed case, but it is smaller than the systematic error. At $v = 1m/s$, 1.2% uncertainty due to random error is observed; while at $v = 10m/s$, uncertainty decreases to 0.8%.

Therefore, the range of total uncertainty in our experiment is from 3.1% ($v = 10m/s$) to 5.3% ($v = 1m/s$). It means that any calculated Nusselt number in our experiment may be ±5.3% from the actual value. In other words, if the Nusselt number is measured multiply times at one point, the maximal possible difference between any two Nusselt numbers is 10.6% due to

uncertainty. This conclusion will be used to check the consistency of data from the heat flux sensor in the next chapter.

$$\frac{\Delta N\bar{u}}{Nu} = \frac{1}{Nu}[(\frac{0.9\gamma D}{\bar{T}k}\Delta q''_{in})^2 + (\frac{0.9q''_{in}D}{\bar{T}k}\Delta\gamma)^2 + (\frac{0.9q''_{in}\gamma}{\bar{T}k}\Delta D)^2 - (\frac{0.9q''_{in}\gamma D}{\bar{T}^2k}\Delta\bar{T})^2 - (\frac{0.9q''_{in}\gamma D}{\bar{T}k^2}\Delta k)^2]^{0.5} \quad 5\text{-}17$$

Chapter 6 - Experiment results and discussion

The experimental apparatus, setups and data processing methods have been discussed in last Chapter. As a creative experiment on moving cylinder in air flow, a verification process was established to ensure the accuracy of the whole system. The stationary experiment was conducted for this purpose, and the accuracy of our system was verified by comparing our results with Churchill (1977), Hilpert (1933), and Zukauskas' (1972) correlations. After the accuracy of system was verified, the oscillating experiment and pivot experiment could be conducted. The purpose of the oscillating experiment was to find how the vertical oscillation effects on the heat transfer of the cylinder in cross-flow. We took data for oscillating experiment with two different wind speeds. The pivot experiment simulated the human arm's swing toward the wind. We had the measurement under two different swing speeds, and for each swing speed three sets of data were record for three different wind speeds.

6.1 Stationary experiment

The stationary experiments were carried out for three wind speeds: 1.95m/s, 3.8m/s, and 8.93m/s. As described in Section 5.3.1, for each case we took five sets of data: the heat flux sensor No.1-5 positioned at leading edge respectively. The reasons for these multipoint measurements are: (1) since each measurement is separate from others, it is a good way to compare and contrast these five measurements. Once one or more heat flux sensors are not functioning, it is easy to find it out by observation or data analysis. (2) A complete chart of data

for each heat flux sensor is obtained, meaning that the data of any heat flux sensor at any position is recorded. Therefore, it is possible to calculate overall Nusselt number around the tube and averaged local Nusselt numbers, etc.

The detailed results for wind speed $v = 1.95 m/s$ are shown in Table 6.1-6.5, with each heat flux sensor at leading edge in the corresponding table, respectively. Line 1 is the averaged ambient temperature during the measurement. Line 2 and 3 are heat flux sensor No. and their locations, respectively. In line 3 of Table 1, "0°" means heat flux sensor #1 (HFS#1) is positioned at leading edge, and "72°" means HFS#5 is positioned next to HFS#1 (see Figure 2.6), etc. Line 4, 5, and 6 are the readings from thermocouples and heat flux sensors. It is noted that surface temperature in Line 4 is lower than the HFS temperature in Line 5, because there is a temperature gradient from the heat flux sensors to the surface thermocouples due to heat conduction. Line 7 is HFS sensitivity from the manufacturer's manual, and Line 9 is the corrected sensitivity influenced by the temperature effect in Figure 5.10, which can be calculated by Equation 5-10. Line 8, temperature for calculation, is obtained from the average of the surface temperature and ambient temperature. This calculation temperature is used to calculate air conductivity in Line 10 by Equation 5-9. Line 11-13 are the calculation process for the heat flux, convective heat transfer coefficient and local Nu, by Equation 2-1, 2-2, 2-4, 2-5, and 2-13. The overall Nusselt number is calculated in Line 14 by averaging all five Nusselt numbers obtained above. Although Nu in Line13 is called local Nu, it is actually an averaged Nu over 72° covering range of the heat flux sensor. It should be also noted that for each measurement it takes 10 minutes for the data collection (about 600 data), and the data in Line 1, 4, 5, and 6 are averaged value of 600 data points.

Table 6.1 Stationary experiment for $v = 1.95 m/s$ and HFS#1 at leading edge

1	Room Temperature (°C)	22.2				
2	HFS #	1	2	3	4	5
3	Angle (0° at leading edge)	0	-72	-144	144	72
4	Surface Temperature(°C)	69.02	72.03	73.43	74.08	73.88
5	HFS Temperature (°C)	70.10	72.99	73.87	74.98	74.84
6	HFS Reading(μV)	1293.34	1056.44	992.73	1012.58	1504.32
7	HFS sensitivity(μV/W/m^2)	0.785	0.888	0.893	0.927	0.906
8	Temperature for calculation (°C)	45.61	47.11	47.82	48.14	48.04
9	Corrected sensitivity (μV/W/m2)	0.773	0.873	0.877	0.910	0.890
10	Air conductivity k (W/m K)	0.028	0.028	0.028	0.028	0.028
11	q"(W/m^2)	1505.99	1089.14	1018.45	1001.04	1521.50
12	h(W/m^2K)	32.17	21.86	19.88	19.30	29.44
13	local Nu	59.1	40.0	36.3	35.2	53.8
14	Overall Nu	44.9				

Table 6.2 Stationary experiment for $v = 1.95 m/s$ and HFS#2 at leading edge

1	Room Temperature (°C)	23.55				
2	HFS #	1	2	3	4	5
3	Angle (0° at leading edge)	72	0	-72	-144	144
4	Surface Temperature(°C)	70.70	68.77	70.94	72.71	73.80
5	HFS Temperature (°C)	72.35	71.33	71.99	73.69	74.97
6	HFS Reading(μV)	1006.59	1421.27	1021.99	937.50	1046.43
7	HFS sensitivity(μV/W/m^2)	0.785	0.888	0.893	0.927	0.906
8	Temperature for calculation (°C)	47.12	46.16	47.24	48.13	48.68
9	Corrected sensitivity (μV/W/m2)	0.772	0.874	0.878	0.910	0.889
10	Air conductivity k (W/m K)	0.028	0.028	0.028	0.028	0.028
11	q"(W/m^2)	1173.92	1463.82	1047.86	926.81	1059.07
12	h(W/m^{2}K)	24.90	32.37	22.11	18.85	21.08
13	local Nu	45.6	59.4	40.5	34.4	38.4
14	Overall Nu	43.7				

Table 6.3 Stationary experiment for $v = 1.95 m/s$ and HFS#3 at leading edge

1	Room Temperature (°C)	23.67				
2	HFS #	1	2	3	4	5
3	Angle (0° at leading edge)	144	72	0	-72	-144
4	Surface Temperature(°C)	70.50	68.62	65.70	66.98	69.68
5	HFS Temperature (°C)	71.59	70.94	67.88	68.72	70.97
6	HFS Reading(μV)	682.32	1226.77	1382.96	890.38	887.85
7	HFS sensitivity(μV/W/m^2)	0.785	0.888	0.893	0.927	0.906
8	Temperature for calculation (°C)	47.09	46.15	44.69	45.33	46.68
9	Corrected sensitivity (μV/W/m2)	0.772	0.874	0.880	0.913	0.891
10	Air conductivity k (W/m K)	0.028	0.028	0.028	0.028	0.028
11	q"(W/m^2)	795.71	1263.48	1414.24	877.70	896.73
12	h(W/m^{2}K)	16.99	28.11	33.65	20.27	19.49
13	local Nu	31.1	51.6	62.0	37.3	35.7
14	Overall Nu	43.6				

Table 6.4 Stationary experiment for $v = 1.95 m/s$ and HFS#4 at leading edge

1	Room Temperature (°C)	22.78				
2	HFS #	1	2	3	4	5
3	Angle (0° at leading edge)	-144	144	72	0	-72
4	Surface Temperature(°C)	65.12	65.88	63.23	60.54	63.01
5	HFS Temperature (°C)	66.29	67.54	65.10	62.78	64.73
6	HFS Reading(μV)	614.53	750.09	1010.60	1199.08	914.19
7	HFS sensitivity(μV/W/m^2)	0.785	0.888	0.893	0.927	0.906
8	Temperature for calculation (°C)	43.95	44.33	43.01	41.66	42.90
9	Corrected sensitivity (μV/W/m2)	0.774	0.875	0.882	0.916	0.895
10	Air conductivity k (W/m K)	0.028	0.028	0.027	0.027	0.027
11	q"(W/m^2)	714.34	771.09	1031.66	1177.52	919.75
12	h(W/m^2K)	16.87	17.89	25.50	31.18	22.86
13	local Nu	31.2	33.0	47.2	58.0	42.4
14	Overall Nu	42.3				

Table 6.5 Stationary experiment for $v = 1.95 m/s$ and HFS#5 at leading edge

1	Room Temperature (°C)	23.32				
2	HFS #	1	2	3	4	5
3	Angle (0° at leading edge)	-72	-144	144	72	0
4	Surface Temperature(°C)	70.87	72.85	73.72	73.10	71.44
5	HFS Temperature (°C)	71.93	74.50	74.80	74.25	72.56
6	HFS Reading(μV)	862.40	891.93	966.52	1344.26	1653.32
7	HFS sensitivity(μV/W/m^2)	0.785	0.888	0.893	0.927	0.906
8	Temperature for calculation (°C)	46.53	47.52	47.96	47.65	46.82
9	Corrected sensitivity (μV/W/m2)	0.772	0.873	0.877	0.911	0.891
10	Air conductivity k (W/m K)	0.028	0.028	0.028	0.028	0.028
11	q"(W/m^2)	1005.15	919.91	991.71	1328.29	1670.12
12	h(W/m^{2}K)	21.14	18.57	19.68	26.68	34.71
13	local Nu	38.8	34.0	35.9	48.8	63.6
14	Overall Nu	44.2				

Table 6.1-6.5 include data collection and data processing, and are not convenient to look and analyze. The Nusselt numbers for all measurements are summarized in Table 6.6. For the purpose of simplicity, the data collection tables such as Table 6.1-6.5, will be presented in Appendix C. Table 6.6 shows the Nusselt numbers with the heat flux sensors sitting on different positions. Nu versus position for Table 6.6 is plotted in Figure 6.1. The discrepancy of the heat flux sensors in our measurements can be seen from this plot, and it is possible to find any disfunctional heat flux sensor by observation on the plot. The summary of the local Nusselt numbers for $v = 3.81 m/s$ and $v = 8.93 m/s$ are shown in Table 6.7 and 6.8, and the corresponding plots are shown in Figure 6.2 and 6.3.

Table 6.6 Nu summary of stationary case $v = 1.95 m/s$

Angle	1	2	3	4	5
-144	31.2	34.0	36.3	34.4	35.7
-72	38.8	40.0	40.5	37.3	42.4
0	59.1	59.4	62.0	58.0	63.6
72	45.6	51.6	47.2	48.8	53.8
144	31.1	33.0	35.9	35.2	38.0

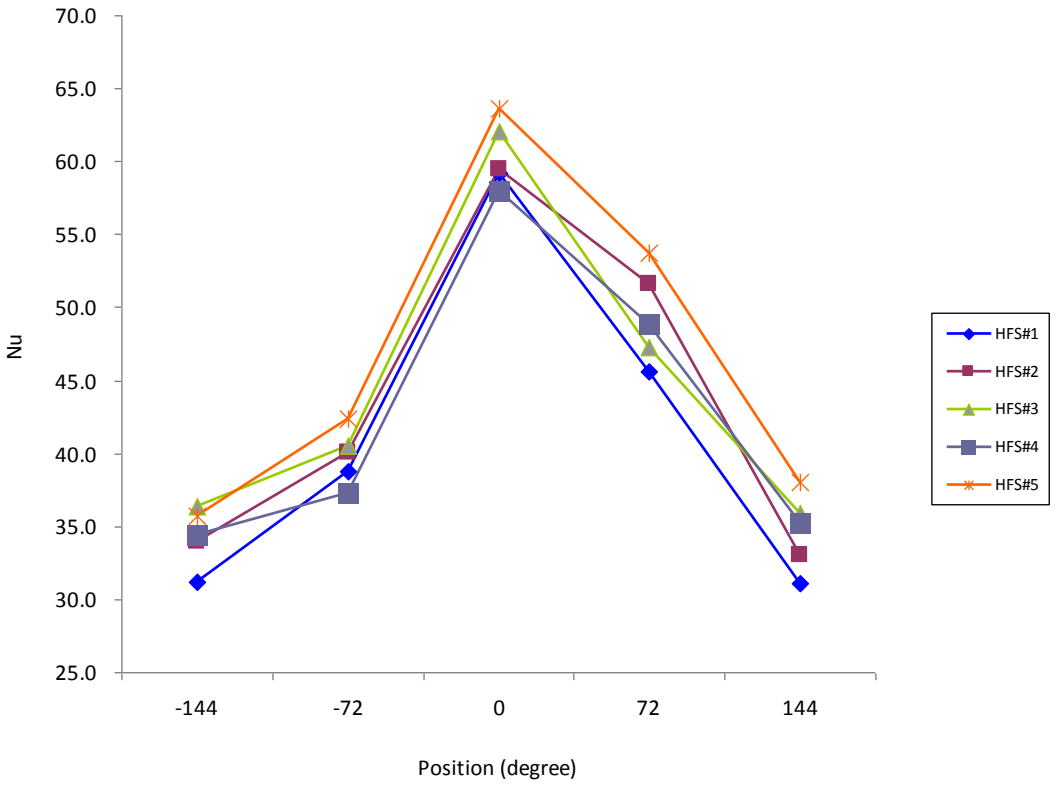

Figure 6.1 Nu versus position for stationary case $v = 1.95 m/s$ Re=6595

Table 6.7 Nu summary of stationary case $v = 3.81 \text{m/s}$

Angle	1	2	3	4	5
-144	49.0	47.9	50.3	45.3	52.8
-72	54.3	59.3	58.1	57.0	62.8
0	93.0	93.3	89.8	88.3	95.0
72	70.4	74.8	67.4	65.7	76.4
144	47.2	49.3	45.5	52.4	48.5

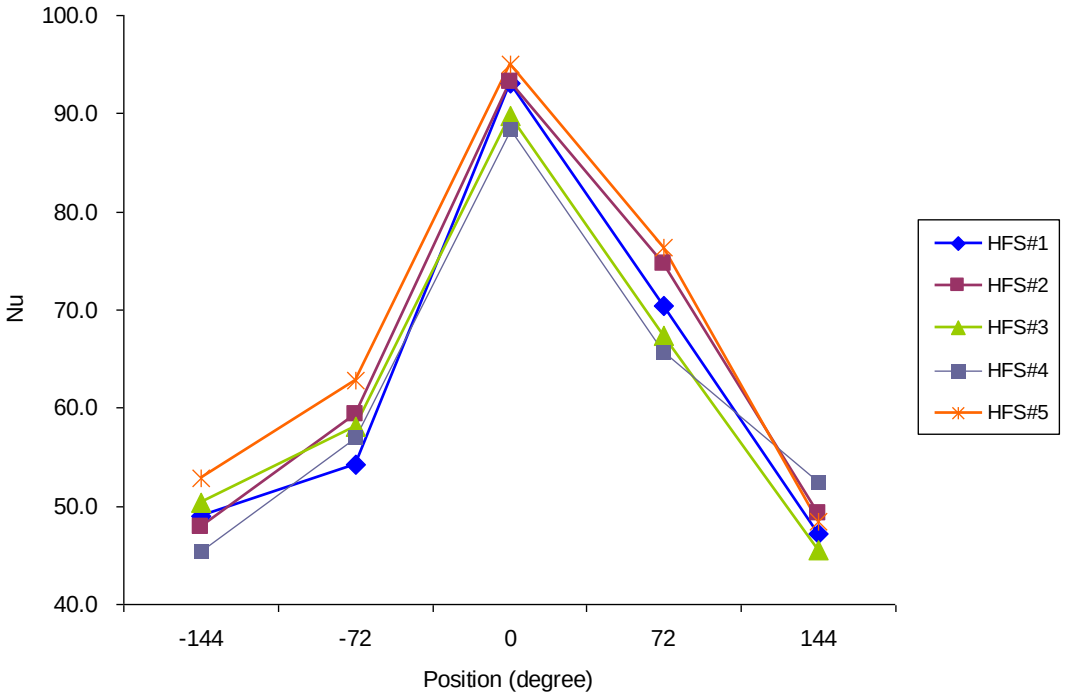

Figure 6.2 Nu versus position for stationary case $v = 3.81 \text{m/s}$ **Re=12885**

Table 6.8 Nu summary of stationary case $v = 8.93 m/s$

Angle	1	2	3	4	5
-144	75.0	91.0	81.0	87.0	97.0
-72	103.2	105.0	94.0	89.9	113.0
0	155.2	164.0	167.0	159.0	170.0
72	120.0	126.0	131.0	117.0	136.0
144	83.4	92.0	87.0	84.7	100.0

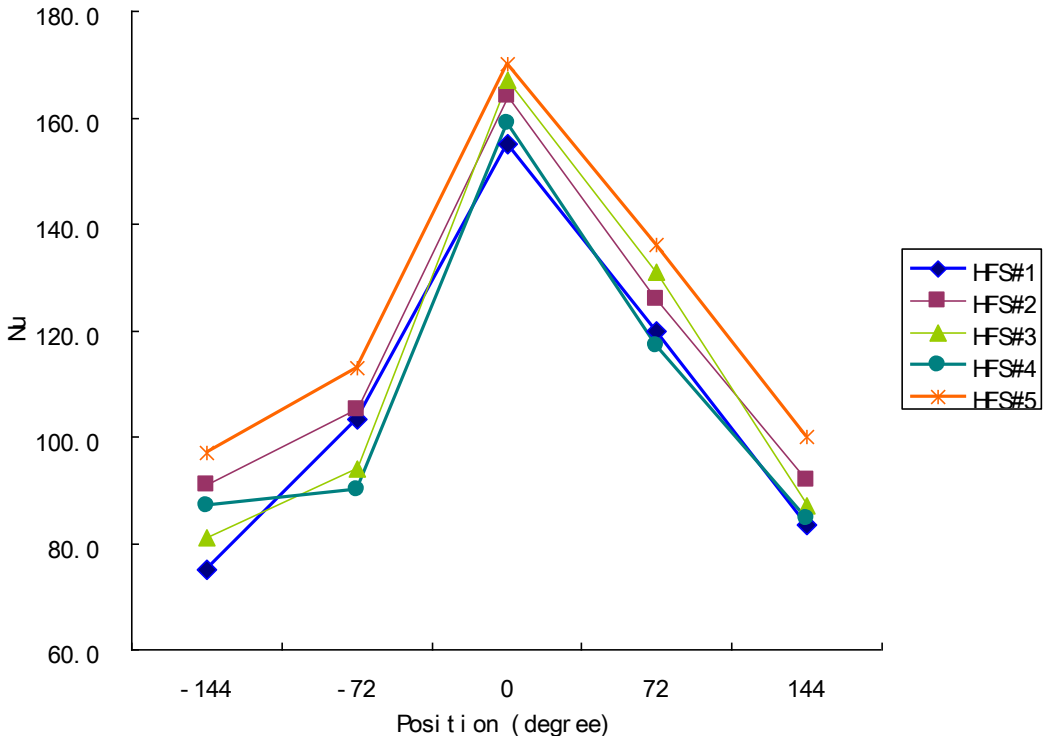

Figure 6.3 Nu versus position for stationary case $v = 8.93 m/s$ Re=30201

Figures 6.1-6.3 show the same trend that the Nu at leading edge is the highest, and decreases around the cylinder circumference. The consistency of the heat flux sensor No.1-5 can be observed from Figure 6.1-6.3. The consistency analysis for $v = 1.95\text{m/s}$, $v = 3.81\text{m/s}$, and $v = 8.93\text{m/s}$ is presented in Table 6.9a, 6.9b, and 6.9c, respectively. The Nusselt numbers measured from the heat flux sensor No.1-5 are averaged for different positions. The standard deviation and 95% confidence interval are then calculated. It can be seen that the maximal ratio of the standard deviation of Nu to the average Nu is less than 8%. Recall that the overall uncertainty of the system is 5.3%, which means the possible maximal difference for two measurements is 10.6%. Therefore, our 8% difference is acceptable, and consistency analysis indicates that the data from all five sensors are valid. In the next comparison part, we average the readings of these five heat flux sensors and compare them to the experimental results or empirical correlations.

Table 6.9a Consistency analysis for $v = 1.95\text{m/s}$

Angle	average Nu (u)	standard deviation (S)	95% confident interval	Ratio S/u
-144	34.3	2.01	±4.01	0.06
-72	39.8	1.90	±3.79	0.05
0	60.4	2.31	±4.62	0.04
72	49.4	3.30	±6.60	0.07
144	34.7	2.66	±5.33	0.07

Table 6.9b Consistency analysis for $v = 3.81\text{m/s}$

Angle	average Nu (u)	standard deviation (S)	95% confident interval	Ratio S/u
-144	49.08	2.50	±4.99	0.06
-72	58.31	2.81	±3.62	0.05
0	91.89	2.44	±4.62	0.03
72	70.94	4.11	±6.60	0.06
144	48.55	2.31	±5.33	0.05

Table 6.9c Consistency analysis for $v = 8.93\text{m/s}$

Angle	average Nu (u)	standard deviation (S)	95% confident interval	Ratio S/u
-144	86.20	6.56	±13.12	0.08
-72	101.03	7.53	±15.06	0.07
0	163.04	5.98	±11.96	0.04
72	126.01	7.78	±15.56	0.06
144	89.43	6.31	±12.62	0.07

Recall Churchill (1977), Hilpert (1933), and Zukauskas' (1972) empirical correlations of overall Nu in Equation 6-1, 6-2, and 6-3. It can be seen that three correlations are dependent on Re_D and Pr. Reynolds number with cylinder diameter as characteristic length, is defined as $\text{Re}_D = \rho VD / \mu$. The air density ρ and viscosity μ are functions of ambient temperature. In our experiment, the ambient temperature varies in a very narrow range from 20℃ to 23℃, so ρ and μ can be considered as constants. The air velocity range is from 1m/s to 10m/s. Therefore, Re_D varies from 3,000 to 36,000, which is in the effective range in Equation 6.1 - 6.3. The

Prandtl number Pr is defined as $\mu c_P / k$, where μ, c_P, and k are the viscosity, specific heat, and conductivity of air, respectively. Pr can also be considered as constant because μ, c_P, and k do not change much with temperature variation in our experiment. The value of Pr used in our calculation is 0.701.

$$Nu_D = 0.3 + \frac{0.62\,\mathrm{Re}_D^{1/2}\,\mathrm{Pr}^{1/3}}{[1+(0.4/\mathrm{Pr})^{2/3}]^{1/4}}[1+(\frac{\mathrm{Re}_D}{282000})^{5/8}]^{4/5}$$

$$\text{for } \mathrm{Re}_D\,\mathrm{Pr} > 0.2 \qquad \text{6-1}$$

$$Nu_D = 0.193\,\mathrm{Re}_D^{0.618}\,\mathrm{Pr}^{1/3}$$

$$\text{for } 4000 < \mathrm{Re}_D < 40000 \qquad \text{6-2}$$

$$Nu_D = 0.26\,\mathrm{Re}_D^{0.6}\,\mathrm{Pr}^{0.37}(\frac{\mathrm{Pr}}{\mathrm{Pr}_s})^{1/4}$$

$$\text{for } 10^3 < \mathrm{Re}_D < 2\times 10^5 \qquad \text{6-3}$$

Table 6.10 shows the Nu comparison of our experimental data with Churchill (1977), Hilpert (1933), and Zukauskas' (1972) empirical correlations in Equation 6-1, 6-2, and 6-3. The corresponding column chart is drawn in Figure 6.4 for the further observation. For $v = 1.95$, Nu from our experiment is very close to Churchill's result (1.4% higher), 9.7 % higher than Hilpert's and 3.4% lower than Zukauskas'. For $v = 3.81$, our Nu is 3.9% and 7.4% higher than Churchill and Hilpert's, respectively; and 4.2% lower than Zukauskas'. For $v = 8.93$, our result is the highest among all data, 1.8% higher than Zukauskas, and 12.5% than Churchill and Hilpert's. It

can be seen from above analysis that our data are higher than Churchill and Hilpert's correlation result , and lower than Zukauskas correlation result for $v = 1.95$ and $v = 3.81$; while for $v = 8.93$ our data is the highest, showing a 12.5% difference to Churchill's. The wind speed for the next oscillating and pivot experiments is from 1m/s to 10m/s, which fits the speed range of above verification experiment. Therefore, it can be concluded that our whole experimental system, including apparatus, measuring method, and data process, is accurate for Nu measurement of a cylinder in cross flow, and will be able to provide convincing results for moving cylinder experiments.

Table 6.10 Nu comparison for stationary cases

	v=1.95	v=3.81	v=8.93
Ours	43.1	63.8	113.1
Churchill	42.5	61.4	100.5
Hilpert	39.3	59.4	100.6
Zukauskas	44.6	66.6	111.1

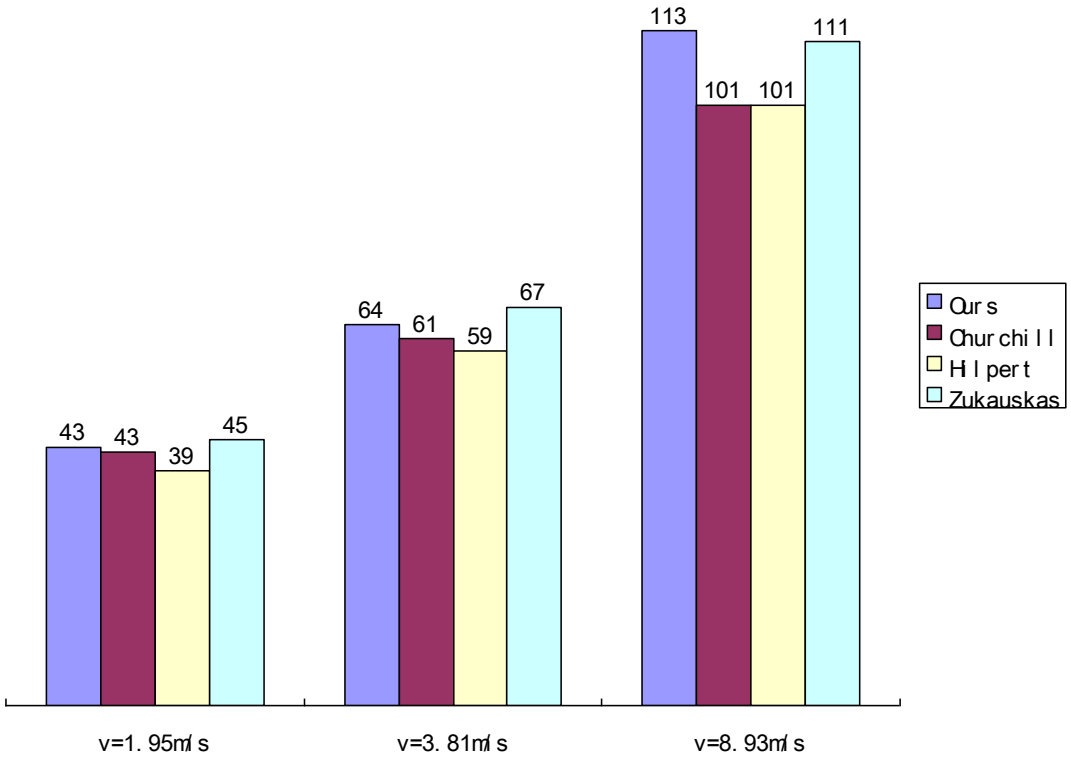

Figure 6.4 Nu comparison for stationary cases

One point which needs to be mentioned is that Nu curves show asymmetrical values at +72° and -72° positions in Figure 6.1 - 6.3. Nu at +72° position is always higher than that at -72° by 10 - 20%. The reason may attribute to the natural convection, which is not negligible for low speed cases. Due to the heated wall of the cylinder, the nearby air is heated and forms a thermal boundary layer along the cylinder surface from bottom to top. The heated air at the cylinder bottom starts to move up due to lower density, and a velocity boundary layer also forms vertically on the cylinder surface. The consequence is that air moves fasters at the top than it does at the bottom, so the heat transfer effect is enhanced on the cylinder top, leading to a higher Nu at +72° position. A validation of above suggestion is shown in Equation 6-4, which calculates

Gr_D / Re_D^2 for $v = 1.95$ at 293℃. Gr, as Grashof number, indicates the ratio of the buoyancy force to the viscous force acting on the fluid. The higher Gr is, the stronger natural convection will be induced. Therefore, the value of 0.067 for Gr_D / Re_D^2 implies that natural convection still take non-negligible part compared to forced convection.

$$Gr_D / Re_D^2 = \frac{g\beta(T_s - T_\infty)D^3}{\nu^2} / (\frac{\rho UD}{\mu})^2 = 0.067 \qquad 6\text{-}4$$

Figure 6.5 shows the repeatability of Nu number in our experiment. Three tests are conducted under the same condition $v = 1.95$ m/s. The maximal ratio of standard deviation to average Nu number is 2.8% at 144°, which is less than the uncertainty of system, 5.3%. The ratio for overall Nu number is 0.25%. Figure 6.5 indicates that the experiments are repeatable within the accuracy of apparatus.

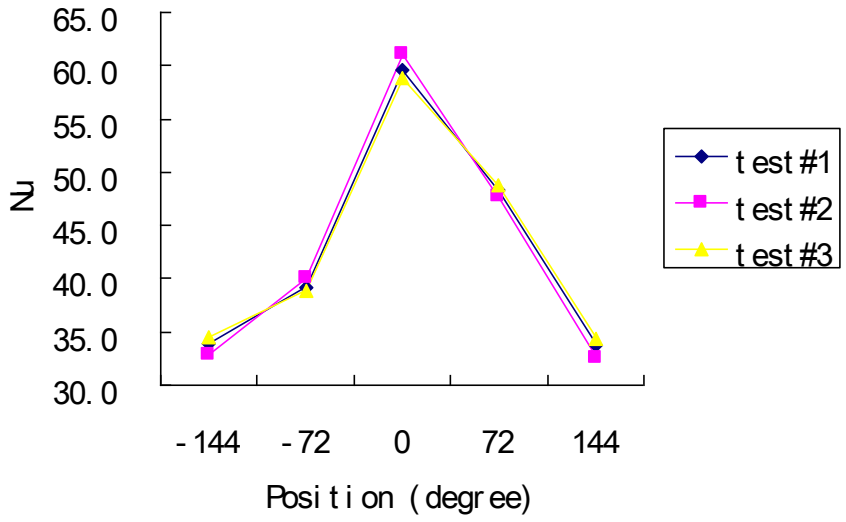

Figure 6.5 Repeatability of Nu number

6.2 Oscillating experiment

As mentioned in last chapter, the purpose of oscillating experiment focuses on the effect of vertical movement on heat transfer in cross-flow model. The research from Sreenvasan (1961), Kezios (1966), Saxena (1978), and Cheng (1997), etc. show that the heat transfer coefficient may be influenced by the non-dimensional frequency f^* (defined as fD/U), amplitude ratio (A/D), and wake mode. The frequency f of the cylinder oscillation in our experiment is 0.1, amplitude ratio 1.5, and $2P+2S$ for wake mode. The wind speeds applied for the oscillating experiment are $v=1.95m/s$ and $4.78m/s$. As described in Section 6.3.2, the data for stationary cylinder was taken first, then the cylinder was oscillated and data were recorded for five locations. Average Nu numbers are obtained in the same way as in stationary case.

For $v=1.95m/s$, the stationary Nusselt number versus angle is shown in Table 6.11, with angle averaged Nu and overall Nu, while the oscillating Nusselt number is shown in Table 6.12. The average Nu for stationary and oscillating cases are plotted against angels in Figure 6.6. The complete tables are collected in Appendix C. The overall Nu for the stationary experiment is 42.7; while for the oscillating experiment is 43.7. It seems like oscillation of the cylinder brings a 2.3% boost on Nu compared to stationary result. However, from the aspect of heat transfer, 2.3% boost is not so obvious that it can be considered as effects of vertical oscillation. Sreenvasan (1961) pointed out that if Reynolds number is between 2500 and 15000, and the ratio of vibration velocity to air flow velocity is below 20%, the heat transfer remains unaffected. In our experiment, Reynolds number for $v=1.95m/s$ case is 6595, and the ratio of two velocities is about 2%. The fact that our oscillating Nu is not much higher than stationary Nu agrees on

Sreenvasan's observation. Studies from Sexana (1978), Cheng (1997), and Gau (1999) show that the heat transfer coefficient will be increased significantly if the oscillation frequency is close to Strouhal number. According to Bearman (1969), Kim (1986), and Achenbach (1981)'s studies, Strouhal number is a function of Reynolds number. Sarioglu (2000) gave a correlation for vortex shedding frequency f_s in Equation 6-5, where F is called shedding frequency parameter, f_s is vortex shedding frequency, D is diameter of the cylinder as characteristic length, and ν is kinematic viscosity. According to the definition $St = \frac{f_s D}{U}$, Strouhal number in our experiment is about 0.3 to 1.5, depending on wind velocity. However, the oscillation frequency in our experiment is 0.15, which is much less than Strouhal number, so the increasing of Nusselt number is not obvious for $v = 1.95 m/s$ in our experiment.

$$F = f_s D^2 / \nu = 0.194\,\mathrm{Re} + 1006 \qquad 6\text{-}5$$

Table 6.11 Nu of stationary case $v = 1.95 m/s$

Angle	1	2	3	4	5	angle average
-144	28.8	34.0	36.3	34.4	35.7	33.4
-72	38.8	40.0	40.5	37.3	42.4	39.1
0	59.1	59.4	62.0	58.0	64.0	59.6
72	45.6	51.6	47.2	48.8	54.6	48.3
144	28.7	33.0	35.9	35.2	37.0	33.2
Overall Nu						42.7

Table 6.12 Nu of oscillating case $v = 1.95 m/s$

Angle	1	2	3	4	5	angle average
-144	27.3	32.9	36.1	31.2	34.7	32.4
-72	38.6	39.8	40.3	36.8	42.5	39.6
0	60.6	61.1	62.9	60.5	65.2	62.1
72	45.3	51.0	47.3	50.2	55.7	49.9
144	28.2	32.3	35.8	37.6	38.6	34.5
Overall Nu						43.7

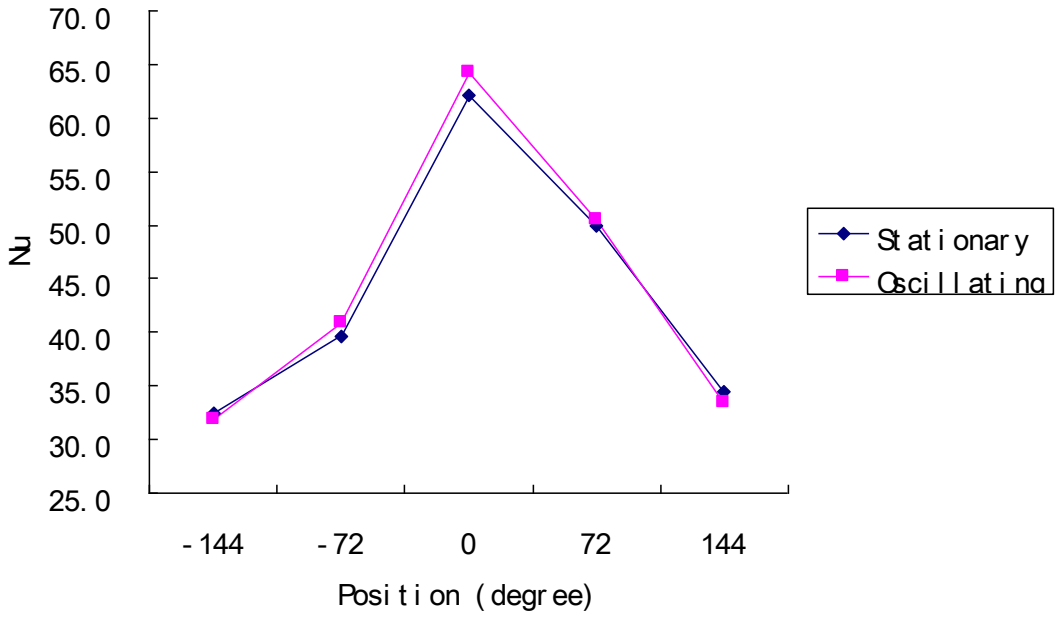

Figure 6.6 Average Nu comparison for stationary and oscillating cases $v = 1.95m/s$

For $v = 4.78m/s$, the stationary and oscillating Nu are shown in Table 6.13 and 6.14, and the corresponding plot is drawn in Figure 6.7. The average Nu for the stationary case is 73.0, which is even higher than Nu for the oscillating case, 72.3. In this case, Strouhal number is about 1.4, much more than the cylinder oscillation frequency 0.15. Therefore, it is confirmed that if the oscillation frequency is not close to Strouhal number of the system, Nu would not have an obvious change when the cylinder is oscillated. It should be mentioned that natural convection still exists in oscillating experiment, and Nu at 72° position is higher than that at -72° position.

Table 6.13 Nu of stationary case $v = 4.78 m/s$

Angle	1	2	3	4	5	Angle average
-144	52.3	61.0	62.5	65.2	70.2	60.3
-72	60.2	62.0	65.8	65.9	72.2	63.5
0	98.6	101.8	108.3	103.9	112.5	103.1
72	72.3	81.6	82.8	82.1	90.9	79.7
144	56.0	56.1	61.8	59.6	68.6	58.4
Overall Nu						73.0

Table 6.14 Nu of oscillating case $v = 4.78 m/s$

Angle	1	2	3	4	5	angle average
-144	50.4	59.1	61.3	61.7	68.2	58.1
-72	59.7	66.9	65.2	63.8	71.6	63.9
0	99.3	101.5	108.0	104.3	112.4	103.3
72	71.2	80.8	82.8	80.4	90.1	78.8
144	51.7	54.9	60.4	62.5	68.0	57.4
Overall Nu						72.3

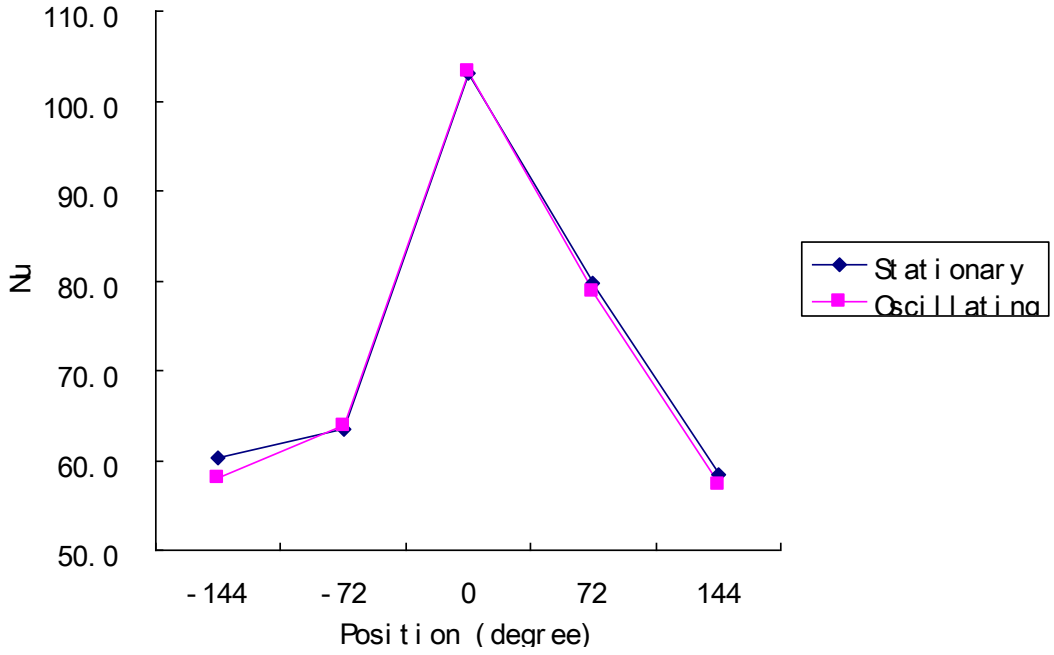

Figure 6.7 Average Nu comparison for stationary and oscillating cases $v = 4.78m/s$

Analysis for transient Nu of the oscillation and stationary cases are shown in Figure 6.8 and 6.9 for $v = 1.95m/s$ and $v = 4.78m/s$, respectively. The transient Nu, which is taken at leading edge of the cylinder, is plotted against the cylinder motion. The cylinder motion curve is sinusoidal function. The dimensionless amplitude of the cylinder in Figure 6.8 and 6.9 is from 1 to -1, which means the cylinder moves from vertical position to horizontal position. The length of the cylinder is 10 inches (25.4 cm), so the distance which the cylinder tip travels is 39.9 cm. The slope of the motion curve represents the transient velocity of the cylinder at certain point. Typically, the cylinder has maximal speed at middle point (amplitude equals zero), and no speed at vertical and horizontal positions (amplitude equals -1 and 1). It can be seen from Figure 6.8 and 6.9 that there is no obvious trend for oscillation transient Nu, and the variation of transient Nu seems to be random. It can be concluded that transient Nu for the oscillation cylinder is not

dependent on the cylinder motion. It is also observed that the stationary Nu and oscillation Nu are very close. This is because the oscillating frequency of our system is far smaller than Strouhal number, so no obvious change on Nu is observed.

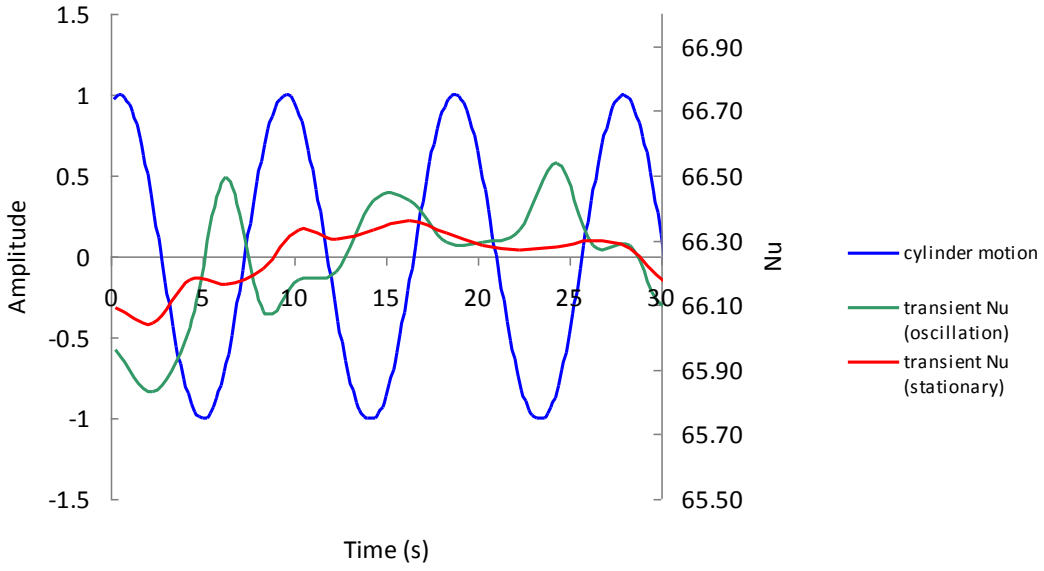

Figure 6.8 Transient Nu of oscillation and stationary cylinder $v = 1.95m/s$

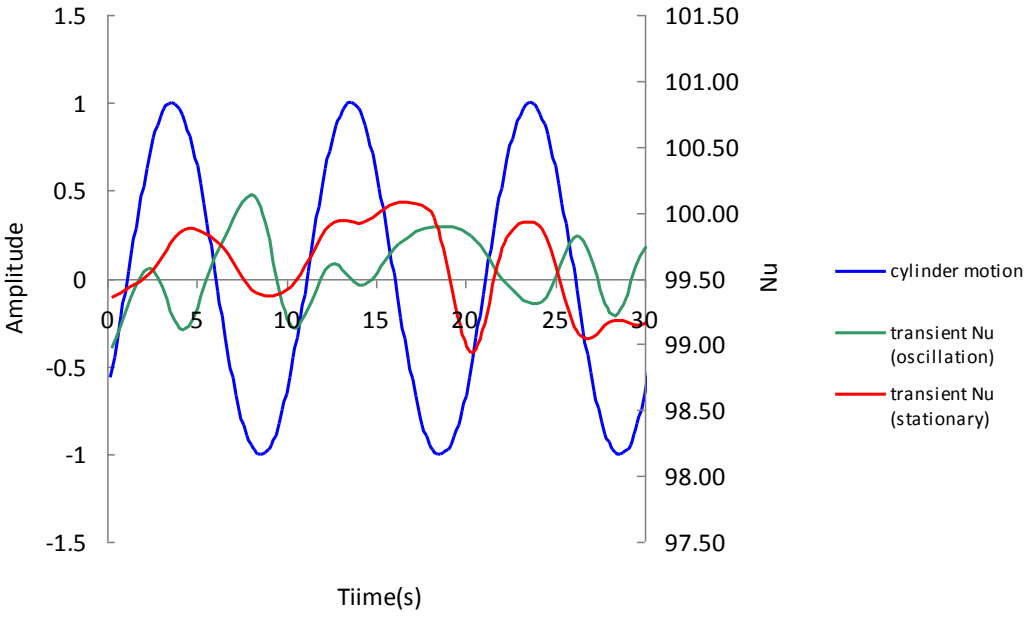

Figure 6.9 Transient Nu of oscillation and stationary cylinder $v = 4.78m/s$

6.3 Pivot experiment

The stationary and oscillating experiments have been presented in last two sections. The stationary experiment is conducted to verify the accuracy of the whole system, while the oscillating experiment simulates the human arm moving in a vertical manner. The pivot experiment is different from those two experiments because the flow boundary layer on the cylinder surface changes in the pivot experiment. In the stationary and oscillating experiments, the laminar boundary layer accumulates along the front sphere of the cylinder surface, and the separation of boundary layer occurs at about 80°. The wake becomes increasingly turbulent as Re_D increases; however, the shedding of vortices of diameter comparable with D remains a feature of the wake over most of $10^2 < \mathrm{Re}_D < 10^7$ range. The boundary layer in cross-flow case is a combination of laminar boundary layer and turbulent boundary layer. In the pivot experiment as shown in Figure 5.9 in Chapter 5, when the cylinder is at vertical position (perpendicular to bottom floor), it is a cross-flow case. The separation of the boundary layer, which is determined by $\mathrm{Re}_D = \frac{\rho UD}{\mu}$, keeps the same as that in the stationary and oscillating experiments. However, when the cylinder is at horizontal position, the boundary layer accumulates longitudinally along the cylinder, so this boundary layer can be analog to flat-plate boundary layer problem and depends on $\mathrm{Re}_x = \frac{\rho Ux}{\mu}$. The reality is that when the cylinder moves pivotally from vertical position to horizontal position, a transition of flow type and boundary layer occurs. It is not easy to find an analytical solution for this moving boundary problem because the flow type changes from laminar -- turbulent flow (vertical position) to leading edge flow (horizontal position). There are some well-recognized correlations for flow over cylinder problem (vertical position)

such as Churchill (1977), Hilpert (1933), and Zukauskas' (1972), which are mentioned in literature review. However, for axial flow over cylinder (horizontal position), the heat transfer phenomenon is still being studied. The researchers cannot even reach an agreement on velocity field distribution. Therefore, the objective for the pivot experiment is as follows: (1) study the overall and local Nu of the cylinder in the whole pivot moving process; (2) study the heat transfer phenomenon for the cylinder in horizontal position, also called axial flow over cylinder problem; (3) try to build empirical correlations to estimate overall Nu during the movement.

The pivot experiment was conducted for three different air velocity $v = 2.85 m/s$, $v = 6.01 m/s$, and $v = 10.71 m/s$, and for each velocity two frequencies, 1/14 (14 seconds per cycle) and 1/28 (28 seconds per cycle), were applied. As described in the experimental setups, when the cylinder was moving pivotally, each heat flux sensor was positioned at leading edge in turn, so there were five sets of data for at each angle, just the same configurations as for the stationary and oscillating experiments. At each angle, the stationary Nu numbers were taken at vertical and horizontal positions before pivot movement was applied. The average Nu numbers were still from the average of five locations.

Table 6.15 - 6.20 shows the average Nu for three wind velocity $v = 2.85 m/s$, $v = 6.01 m/s$, and $v = 10.71 m/s$ with the cylinder moving at two frequency 1/14 and 1/28. In each table, column 2 -5 represent five measuring positions on the cylinder, and row 2-4 represent three cases: still cylinder at horizontal position, still cylinder at vertical position, and cylinder in pivot movement. Overall Nu is calculated for three cases. Figure 6.10 - 6.15 are plots of Nu against angles for each case. For pivot experiment, we also concern the transient local Nu of the cylinder. Figure 6.16 - 6.21 show the transient Nu at leading edge (0^{o}) versus cylinder motion.

These figures are based on the transient data collected by LABVIEW as described in apparatus section, and the data acquisition interval is 1 second.

For $v = 2.85 m/s$ f=1/14, it can be seen from Table 6.15 and Figure 6.10 that for "Still horizontal" case, Nu numbers at all positions are very close. This is because the five heat flux sensors are located symmetrically around the cylinder circumference. However, just like in stationary case, natural convection exists, and may affect local Nu of the cylinder. In Table 6.15, Nu at 0° is 39.7, the lowest point among the five positions, since this position is on the bottom of the cylinder as shown in Figure 5.4. The other four spots are affected by natural convection, so Nu numbers are higher than Nu of bottom position. "Still vertical" case is also "flow over cylinder" problem, the same as in stationary case. The difference of this two cases are: in stationary case, top positions are affected by natural convection phenomenon, so Nu numbers at 72° and -72° don't show symmetrical trend (Nu at bottom is lower); in "still vertical" case, all five positions are affected by natural convection along the cylinder axis, so theoretically they should have equal Nu. Therefore, it can be seen from Figure 6.10 that "still vertical" case has a similar curve to stationary case; "still horizontal" case has a flat curve; and "pivot moving" curve is just in between. "Still vertical" curve in Figure 6.10 shows a symmetrical trend at 72° and -72°.

It is also noted that at 144° and -144° three cases show very close Nu numbers. This may be a coincidence because the boundary layer and heat transfer for horizontal and vertical cylinder are very different. The overall Nussel numbers for three cases are listed in the last column in the table. It is observed that Nu of pivot moving is closer to Nu of "still vertical" than that of "still

horizontal". After analyzing all the data, we are trying to find a correlation for overall Nu of pivot moving.

Table 6.16 and Figure 6.11 show overall Nu for $v = 2.85 m/s$ and f=1/28. The frequency is 1/28, which means the average velocity of cylinder is 1/2 slower than that in Table 6.15. In general, a slower wind velocity leads to a smaller Nu. However, results from vertical experiment indicate that Nu won't have an obvious change if the oscillating frequency is not close to Strauhal number. Strauhal number is proved to be valid for vertical oscillation, and for pivot motion its validity needs to be verified. It is found that overall Nu of pivot moving case from Table 6.15 is 1.7% higher than that in Table 6.6, which cannot be considered an obvious change. There is another observation that for pivot moving case, local Nu at 72°, -72°, 144°, and -144° are very close, and approximate 25% lower than Nu at 0°.

The Nu numbers in Figure 6.10 and 6.11 can be compared to Danielsson's experimental data presented in literature review. It can be seen from Figure 6.10 and 6.11 that (1) Nu number reaches maximal value at leading edge, and decreases along the cylinder circumference (2) Nu number of pivotal moving cylinder is less than Nu number of cylinder in vertical position. Recall Figure 2.5 and 2.6 in Chapter 2. The above observations also applies to Figure 2.5 and 2.6, except that Figure 2.5 and 2.6 use convection coefficient instead of Nu number. Although the conditions of two experiments are different, the trend of local heat transfer coefficients is consistent.

For $v = 6.01 m/s$ f=1/14 case as shown in Figure 6.12 and Table 6.18, Nu for "still horizontal", "still vertical", and pivot moving cases are 62.0, 74.6, and 69.4, which is higher than $v = 2.85 m/s$ case, as expected. When the cylinder is positioned horizontally, Nu also shows the

same trend as in last case. The standard deviation of Nu for five locations is 2.25, or 3.6% of average, which indicates that Nu is only slightly changed for "still horizontal" case. Average Nu for pivot moving f=1/28 case is 68.9, which is 0.5 (or 0.7%) lower than f=1/14 case. It is worthy to notice that average Nu of "still horizontal" case is 62.0 and 59.8 for f=1/14 and f=1/28, respectively. The difference is 5.1%. To explain this, we recall the uncertainty analysis in Chapter 5. The maximal uncertainty due to systematic and random error is ±4.1% and ±3.2%, respectively. The total uncertainty of the system is ±7.3%, which means for two separate measurements, the maximal difference may reach 7.3%. Therefore, the observation of 5.1% on Nu difference is acceptable.

The similar analysis can be applied to $v = 10.71 m/s$ case. Nu increases with the increasing of wind speed. A different observation from Figure 6.14 and 6.15 is that when the cylinder is positioned horizontally, Nu numbers of five locations are not as close as in last two cases. Table 6.21 shows average Nu, standard deviation of Nu, and the ratio of standard deviation to average Nu. It can be seen that the ratio of $v = 2.85 m/s$ and $v = 6.01 m/s$ cases is no more than 3.64%, but ratio of $v = 10.71 m/s$ case is 5.15% and 6.11% for different frequencies. The reason might be: for high velocity case, the turbulent boundary layer forms earlier along the cylinder than low velocity case, and more cylinder area is covered by turbulent flow. It has been proved that turbulent flow will result in a more unsteady velocity distribution, so Nu for turbulent flow is not as steady as laminar flow. Therefore, the standard deviation of Nu for high velocity flow is larger than that for low velocity flow.

We have our 6 set of pivot moving data summarized in Table 6.22. In practical application, Nu for still horizontal and still vertical cases are easy to get, either by theoretical

analysis or by experimental measurements. Therefore, it is necessary to build a correlation for Nu of pivot moving, with still horizontal Nu and still vertical Nu as inputs. Using regression analysis, correlation for pivot moving Nu is given in Equation 3-6. where Nu_{pivot}, $Nu_{horizontal}$, and $Nu_{vertical}$ are Nusselt numbers of pivot moving, still horizontal, and still vertical cases, respectively.

$$Nu_{pivot} = 0.64482 Nu_{horizonal} + 0.39891 Nu_{vertical} + 0.14312 \qquad (6\text{-}6)$$

Table 6.23 shows the comparison of Nusselt number from experimental measurements and correlation in Equation 6-6. It can be seen from Table 6.23 that the correlation results are very close to experiment results, and the maximal error is 0.75% at $v = 6.01 m/s$ f=1/28. Therefore, it is concluded that our correlation in Equation 6-6 can give good prediction on overall Nusselt number of pivot experiment with Re number ranged from 9600 to 36,000, Pr number of 0.7, and pivotal movement frequency from 1/28 to 1/14.

Table 6.15 Average Nu for three cases, $v = 2.85m/s$ f=1/14

Angle	-144	-72	0	72	144	Overall Nu
Still horizontal	40.8	41.6	39.7	43.1	42.4	41.5
Still vertical	43.2	53.4	77.3	56.2	42.7	54.6
pivot moving	45.5	46.3	61.1	47.2	42.7	48.6

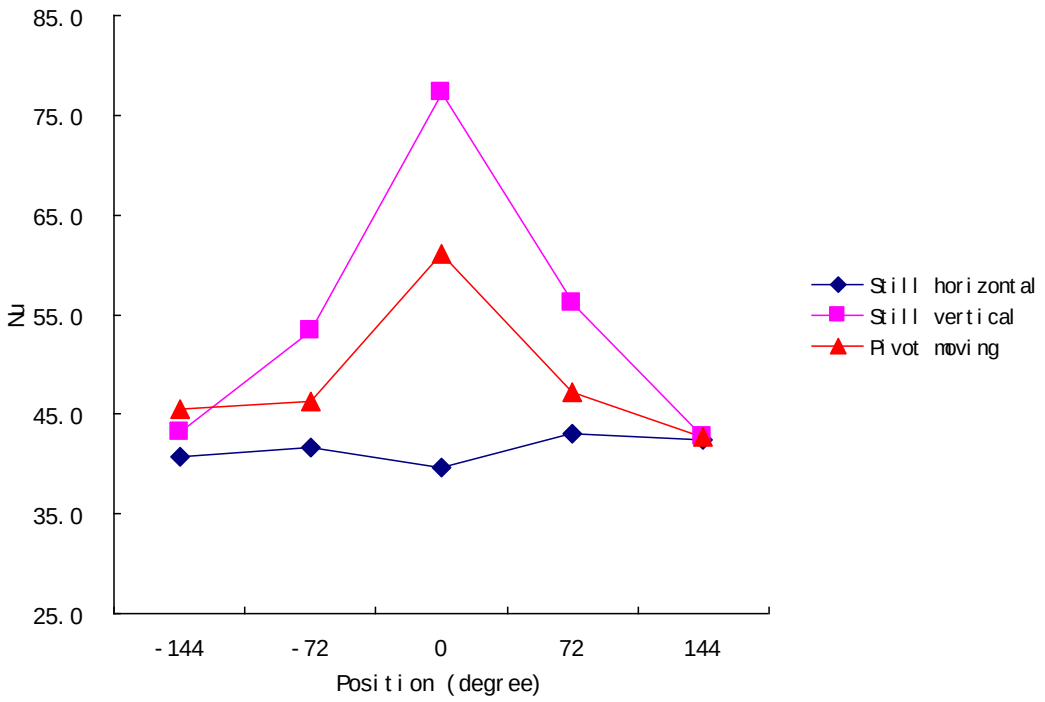

Figure 6.10 Average Nu for three cases, $v = 2.85m/s$ f=1/14

Table 6.16 Average Nu three cases, $v = 2.85 m/s$ f=1/28

Angle	-144	-72	0	72	144	Overall Nu
Still horizontal	41.2	39.6	38.3	40.1	41.0	40.0
Still vertical	44.2	52.4	75.0	56.8	45.3	54.7
pivot moving	44.6	45.8	60.2	47.3	41.3	47.8

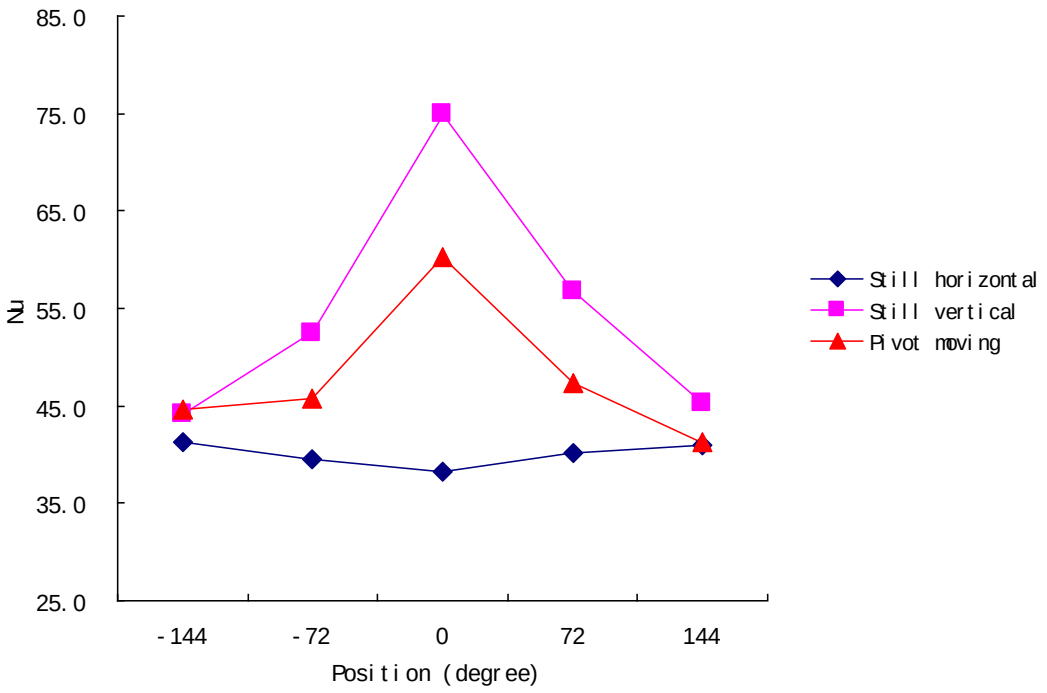

Figure 6.11 Average Nu for three cases, $v = 2.85 m/s$ f=1/28

Table 6.17 Average Nu for three cases, $v = 6.01 m/s$ f=1/14

Angle	-144	-72	0	72	144	Overall Nu
Still horizontal	62.2	58.6	61.3	63.6	64.4	62.0
Still vertical	61.4	71.1	107.8	75.5	57.0	74.6
pivot moving	64.4	66.7	86.0	66.9	63.1	69.4

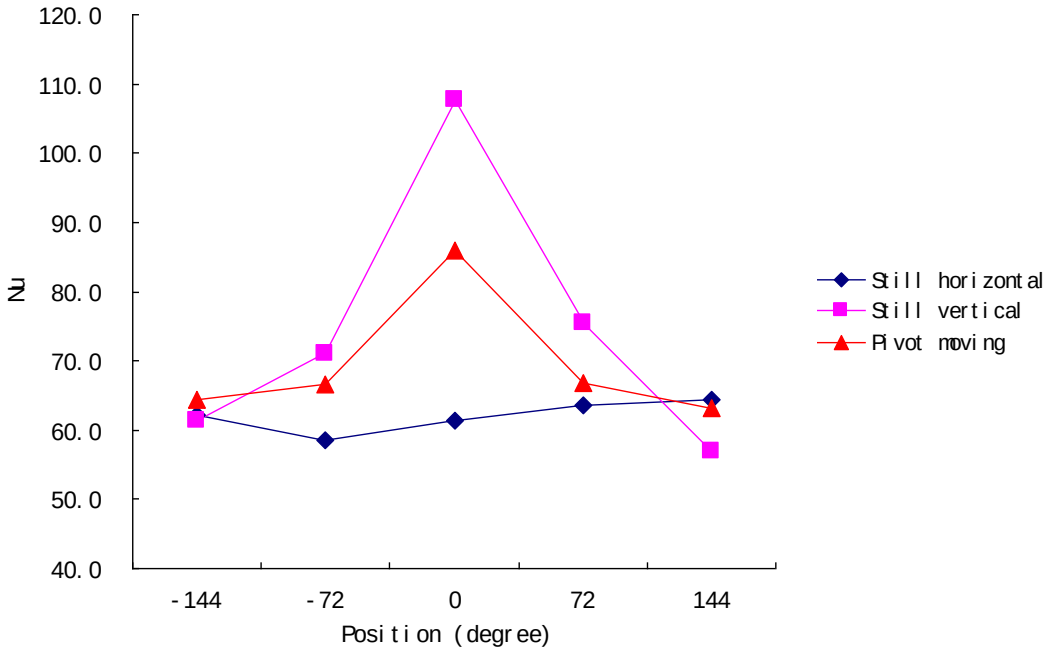

Figure 6.12 Average Nu for three cases, $v = 6.01 m/s$ f=1/14

Table 6.18 Average Nu for three cases, $v = 6.01 m/s$ f=1/28

Angle	-144	-72	0	72	144	Overall Nu
Still horizontal	60.2	58.9	57.2	61.6	61.1	59.8
Still vertical	60.7	75.2	103.3	74.8	59.3	74.7
pivot moving	64.1	65.6	81.3	67.0	66.3	68.9

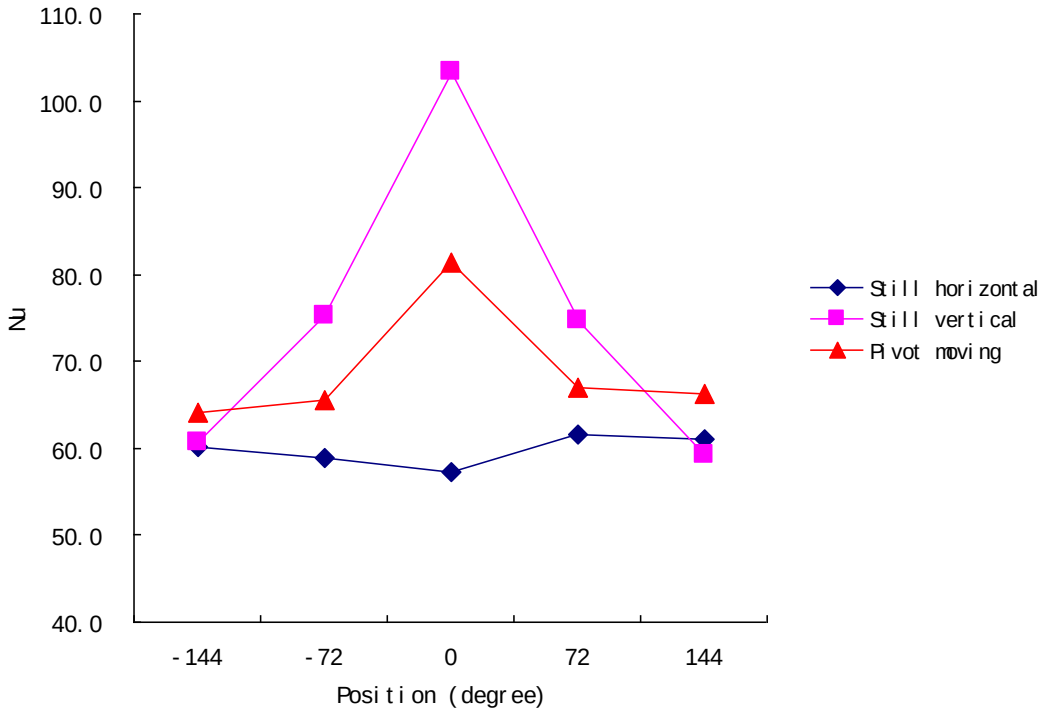

Figure 6.13 Average Nu for three cases, $v = 6.01 m/s$ f=1/28

Table 6.19 Average Nu for three cases, $v = 10.71 m/s$ f=1/14

Angle	-144	-72	0	72	144	Overall Nu
Still horizontal	118.3	108.4	109.2	103.6	114.5	110.8
Still vertical	103.4	121.6	183.8	125.8	109.1	128.7
pivot moving	125.0	111.3	149.8	111.7	121.1	123.8

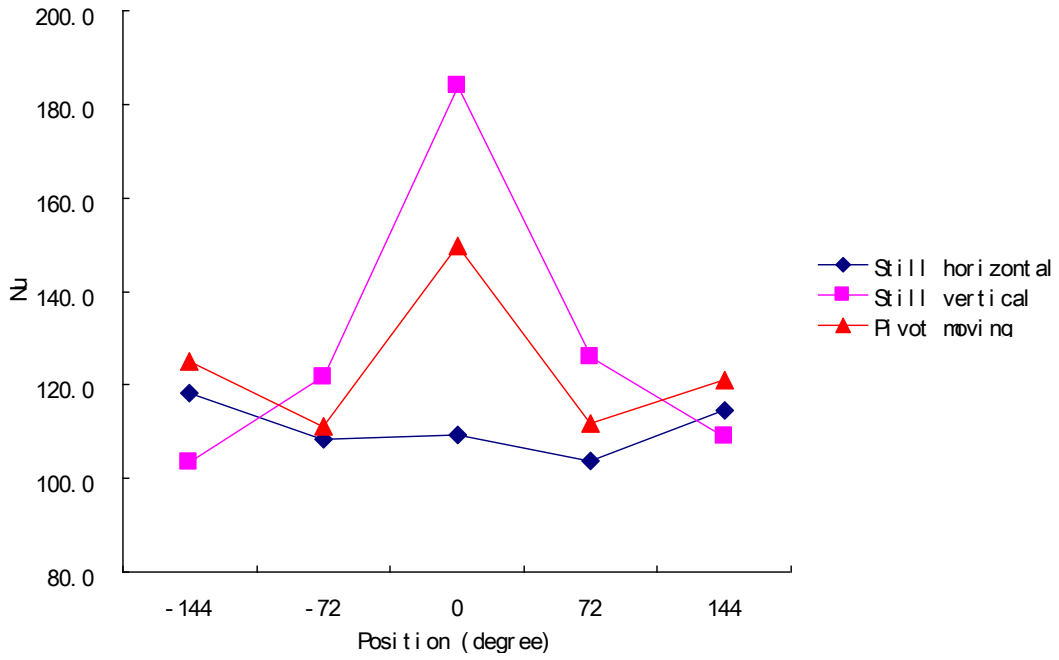

Figure 6.14 Average Nu for three cases, $v = 10.71 m/s$ f=1/14

Table 6.20 Average Nu for three cases, $v = 10.71 m/s$ f=1/28

Angle	-144	-72	0	72	144	Overall Nu
Still horizontal	117.4	103.9	105.6	101.3	112.3	108.1
Still vertical	99.4	119.2	178.3	123.0	103.7	124.7
pivot moving	123.5	107.3	146.1	110.4	114.9	120.4

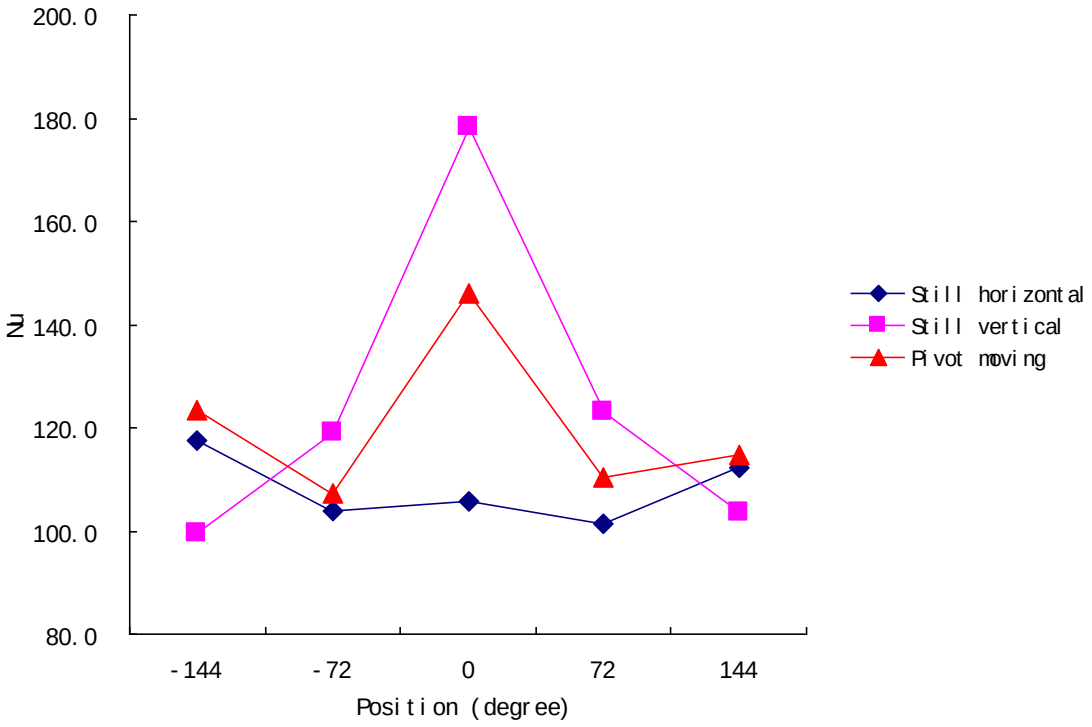

Figure 6.15 Average Nu for three cases, $v = 10.71 m/s$ f=1/28

Table 6.21 Analysis of standard deviation for still horizontal case

Pivot experiment	Average Nu	Standard deviation	Ratio (%)
v=2.85m/s f=1/14	41.52	1.33	3.21
v=2.85m/s f=1/28	40.04	1.17	2.93
v=6.01m/s f=1/14	62.02	2.26	3.64
v=6.01m/s f=1/28	59.80	1.78	2.97
v=10.71m/s f=1/14	110.80	5.70	5.15
v=10.71m/s f=1/28	108.10	6.60	6.11

Table 6.22 Average Nu for still horizontal, still vertical, and pivot moving

Case	Still horizontal	Still vertical	Pivot moving
v=2.85 f=1/14	41.5	54.6	48.6
v=6.01 f=1/14	62.0	74.6	69.4
v=10.71 f=1/14	110.8	128.7	123.8
v=2.85 f=1/28	40.0	54.7	47.8
v=6.01 f=1/28	59.8	74.4	68.9
v=10.71	108.1	124.7	120.4

f=1/28

Table 6.23 Nu comparison of experiment results and correlation

Case	Nu from EXP	Nu from correlation	% of error
v=2.85 f=1/14	48.6	48.7	0.17
v=6.01 f=1/14	69.4	69.9	0.69
v=10.71 f=1/14	123.8	122.9	-0.70
v=2.85 f=1/28	47.8	47.8	-0.09
v=6.01 f=1/28	68.9	68.4	-0.75
v=10.71 f=1/28	120.4	119.6	-0.67

Figures 6.16 -6.21 show plots of transient Nu and cylinder motion against time. Transient Nu is taken at the leading edge when the cylinder is vertically positioned. The cylinder motion curve is also sinusoid function, the same as in the oscillating experiment. It can be observed from all three figures that transient Nu is always 0.7 - 1.0 second behind the cylinder motion. There are three main reasons for this delay: (1) according to users' manual, the heat flux sensor has a 0.2 second for response time. This means that when the thermal status is changed, it takes at least 0.2 second for heat flux sensor to react and get correct readings. (2) As discussed in previous section, for pivot experiment, transition of boundary layer occurs when the cylinder moves from horizontal position to vertical position. However, this transition is not immediate, and it takes sometime for the boundary layer to reform and then the temperature distribution is updated. This process can be very fast, but it still play a role for the delay. (3) Accumulated delaying time occurs in data acquisition, such as scanning delay from HP unit, control delay from LABVIEW, etc. Another observation is that transient Nu increases when the cylinder moves from horizontal

position to vertical position, and reaches maximal value at vertical position; while transient Nu decreases when the cylinder moves from vertical position to horizontal position, and reaches minimal value at horizontal position. This means that the heat transfer of cross-flow cylinder is stronger than that of axial-flow cylinder.

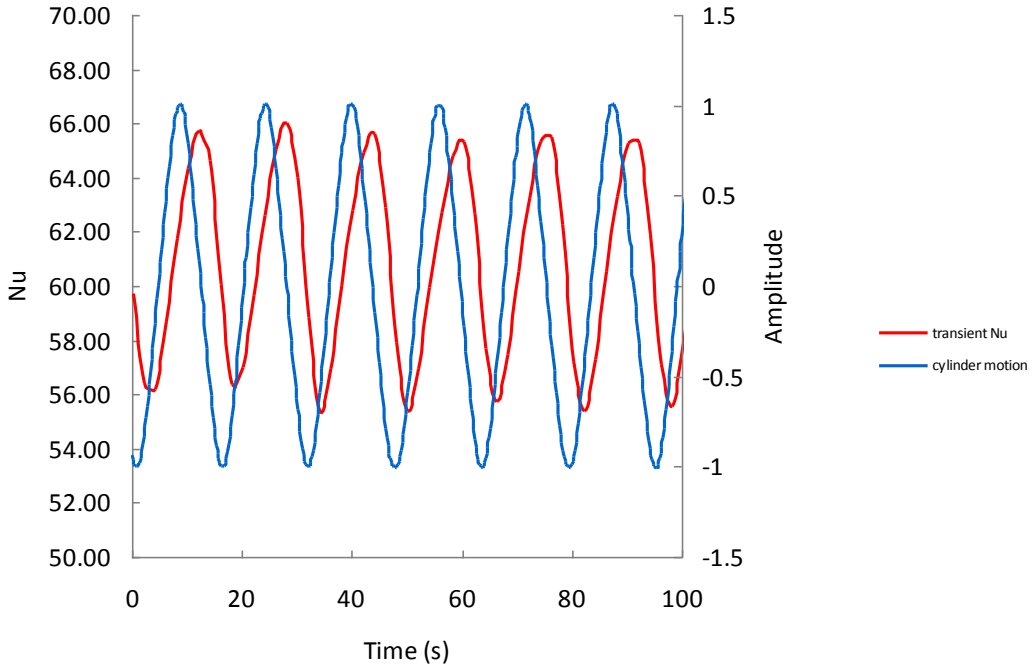

Figure 6.16 Transient Nu versus cylinder motion, $v = 2.85 m/s$ **f=1/14**

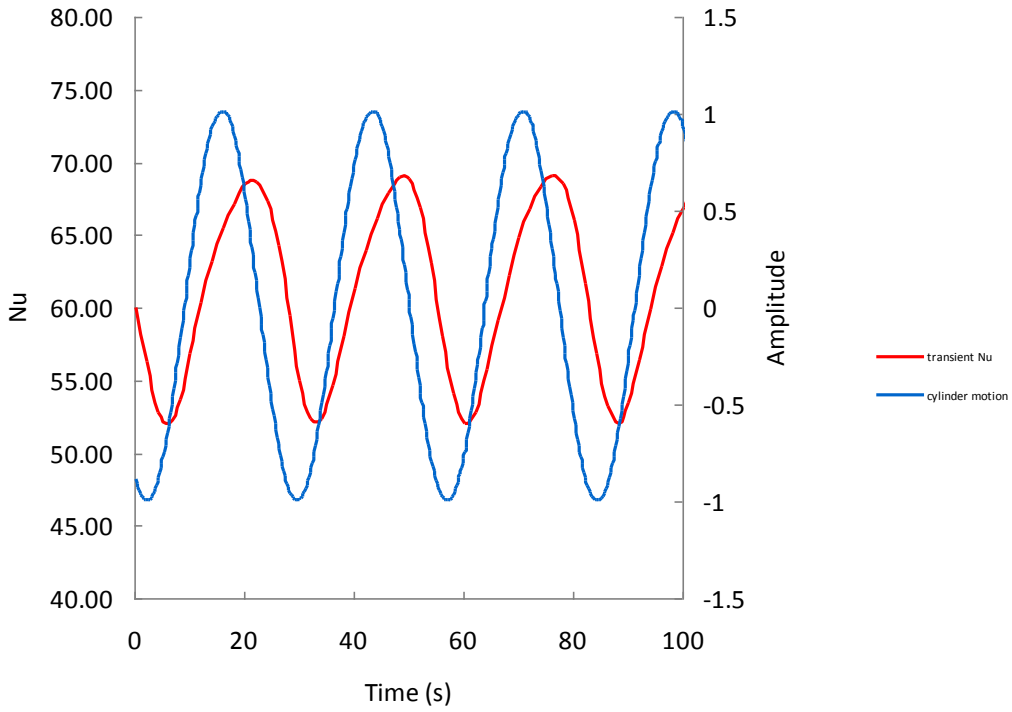

Figure 6.17 Transient Nu versus cylinder motion, $v = 2.85 m/s$ **f=1/28**

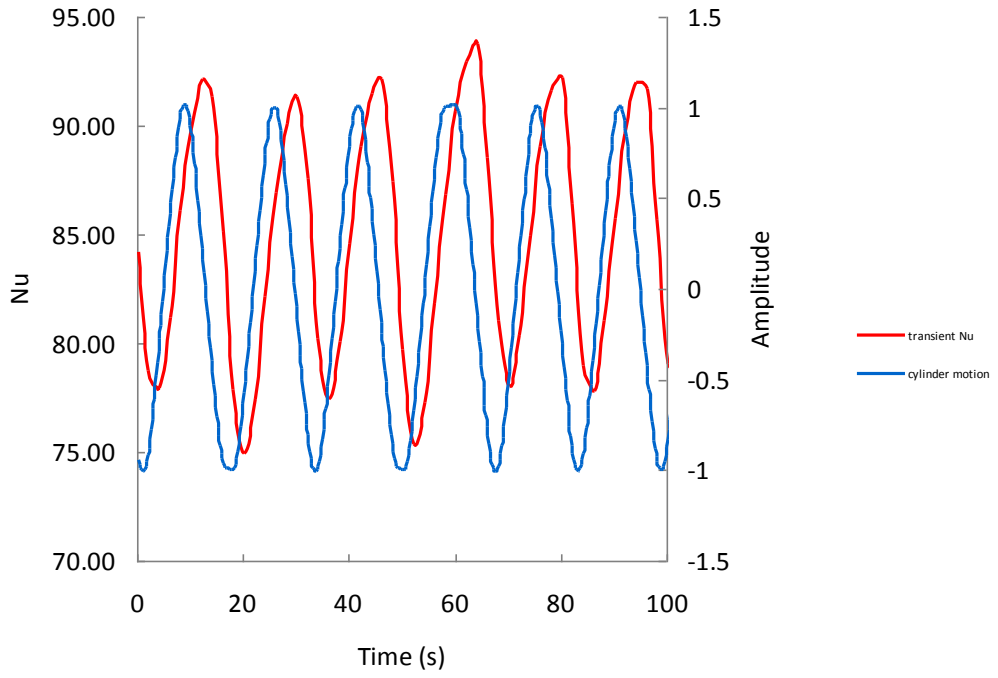

Figure 6.18 Transient Nu versus cylinder motion, $v = 6.01 m/s$ **f=1/14**

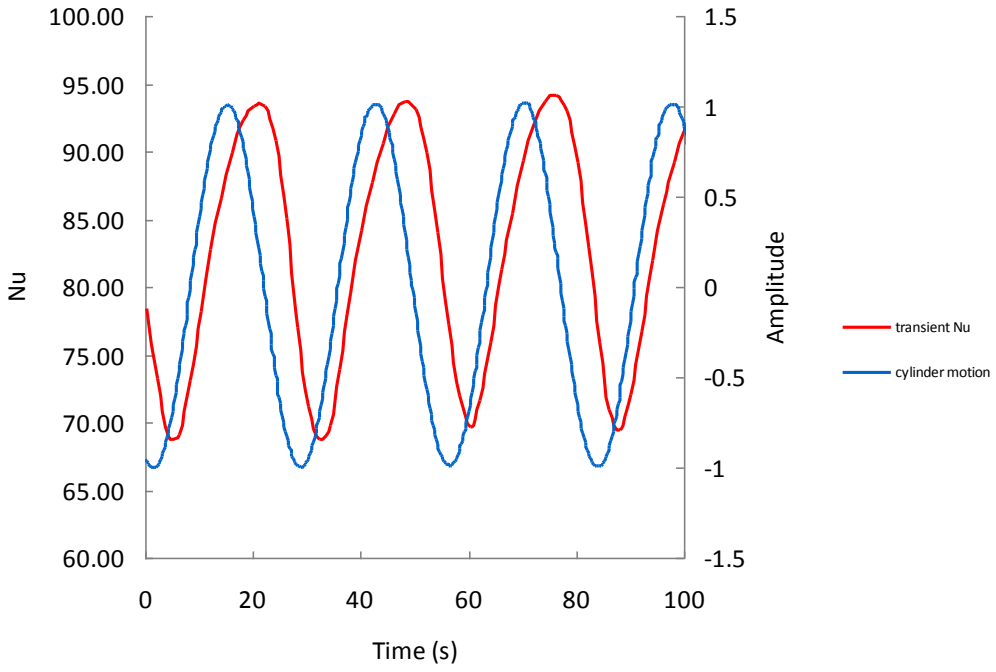

Figure 6.19 Transient Nu versus cylinder motion, $v = 6.01 m/s$ **f=1/28**

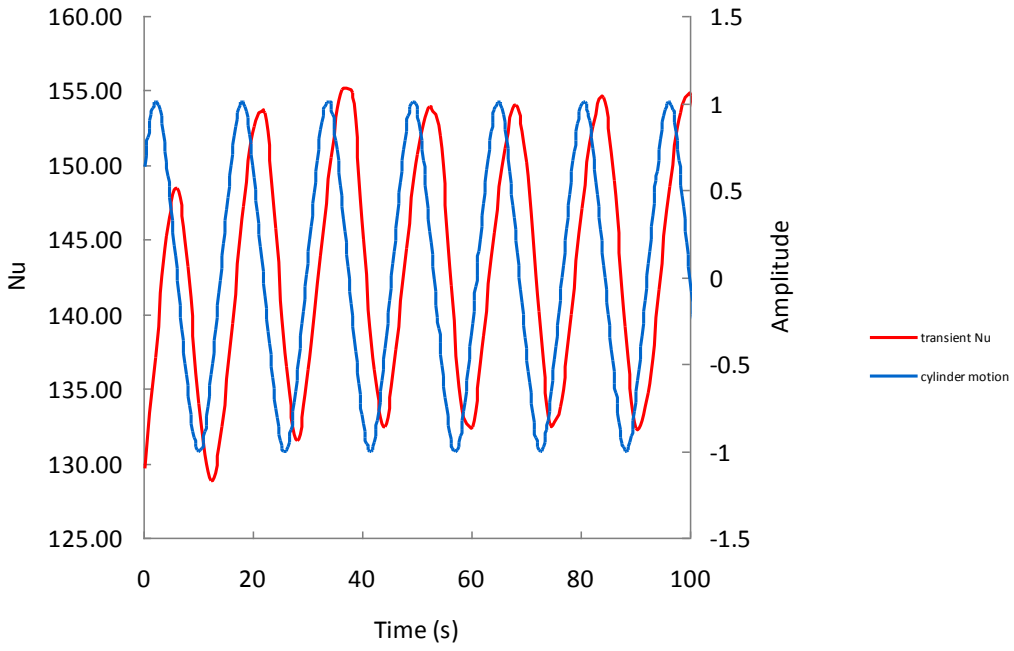

Figure 6.20 Transient Nu versus cylinder motion, $v = 10.71 m/s$ **f=1/14**

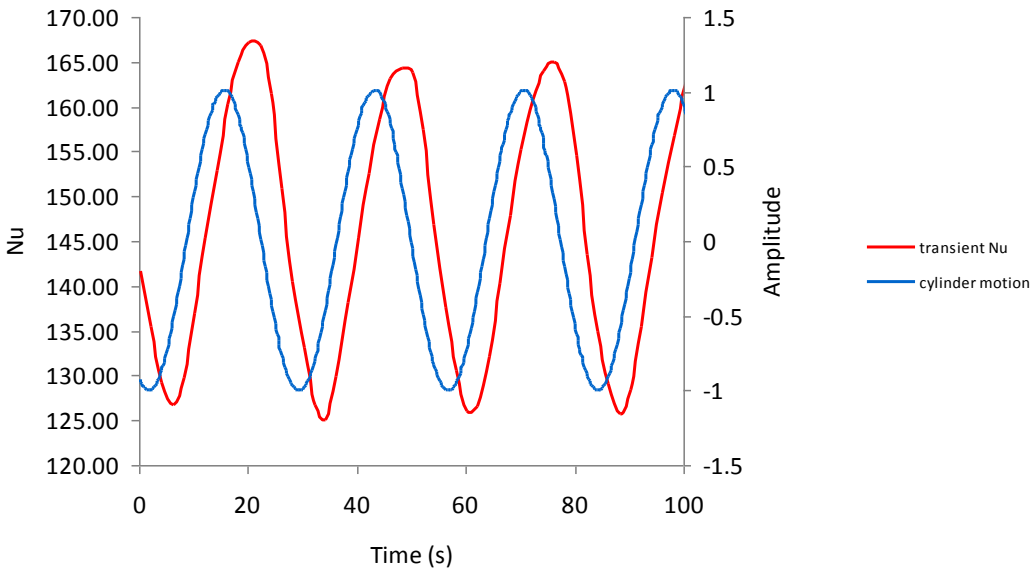

Figure 6.21 Transient Nu versus cylinder motion, $v = 10.71 m/s$ **f=1/28**

Chapter 7 - Conclusion

The thermal model was able to predict thermal behavior of the human body when exposed to a uniform environment. The transient temperature profiles predicted by our model showed good agreement with Zhang's experiment data (Zhang 2003) in neutral and warm conditions. In cold condition, our hand temperature kept constant during the test, while the experiment showed a descending trend for hand. The steady-state temperatures by our refined-shape model showed better agreement with Zhang's experiment data than the previous model, which used cylinders to simulate body parts. In the neutral and warm tests, skin temperatures of all body parts agreed with Zhang's experiment data very well; in the cold test, the predicted temperatures still matched Zhang's data, except for distal limbs such as hand and foot. The blood flow rate through the neck was corrected in this model in order to simulate additional blood flow at the neck. This correction proved to be effective.

The follow-up experiments on the moving cylinder were able to provide convective heat transfer coefficient or Nusselt number to the thermal model. In the validation experiment of a stationary cylinder in cross flow, the overall Nu from our data showed very good agreement with Churchill (1977), Hilpert (1933), and Zukauskas' (1972) empirical correlations. In the case of a transverse-moving cylinder in cross flow, Nu remained unaffected compared to the stationary case, under the conditions of Reynolds number from 6600 to 16500, Strouhal number from 0.3 to 1.5, and the oscillation frequency 0.15. This result was supported by Sreenvasan's (1961) work. The transient analysis indicated that the local Nu showed no periodical trend when the cylinder was oscillated. In both stationary and oscillating experiments, natural convection was found to be an nonnegligble factor in heat transfer, and it might cause 5% -10% change on the local Nusselt numbers. In the pivot experiment, the overall Nu showed a periodical trend between horizontal and vertical positions for the Reynolds number ranged from 9600 to 36,000. A correlation was presented to predict the overall Nu of a pivotal moving cylinder by using the Nu at horizontal and vertical positions in stationary state. The maximal error of the correlation was less than 1% in the range of our conditions.

In conclusion, the new thermal model allows people to use customized body shape for simulation, describes human body in more details, and provides a better prediction for both

steady-state and transient temperatures than the previous cylindrical model. There is still room to improve the model on vascular system and mechanism of vasoconstriction and shivering, if we know more about the physiological mechanism of individual body parts. The experimental investigation on the cylinder in cross flow is proved to be valid and accurate. The heat transfer coefficients (or Nu numbers) from a pivotal moving cylinder are presented for the first time. It is possible for the thermal model to simulate moving humans if the experimental data and correlations from the transverse and pivotal moving of the cylinder are applied.

References

Achenbach, E. and E. Heinecke. 1981. On vertex shedding from smooth and rough cylinder in the Reynolds number from 6×103 to 5×106. Journal of Fluid Mechanics 109: 239-251.

ASHRAE 2005. ASHRAE handbook -Fundamentals. Atlanta Georgia: American Society of Heating, Refrigerating and Air-Conditioning Engineers, Inc.

Avilio, A.P. 1980. Multi-branched model of the human arterial system. Medical & Biological Engineering & Computing 18(6): 709-718.

Atkin, A. R., and C. H. Wyndam. 1969. A study of tmeperature regulation in the human body with the aid of an analogue computer. Pflugers Archives ges. Physiology 307: 104-19.

Bearman, R.W., 1969. On vertex shedding from a circular cylinder in the critical Reynolds number regime. Journal of Fluid Mechanics 37: 577-585.

Benzinger, T.H. 1970. Peripheral cold reception and central warm reception, sensory mechanisms of behavioral and autonomic thermostasis. Physiological and Behavioral Temperature Regulation Chapter 56: 831-55. Illinois: Charles C. Thomas Publishing Company.

Charny, C.K., M.J. Hagmann, and R.L. Levin. 1987. A whole body thermal model of man during hyperthermia. IEEE Transactions on Biomedical Engineerin BME-34(5): 375-87.

Cheng, C.H., H.N. Chen, and W. Aung. 1997. Experimental study of the effect of transverse oscillation on convection heat transfer from a circular cylinder. Journal of Heat Transfer, Transaction ASME 119 (3): 474-482.

Churchill S. W., M. Bernstein. 1977. Correlation equations for forced-convection from gases and liquid to a circular-cylinder in cross flow. Journal of Heat Transfer 99(2): 300-306.

Danielsson, Ulf. 1993. Convection coefficients in clothing air layers. Ph.D dissertation. Te Royal Institute of Technology.

Fiala, D., K.J. Lomas, and M. Stohrer. 2001. Computer prediction of human thermoregulatory and temperature responses to a wide range of environmental conditions. International Journal of Biometeorolog 45(3): 143-159.

Fu, G. 1995. A transient, 3-D mathematical thermal model for the clothed human, Ph.D dissertation. Kansas State University.

Gagge, A.P., J.A. Stolwijk, and Y. Nishi. 1971. An effective temperature scale based on a simple model of human physiological regulatory response. ASHRAE Transactions 77 Part I: 247-262.

Ganong, W.F. 1983. Review of Medical Physiology, 11th ed. Los Altos, California: LANGE Medical Publications.

Gau, C., J.M. Wu, and C.Y. Liang. 1999. Heat transfer enhancement and vortex flow structure over a heated cylinder oscillating in the crossflow direction. Journal of Heat Transfer, Transaction ASME 121 (4): 789-795.

Gordon, R.G. 1974. The response of a human temperature regulatory system model in the cold. Ph.D dissertation. University of California, Santa Barbara.

Hall, J.F. and F.K. Klemm. 1969. Thermal comfort in disparate thermal environments. Journal of Applied Physiology 27(5): 601-06.

Hardy, J.D. and J.A. Stolwijk. 1966. Partitional calorimetric studies of man during exposures to thermal transients. Journal of Applied Physiology 31(6): 1799-1806.

Hardy, J.D. and E.F. Dubois. 1938. The technique of measuring radiation and convection. Journal of Nutrition 15: 461-475.

Higuchi, H., P. van Langen, H. Sawada, and C. E. Tinney. 2006. Axial flow over a blunt circular cylinder with and without shear layer reattachment. Journal of Fluids and Structures 22: 949-959.

Hilpert, R. 1933. Forsch. Geb. Ingenieurwes 4: 215.

Jones, B.W. and Y. Ogawa. 1992. Transient interaction between the human and the thermal environment, ASHRAE trans., 98, Part1.

Jones, B.W., Y. Ogawa and E. A. McCullough. 1993. Transient in clothing system, submitted to Textile Research Journal.

Kays, W. M., M. E. Crawford and B. Weigand. 2005. Convective heat and mass transfer, 4th ed. McGraw-Hill Higher Education, Boston.

Kezios, S.P. and K.V. P. Prasanna. 1966. Effect of vibration on heat transfer from a cylidner in normal flow. 66-WA/HT-43, ASME Paper No.

Kim, H.J. 1986. An experimental investigation on the flow around a circular cylinder in the first critical subregion. Ph.D dissertation. The Faculty of the Graduate school of the University of Minnesota, Minnesota.

Kiya, M. and K. Sasaki. 1983. Structure of a turbulent separation bubble. Journal of Fluid Mechanics 137: 83-113.

Kiya, M., O. Mochizuki, H. Tamura, R. Ishikawa, K. Kushioka. 1991. Turbulence properties of an axisymmetric separation and reattaching flow. AIAA Journal 29(6): 936-941.

Lichtenbelt, W.D., A.J.H. Frijns, D. Fiala, F.E.M. Janssen, M.J. van Ooijen and A.A. van Steenhoven. 2004. Effect of individual characteristics on a mathematical model of human thermoregulation. Journal of Thermal Biology 29(7-8): 577-581.

Lichtenbelt, W.D., A.J.H. Frijns, M.J. van Ooijen, D. Fiala, A.M. Kester, A.A. van Steenhoven. 2007. Validation of an individualised model of human thermoregulation for predicting responses to cold air. International Journal of Biometeorology 51(3): 169-179.

Mills, R., J. Sheridan, and K. Hourigan. 2002. Response of base suction and vortex shedding from rectangular prisms to transverse forcing. Journal of Fluid Mechanics 461: 25-49.

Morgan, V. T., 1975. The overall convective heat transfer from smooth circular cylinders. Advances in Heat Transfer, Vol 11. Academic Press, New York.

Ota, T. 1975. An axisymmetric separated and reattached flow on a longitudinal blunt circular cylinder. Journal of Applied Mechanics (June): 311-315.

Park, H.G. and M. Gharib. 2001. Experimental study of heat convection from stationary and oscillating circular cylinder in cross flow. Journal of Heat Transfer, Transaction ASME 123 (1): 51-62.

Pottebaum, T.S. and M. Gharib. 2006. Using oscillations to enhance heat transfer for a circular cylinder. Journal of Heat and Mass Transfer 49: 3190-3210.

Ramanujan, S. 1913. Modular Equations and Approximations toπ. Quarterly Journal of Pure and Applied Mathematics 45: 350-372.

Salloum, M., N. Ghaddar, and K. Ghali. 2007. A new transient model of the human body and its integration to clothing models. International Journal of Thermal Sciences 46(4): 371-384.

Saltin, B. and L. Hermansen. 1966. Esophageal, rectal and muscle temperature during exercise. Journal of Applied Physiology 21(6): 1757-62.

Sanitjai, S. and R. J. Goldstein. 2004. Forced convection heat transfer from a circular cylinder in cross flow to air and liquid. International Journal of Heat and Mass Transfer 47: 4795-4805.

Sarioglu, M. and T. Yavuz. 2000. Vortex shedding from circular and rectangular cylinders placed horizontally in a turbulent flow. Turk. J. Engin. Environ. Sci. 24: 217-228.

Saxena, U.C. and A.D.K. Laird. 1978. Heat transfer from a cylinder oscillating in a cross flow. Journal of Heat Transfer, Transaction ASME 100 (4): 684-689.

Segerlind, L.J. 1984. Applied Finite Element Analysis, 2nd ed. New York: John Wiley & sons.

Sheridan, J., K. Hourigan, and R. Mills. 1997. Vortex structures in flow over a rectangular plate. ASME97-FSI, ASME Meeting, Dallas, TX, USA.

Smith, C.E. 1991. A transient three-dimensional model of the human thermal system, Ph.D dissertation. Kansas State University.

Sreenivasan, K. and A. Ramachandran. 1961. Effect of vibration on heat transfer from a horizontal cylinder to a normal air stream. International Journal of Heat and Mass Transfer 3: 60-67.

Stolwijk, J.A. and J. D. Hardy. 1966. Temperature regulation in Man – a theoretical study. Pflugers Archives ges Physiology, 291: 129-162.

Stolwijk, J.A. 1970. Mathematical model of thermoregulation, physiological and behavioral temperature regulation Chapter 48: 703-721. Illinois: Charles C. Thomas Publishing Company.

Williamson, C. H. K. and A. Roshko. 1988. Vortex formation in the wake of an oscillating cylinder. Journal of Fluids Structure 2: 355-381.

Wissler, E.H. 1964. A mathematical model of the human thermal system. Bulletin of Mathematical Biophysics 26(2): 147-166.

Wissler, E.H. 1966. The use of finite difference techniques in simulating the human thermal system. Physiological and Behavioral Temperature Regulation Chapter 27, 367-388.

Wissler, E.H. 1985. Mathematical simulation of human thermal behavior using whole body models. Heat and Mass Transfer in Medicine and Biology Chapter 13: 325-373. New York: Plenum Press.

Yi, L., F.Z. Li, Y.X. Liu, and Z.X. Luo. 2004. An integrated model for simulating interactive thermalprocesses in human-clothing system. Journal of Thermal Biology 29(7-8): 567-575.

Zhang, H. 2003. Human thermal sensation and comfort in transient and non-uniform thermal environments, Ph.D dissertation. University of California, Berkeley.

Zhang, N, Z. C. Zheng, and S. Eckels. 2008. Study of heat-transfer on the surface of a circular cylinder in flow using an immersed-boundary method. International Journal of Heat and Fluid Flow, 29 (6): 1558-1566.

Zukauskas, A. 1972. Heat transfer from tube in cross flow. Advances in Heat Transfer 8: 116-133. Academic Press, New York.

Zukauskas, A. 1987. Convective heat transfer in cross flow. Handbook of Single-Phase Convective Heat Transfer. Wiley, New York.

Appendix A - Leotard ensemble

Leotard content is usually cotton, polyester, lycra, and polyamide, etc. It is also possible to be the combination of several material such as 80% cotton + 20% lycra and 76% polyamide + 24% lycra. In our experiment, we assume the material of leotard is 100% polyester, for the purpose of simplicity.

Properties of leotard needs to be figured out to create the leotard database for our model The main properties used in the model are thickness (cm), dry resistance (m2·K/W or in clo), evaporative resistance (m2·kPa/W), specific heat (J/g·K), and area density (kg/m2). The dry resistance of material can be determined by Equation A-1, given by McCullough and Jones (McCullough 1984).

$$I_{clu,I} = (0.534 + 0.135x_f)(A_G / A_D) - 0.0549 \qquad \text{A-1}$$

In Equation A-1, x_f is fabric thickness in mm; A_G is body surface area covered by cloth; A_D is total body area. The leotard in our experiment covers torso, arm, thigh, calf, and foot of the body. The property evaluation of each body part is shown in Table A.1.

Table A.1 Properties of leotard

	Thickness (cm)	clo	Rf	Ref	Cp	Weight	radius
torso	0.500	0.600	0.047	0.015	0.400	150.000	13.500
u.arm	0.278	0.300	0.047	0.015	0.400	83.333	4.778
l.arm	0.219	0.220	0.047	0.015	0.400	65.556	3.919
thigh	0.219	0.220	0.047	0.015	0.400	65.556	6.919
calf	0.248	0.260	0.047	0.015	0.400	74.444	4.548
foot	0.433	0.510	0.047	0.015	0.400	130.000	4.033

1 clo = 0.155 m2·K/W

Appendix B - Specifications of heat flux sensor HFS-4

Table B.1 HFS-4 specifications

Model No.	Nominal sensitivity ($\mu V/Btu/Ft^2 \cdot Hr$)	Max. Heat flux ($Btu/Ft^2 \cdot Hr$)	Built-in Type-K thermocouple	Response time (s)	Thermal capacitance $Btu/Ft^2 \cdot F$	Thermal resistance $F/Btu/Ft^2 \cdot Hr$	Nominal thickness mm (inch)
HFS-4	6.5	30,000	Yes	0.20	0.02	0.01	0.18 (0.007)

Appendix C - Tables for moving cylinder experiments

Table C.1 Stationary experiment for $v = 3.81 \text{m/s}$ and HFS#1 at leading edge

1	Room Temperature (°C)	22.19				
2	HFS #	1	2	3	4	5
3	Angle (0° at leading edge)	0	-72	-144	144	72
4	Surface Temperatrue(°C)	34.79	37.15	38.25	38.85	37.21
5	HFS Temperature (°C)	36.77	38.69	39.5	39.63	38.73
6	HFS Reading(μV)	523.23	448.96	410.88	460.32	592.14
7	HFS sensitivity(μV/W/m2)	0.785	0.888	0.893	0.927	0.906
8	Temperature for calculation (°C)	28.49	29.67	30.22	30.52	29.7
9	corrected factor (μV/W/m2)	0.787	0.889	0.894	0.927	0.907
10	Air conductivity k (W/m K)	0.026	0.026	0.026	0.026	0.026
11	q"(W/m2)	599.88	454.41	413.78	446.72	587.43
12	h(W/m2K)	47.61	30.37	25.76	26.81	39.11
13	local Nu	93.0	59.3	50.3	52.4	76.4
14	Overall Nu	66.3				

Table C.2 Stationary experiment for $v = 3.81 \text{m/s}$ and HFS#2 at leading edge

1	Room Temperature (°C)	22.19				
2	HFS #	1	2	3	4	5
3	Angle (0° at leading edge)	72	0	-72	-144	144
4	Surface Temperatrue(°C)	37.18	36.63	38.05	38.99	39.45
5	HFS Temperature (°C)	39.03	39.02	39.33	39.73	40.29
6	HFS Reading(μV)	471.67	681.13	468.42	401.56	430.98
7	HFS sensitivity(μV/W/m2)	0.785	0.888	0.893	0.927	0.906
8	Temperature for calculation (°C)	29.685	29.41	30.12	30.59	30.82
9	corrected factor (μV/W/m2)	0.786	0.889	0.894	0.927	0.906
10	Air conductivity k (W/m K)	0.026	0.026	0.026	0.026	0.027
11	q"(W/m2)	540.04	689.20	471.68	389.72	428.08
12	h(W/m2K)	36.03	47.73	29.74	23.20	24.80
13	local Nu	70.4	93.3	58.1	45.3	48.5
14	Overall Nu	63.1				

Table C.3 Stationary experiment for $v = 3.81 \text{m/s}$ and HFS#3 at leading edge

1	Room Temperature (°C)	22.31				
2	HFS #	1	2	3	4	5
3	Angle (0° at leading edge)	144	72	0	-72	-144
4	Surface Temperatrue(°C)	41.69	40.7	38.94	40.49	41.81
5	HFS Temperature (°C)	43.04	42.97	41.29	41.5	42.84
6	HFS Reading(μV)	407.67	693.88	758.79	545.67	530.13
7	HFS sensitivity(μV/W/m2)	0.785	0.888	0.893	0.927	0.906
8	Temperature for calculation (°C)	31.94	31.445	30.565	31.34	32
9	corrected factor (μV/W/m2)	0.784	0.888	0.893	0.927	0.905
10	Air conductivity k (W/m K)	0.027	0.027	0.026	0.027	0.027
11	q"(W/m2)	467.91	703.65	764.44	530.01	527.23
12	h(W/m2K)	24.14	38.26	45.97	29.15	27.04
13	local Nu	47.2	74.8	89.8	57.0	52.8
14	Overall Nu	64.3				

Table C.4 Stationary experiment for $v = 3.81\text{m/s}$ and HFS#4 at leading edge

1	Room Temperature (°C)	22.54				
2	HFS #	1	2	3	4	5
3	Angle (0° at leading edge)	-144	144	72	0	-72
4	Surface Temperatrue(°C)	41.16	42.56	41.28	39.51	40.82
5	HFS Temperature (°C)	42.69	44.26	43.39	41.22	42.28
6	HFS Reading(μV)	406.93	497.14	640.96	790.34	591.32
7	HFS sensitivity(μV/W/m2)	0.785	0.888	0.893	0.927	0.906
8	Temperature for calculation (°C)	31.675	32.375	31.735	30.85	31.505
9	corrected factor (μV/W/m2)	0.784	0.887	0.892	0.927	0.905
10	Air conductivity k (W/m K)	0.027	0.027	0.027	0.027	0.027
11	q"(W/m2)	466.92	504.65	646.55	767.26	587.77
12	h(W/m2K)	25.08	25.21	34.50	45.21	32.15
13	local Nu	49.0	49.3	67.4	88.3	62.8
14	Overall Nu	63.4				

Table C.5 Stationary experiment for $v = 3.81 \text{m/s}$ and HFS#5 at leading edge

1	Room Temperature (°C)	22.03				
2	HFS #	1	2	3	4	5
3	Angle (0° at leading edge)	-72	-144	144	72	0
4	Surface Temperatrue(°C)	38.49	40.12	40.72	39.37	38.03
5	HFS Temperature (°C)	40.09	41.94	42.28	40.91	39.92
6	HFS Reading(μV)	398.79	437.05	431.02	600.45	783.14
7	HFS sensitivity(μV/W/m2)	0.785	0.888	0.893	0.927	0.906
8	Temperature for calculation (°C)	31.14	32.065	32.235	31.55	31.055
9	corrected factor (μV/W/m2)	0.785	0.887	0.892	0.926	0.906
10	Air conductivity k (W/m K)	0.027	0.027	0.027	0.027	0.027
11	q"(W/m2)	457.32	443.50	435.01	583.35	778.06
12	h(W/m2K)	27.78	24.52	23.28	33.64	48.63
13	local Nu	54.3	47.9	45.5	65.7	95.0
14	Overall Nu	61.7				

Table C.6 Stationary experiment for $v = 8.93 \text{m/s}$ and HFS#1 at leading edge

1	Room Temperature (°C)	24.341				
2	HFS #	1	2	3	4	5
3	Angle (0° at leading edge)	0	72	144	-144	-72
4	Surface Temperatrue(°C)	37.96	40.12	40.66	39.71	39.98
5	HFS Temperature (°C)	40.68	43.27	43.70	43.08	43.67
6	HFS Reading(μV)	866.50	923.58	663.54	650.43	840.32
7	HFS factor(μV/W/m^2)	0.785	0.888	0.893	0.927	0.906
8	Temperature for calculation	31.15	32.23	32.50	32.03	32.16
9	corrected factor (μV/W/m2)	0.785	0.887	0.891	0.926	0.905
10	Air conductivity k (W/m K)	0.027	0.027	0.027	0.027	0.027
11	q"(W/m^2)	1104.091	1041.536	744.3106	702.4856	928.7449
12	h(W/m^{2}K)	81.05	66.01	45.62	45.71	59.39
13	local Nu	155.2	126.0	87.0	87.3	113.4
14	Overall Nu	113.8				

Table C.7 Stationary experiment for $v = 8.93 \text{m/s}$ and HFS#2 at leading edge

1	Room Temperature (°C)	24.178				
2	HFS #	1	2	3	4	5
3	Angle (0° at leading edge)	-72	0	72	144	-144
4	Surface Temperatrue(°C)	40.14	39.56	41.31	40.89	41.65
5	HFS Temperature (°C)	42.62	42.85	43.90	43.58	44.68
6	HFS Reading(μV)	677.32	1170.32	1050.83	687.32	805.20
7	HFS factor(μV/W/m^2)	0.785	0.888	0.893	0.927	0.906
8	Temperature for calculation	32.24	31.95	32.83	32.62	33.00
9	corrected factor (μV/W/m2)	0.784	0.887	0.891	0.925	0.904
10	Air conductivity k (W/m K)	0.027	0.027	0.027	0.027	0.027
11	q"(W/m^2)	864.0573	1319.39	1179.161	742.8008	890.7308
12	h(W/m^{2}K)	54.12	85.77	68.82	44.45	50.98
13	local Nu	103.3	163.9	131.1	84.8	97.1
14	Overall Nu	116.0				

Table C.8 Stationary experiment for $v = 8.93 \text{m/s}$ and HFS#3 at leading edge

1	Room Temperature (°C)	24.235				
2	HFS #	1	2	3	4	5
3	Angle (0° at leading edge)	-144	-72	0	72	144
4	Surface Temperatrue(°C)	41.02	40.67	37.12	37.78	40.11
5	HFS Temperature (°C)	42.75	42.86	41.11	41.19	43.37
6	HFS Reading(μV)	517.32	803.23	1001.32	770.32	751.56
7	HFS factor(μV/W/m^2)	0.785	0.888	0.893	0.927	0.906
8	Temperature for calculation	32.68	32.51	30.73	31.06	32.23
9	corrected factor (μV/W/m2)	0.784	0.886	0.893	0.927	0.905
10	Air conductivity k (W/m K)	0.027	0.027	0.026	0.027	0.027
11	q"(W/m^2)	660.2567	906.0842	1121.06	831.1021	830.7031
12	h(W/m^{2}K)	39.34	55.13	87.01	61.36	52.33
13	local Nu	75.0	105.2	166.8	117.5	99.9
14	Overall Nu	112.9				

Table C.9 Stationary experiment for $v = 8.93 \text{m/s}$ and HFS#4 at leading edge

1	Room Temperature (°C)	24.368				
2	HFS #	1	2	3	4	5
3	Angle (0° at leading edge)	144	-144	-72	0	72
4	Surface Temperatrue(°C)	40.76	40.67	40.08	36.87	38.88
5	HFS Temperature (°C)	42.74	43.74	43.09	40.49	42.31
6	HFS Reading(μV)	562.32	693.32	828.32	958.32	934.32
7	HFS factor(μV/W/m^2)	0.785	0.888	0.893	0.927	0.906
8	Temperature for calculation	32.55	32.51	32.21	30.61	31.61
9	corrected factor (μV/W/m2)	0.784	0.886	0.892	0.927	0.905
10	Air conductivity k (W/m K)	0.027	0.027	0.027	0.026	0.027
11	q"(W/m^2)	717.5902	782.1002	928.8615	1033.426	1032.022
12	h(W/m^{2}K)	43.78	47.98	59.10	82.66	71.12
13	local Nu	83.5	91.5	112.8	158.5	136.0
14	Overall Nu	116.5				

Table C.10 Stationary experiment for $v = 8.93 m/s$ and HFS#5 at leading edge

1	Room Temperature (°C)	24.373				
2	HFS #	1	2	3	4	5
3	Angle (0° at leading edge)	72	144	-144	-72	0
4	Surface Temperatrue(°C)	39.34	40.76	40.84	39.67	36.62
5	HFS Temperature (°C)	41.24	43.84	43.58	42.47	41.31
6	HFS Reading(μV)	740.43	701.83	623.32	660.42	982.32
7	HFS factor(μV/W/m^2)	0.785	0.888	0.893	0.927	0.906
8	Temperature for calculation	31.84	32.55	32.59	32.01	30.48
9	corrected factor (μV/W/m2)	0.784	0.886	0.891	0.926	0.906
10	Air conductivity k (W/m K)	0.027	0.027	0.027	0.027	0.026
11	q"(W/m^2)	944.1569	791.7383	699.2628	713.2597	1083.713
12	h(W/m^2K)	63.08	48.32	42.47	46.63	88.49
13	local Nu	120.6	92.2	81.0	89.1	169.8
14	Overall Nu	110.5				

Table C.11 Oscillating experiment, stationary, $v = 1.95 \text{m/s}$, HFS#1 at leading edge

1	Room Temperature (°C)	22.2				
2	HFS #	1	2	3	4	5
3	Angle (0° at leading edge)	0	-72	-144	144	72
4	Surface Temperatrue(°C)	69.02	72.03	73.43	74.08	73.88
5	HFS Temperature (°C)	70.10	72.99	73.87	74.98	74.84
6	HFS Reading(μV)	1293.34	1056.44	992.73	1012.58	1526.78
7	HFS factor(μV/W/m^2)	0.785	0.888	0.893	0.927	0.906
8	Temperature for calculation	45.61	47.11	47.82	48.14	48.04
9	corrected factor (μV/W/m2)	0.773	0.873	0.877	0.910	0.890
10	Air conductivity k (W/m K)	0.028	0.028	0.028	0.028	0.028
11	q"(W/m^2)	1505.987	1089.136	1018.448	1001.043	1544.218
12	h(W/m^{2}K)	32.17	21.86	19.88	19.30	29.88
13	local Nu	59.1	40.0	36.3	35.2	54.6
14	Overall Nu	45.1				

Table C.12 Oscillating experiment, stationary, $v = 1.95 \text{m/s}$, HFS#2 at leading edge

1	Room Temperature (°C)	23.55				
2	HFS #	1	2	3	4	5
3	Angle (0° at leading edge)	72	0	-72	-144	144
4	Surface Temperatrue(°C)	70.70	68.77	70.94	72.71	73.80
5	HFS Temperature (°C)	72.35	71.33	71.99	73.69	74.97
6	HFS Reading(μV)	1006.59	1421.27	1021.99	937.50	1008.07
7	HFS factor(μV/W/m^2)	0.785	0.888	0.893	0.927	0.906
8	Temperature for calculation	47.12	46.16	47.24	48.13	48.68
9	corrected factor (μV/W/m2)	0.772	0.874	0.878	0.910	0.889
10	Air conductivity k (W/m K)	0.028	0.028	0.028	0.028	0.028
11	q"(W/m^2)	1173.919	1463.819	1047.861	926.8122	1020.244
12	h(W/m^{2}K)	24.90	32.37	22.11	18.85	20.30
13	local Nu	45.6	59.4	40.5	34.4	37.0
14	Overall Nu	43.4				

Table C.13 Oscillating experiment, stationary, $v = 1.95 \text{m/s}$, HFS#3 at leading edge

1	Room Temperature (°C)	23.67				
2	HFS #	1	2	3	4	5
3	Angle (0° at leading edge)	144	72	0	-72	-144
4	Surface Temperatrue(°C)	70.50	68.62	65.70	66.98	69.68
5	HFS Temperature (°C)	71.59	70.94	67.88	68.72	70.97
6	HFS Reading(μV)	629.49	1226.77	1382.96	890.38	887.85
7	HFS factor(μV/W/m^2)	0.785	0.888	0.893	0.927	0.906
8	Temperature for calculation	47.09	46.15	44.69	45.33	46.68
9	corrected factor (μV/W/m2)	0.772	0.874	0.880	0.913	0.891
10	Air conductivity k (W/m K)	0.028	0.028	0.028	0.028	0.028
11	q"(W/m^2)	734.0972	1263.483	1414.235	877.7041	896.7334
12	h(W/m^{2}K)	15.67	28.11	33.65	20.27	19.49
13	local Nu	28.7	51.6	62.0	37.3	35.7
14	Overall Nu	43.1				

Table C.14 Oscillating experiment, stationary, $v = 1.95 \text{m/s}$, HFS#4 at leading edge

1	Room Temperature (°C)	22.78				
2	HFS #	1	2	3	4	5
3	Angle (0° at leading edge)	-144	144	72	0	-72
4	Surface Temperatrue(°C)	65.12	65.88	63.23	60.54	63.01
5	HFS Temperature (°C)	66.29	67.54	65.10	62.78	64.73
6	HFS Reading(μV)	567.66	750.09	1010.60	1199.08	914.19
7	HFS factor(μV/W/m^2)	0.785	0.888	0.893	0.927	0.906
8	Temperature for calculation	43.95	44.33	43.01	41.66	42.90
9	corrected factor (μV/W/m2)	0.774	0.875	0.882	0.916	0.895
10	Air conductivity k (W/m K)	0.028	0.028	0.027	0.027	0.027
11	q"(W/m^2)	659.8576	771.0887	1031.658	1177.522	919.7479
12	h(W/m^{2}K)	15.58	17.89	25.50	31.18	22.86
13	local Nu	28.8	33.0	47.2	58.0	42.4
14	Overall Nu	41.9				

Table C.15 Oscillating experiment, stationary, $v = 1.95 \text{m/s}$, HFS#5 at leading edge

1	Room Temperature (°C)	23.32				
2	HFS #	1	2	3	4	5
3	Angle (0° at leading edge)	-72	-144	144	72	0
4	Surface Temperatrue(°C)	70.87	72.85	73.72	73.10	71.44
5	HFS Temperature (°C)	71.93	74.50	74.80	74.25	72.56
6	HFS Reading(μV)	862.40	891.93	966.52	1344.26	1663.40
7	HFS factor(μV/W/m^2)	0.785	0.888	0.893	0.927	0.906
8	Temperature for calculation	46.53	47.52	47.96	47.65	46.82
9	corrected factor (μV/W/m2)	0.772	0.873	0.877	0.911	0.891
10	Air conductivity k (W/m K)	0.028	0.028	0.028	0.028	0.028
11	q"(W/m^2)	1005.152	919.9132	991.7145	1328.287	1680.296
12	h(W/m^{2}K)	21.14	18.57	19.68	26.68	34.92
13	local Nu	38.8	34.0	35.9	48.8	64.0
14	Overall Nu	44.3				

Table C.16 Oscillating experiment, oscillating, $v = 1.95 \text{m/s}$, HFS#1 at leading edge

1	Room Temperature (°C)	23.44				
2	HFS #	1	2	3	4	5
3	Angle (0° at leading edge)	0	-72	-144	144	72
4	Surface Temperatrue(°C)	71.44	74.60	76.37	77.32	76.61
5	HFS Temperature (°C)	72.82	75.75	76.81	78.08	77.81
6	HFS Reading(μV)	1347.54	1095.51	997.36	1094.82	1576.99
7	HFS factor(μV/W/m^2)	0.785	0.888	0.893	0.927	0.906
8	Temperature for calculation	47.44	49.02	49.91	50.38	50.03
9	corrected factor (μV/W/m2)	0.771	0.871	0.875	0.908	0.888
10	Air conductivity k (W/m K)	0.028	0.028	0.028	0.028	0.028
11	q"(W/m^2)	1746.715	1257.347	1139.31	1205.358	1775.812
12	h(W/m^{2}K)	36.39	24.58	21.52	22.37	33.40
13	local Nu	66.6	44.8	39.1	40.6	60.7
14	Overall Nu	50.4				

Table C.17 Oscillating experiment, oscillating, $v = 1.95 \text{m/s}$, HFS#2 at leading edge

1	Room Temperature (°C)	23.60				
2	HFS #	1	2	3	4	5
3	Angle (0° at leading edge)	72	0	-72	-144	144
4	Surface Temperatrue(°C)	71.83	69.69	72.03	74.10	75.28
5	HFS Temperature (°C)	73.63	72.47	73.11	75.14	76.42
6	HFS Reading(μV)	1024.37	1473.95	1052.34	861.01	1049.66
7	HFS factor(μV/W/m^2)	0.785	0.888	0.893	0.927	0.906
8	Temperature for calculation	47.72	46.65	47.82	48.85	49.44
9	corrected factor (μV/W/m2)	0.771	0.873	0.877	0.910	0.889
10	Air conductivity k (W/m K)	0.028	0.028	0.028	0.028	0.028
11	q"(W/m^2)	1328.191	1687.594	1199.559	946.4624	1181.293
12	h(W/m^{2}K)	27.54	36.61	24.77	18.74	22.86
13	local Nu	50.3	67.1	45.3	34.2	41.6
14	Overall Nu	47.7				

Table C.18 Oscillating experiment, oscillating, $v = 1.95 \text{m/s}$, HFS#3 at leading edge

1	Room Temperature (°C)	23.66				
2	HFS #	1	2	3	4	5
3	Angle (0° at leading edge)	144	72	0	-72	-144
4	Surface Temperatrue(°C)	71.44	74.60	76.37	77.32	76.61
5	HFS Temperature (°C)	72.82	75.75	76.81	78.08	77.81
6	HFS Reading(μV)	1347.54	1095.51	997.36	1094.82	1576.99
7	HFS factor(μV/W/m^2)	0.785	0.888	0.893	0.927	0.906
8	Temperature for calculation	47.44	49.02	49.91	50.38	50.03
9	corrected factor (μV/W/m2)	0.771	0.871	0.875	0.908	0.888
10	Air conductivity k (W/m K)	0.028	0.028	0.028	0.028	0.028
11	q"(W/m^2)	1746.715	1257.347	1139.31	1205.358	1775.812
12	h(W/m^{2}K)	36.39	24.58	21.52	22.37	33.40
13	local Nu	66.6	44.8	39.1	40.6	60.7
14	Overall Nu	50.4				

Table C.19 Oscillating experiment, oscillating, $v = 1.95 \text{m/s}$, HFS#4 at leading edge

1	Room Temperature (°C)	23.11				
2	HFS #	1	2	3	4	5
3	Angle (0° at leading edge)	-144	144	72	0	-72
4	Surface Temperatrue(°C)	65.59	66.26	63.40	60.39	63.26
5	HFS Temperature (°C)	66.61	67.79	65.23	62.90	64.84
6	HFS Reading(μV)	539.39	722.84	1002.97	1222.53	922.09
7	HFS factor(μV/W/m^2)	0.785	0.888	0.893	0.927	0.906
8	Temperature for calculation	44.35	44.69	43.26	41.75	43.19
9	corrected factor (μV/W/m2)	0.774	0.875	0.881	0.916	0.894
10	Air conductivity k (W/m K)	0.028	0.028	0.027	0.027	0.027
11	q"(W/m^2)	696.9578	825.9459	1137.928	1334.07	1031.084
12	h(W/m^{2}K)	16.41	19.14	28.24	35.79	25.68
13	local Nu	30.3	35.3	52.3	66.5	47.5
14	Overall Nu	46.4				

Table C.20 Oscillating experiment, oscillating, $v = 1.95 \text{m/s}$, HFS#5 at leading edge

1	Room Temperature (°C)	23.49				
2	HFS #	1	2	3	4	5
3	Angle (0° at leading edge)	-72	-144	144	72	0
4	Surface Temperatrue(°C)	72.17	74.49	75.26	73.93	71.84
5	HFS Temperature (°C)	73.22	76.00	76.24	75.54	73.82
6	HFS Reading(μV)	894.88	875.55	965.35	1389.05	1732.60
7	HFS factor(μV/W/m^2)	0.785	0.888	0.893	0.927	0.906
8	Temperature for calculation	47.83	48.99	49.37	48.71	47.67
9	corrected factor (μV/W/m2)	0.771	0.871	0.876	0.910	0.890
10	Air conductivity k (W/m K)	0.028	0.028	0.028	0.028	0.028
11	q"(W/m^2)	1160.433	1004.859	1102.148	1526.693	1946.356
12	h(W/m^{2}K)	23.84	19.70	21.29	30.27	40.26
13	local Nu	43.6	35.9	38.8	55.2	73.6
14	Overall Nu	49.4				

Table C.21 Oscillating experiment, stationary, $v = 4.78 \text{m/s}$, HFS#1 at leading edge

1	Room Temperature (°C)	24.26				
2	HFS #	1	2	3	4	5
3	Angle (0° at leading edge)	0	-72	-144	144	72
4	Surface Temperatrue(°C)	42.40	44.60	45.14	45.86	45.18
5	HFS Temperature (°C)	44.04	46.11	46.43	46.95	46.79
6	HFS Reading(μV)	735.43	588.44	611.83	627.68	915.35
7	HFS factor(μV/W/m^2)	0.785	0.888	0.893	0.927	0.906
8	Temperature for calculation	33.33	34.43	34.70	35.06	34.72
9	corrected factor (μV/W/m2)	0.783	0.885	0.889	0.923	0.902
10	Air conductivity k (W/m K)	0.027	0.027	0.027	0.027	0.027
11	q"(W/m^2)	939.2861	665.1615	687.9273	680.132	1014.46
12	h(W/m^{2}K)	51.79	32.70	32.94	31.49	48.49
13	local Nu	98.6	62.0	62.5	59.6	91.9
14	Overall Nu	74.9				

Table C.22 Oscillating experiment, stationary, $v = 4.78 \text{m/s}$, HFS#2 at leading edge

1	Room Temperature (°C)	24.54				
2	HFS #	1	2	3	4	5
3	Angle (0° at leading edge)	72	0	-72	-144	144
4	Surface Temperatrue(°C)	45.99	45.01	47.15	47.65	48.21
5	HFS Temperature (°C)	47.24	46.97	47.97	48.75	49.34
6	HFS Reading(μV)	640.12	971.91	699.16	736.16	784.32
7	HFS factor(μV/W/m^2)	0.785	0.888	0.893	0.927	0.906
8	Temperature for calculation	35.27	34.77	35.84	36.10	36.38
9	corrected factor (μV/W/m2)	0.781	0.884	0.888	0.922	0.901
10	Air conductivity k (W/m K)	0.027	0.027	0.027	0.027	0.027
11	q"(W/m^2)	819.2509	1099.037	787.0803	798.5573	870.7752
12	h(W/m^{2}K)	38.19	53.70	34.81	34.55	36.79
13	local Nu	72.3	101.8	65.8	65.2	69.4
14	Overall Nu	74.9				

Table C.23 Oscillating experiment, stationary, $v = 4.78 \text{m/s}$, HFS#3 at leading edge

1	Room Temperature (°C)	24.71				
2	HFS #	1	2	3	4	5
3	Angle (0° at leading edge)	144	72	0	-72	-144
4	Surface Temperatrue(°C)	45.03	45.01	43.62	44.03	45.24
5	HFS Temperature (°C)	45.82	46.65	45.40	45.51	46.01
6	HFS Reading(μV)	469.15	772.70	959.78	619.39	734.63
7	HFS factor(μV/W/m^2)	0.785	0.888	0.893	0.927	0.906
8	Temperature for calculation	34.87	34.86	34.17	34.37	34.98
9	corrected factor (μV/W/m2)	0.782	0.884	0.890	0.924	0.902
10	Air conductivity k (W/m K)	0.027	0.027	0.027	0.027	0.027
11	q"(W/m^2)	600.1894	873.8497	1078.539	670.6506	814.3881
12	h(W/m^{2}K)	29.54	43.05	57.03	34.71	39.67
13	local Nu	56.0	81.6	108.3	65.9	75.1
14	Overall Nu	77.4				

Table C.24 Oscillating experiment, stationary, $v = 4.78 \text{m/s}$, HFS#4 at leading edge

1	Room Temperature (°C)	25.12				
2	HFS #	1	2	3	4	5
3	Angle (0° at leading edge)	-144	144	72	0	-72
4	Surface Temperatrue(°C)	47.16	48.80	47.61	44.78	46.10
5	HFS Temperature (°C)	47.96	50.03	49.26	46.83	47.63
6	HFS Reading(μV)	476.63	622.54	876.42	995.04	722.53
7	HFS factor(μV/W/m^2)	0.785	0.888	0.893	0.927	0.906
8	Temperature for calculation	36.14	36.96	36.36	34.95	35.61
9	corrected factor (μV/W/m2)	0.781	0.882	0.888	0.923	0.901
10	Air conductivity k (W/m K)	0.027	0.027	0.027	0.027	0.027
11	q"(W/m^2)	610.5771	705.6083	987.1767	1078.054	801.5211
12	h(W/m^{2}K)	27.71	29.79	43.90	54.83	38.20
13	local Nu	52.3	56.1	82.8	103.9	72.2
14	Overall Nu	73.5				

Table C.25 Oscillating experiment, stationary, $v = 4.78 \text{m/s}$, HFS#5 at leading edge

1	Room Temperature (°C)	25.68				
2	HFS #	1	2	3	4	5
3	Angle (0° at leading edge)	-72	-144	144	72	0
4	Surface Temperatrue(°C)	51.79	53.50	54.74	53.78	51.75
5	HFS Temperature (°C)	52.32	54.65	55.46	54.58	52.41
6	HFS Reading(μV)	652.19	797.66	849.52	1131.71	1394.87
7	HFS factor(μV/W/m^2)	0.785	0.888	0.893	0.927	0.906
8	Temperature for calculation	38.02	38.88	39.50	39.02	38.01
9	corrected factor (μV/W/m2)	0.779	0.880	0.885	0.919	0.899
10	Air conductivity k (W/m K)	0.027	0.027	0.027	0.027	0.027
11	q"(W/m^2)	837.1562	905.9369	960.0565	1231.432	1551.304
12	h(W/m^{2}K)	32.07	32.57	33.03	43.82	59.51
13	local Nu	60.2	61.0	61.8	82.1	111.8
14	Overall Nu	75.4				

Table C.26 Oscillating experiment, oscillating, $v = 4.78 \text{m/s}$, HFS#1 at leading edge

1	Room Temperature (°C)	24.47				
2	HFS #	1	2	3	4	5
3	Angle (0° at leading edge)	0	-72	-144	144	72
4	Surface Temperatrue(°C)	47.37	50.00	51.43	52.31	51.54
5	HFS Temperature (°C)	48.77	51.16	52.13	53.17	52.75
6	HFS Reading(μV)	939.65	801.05	779.70	852.64	1168.34
7	HFS factor(μV/W/m^2)	0.785	0.888	0.893	0.927	0.906
8	Temperature for calculation	35.92	37.24	37.95	38.39	38.01
9	corrected factor (μV/W/m2)	0.781	0.882	0.886	0.920	0.899
10	Air conductivity k (W/m K)	0.027	0.027	0.027	0.027	0.027
11	q"(W/m^2)	1203.449	908.2028	879.7107	927.1619	1299.369
12	h(W/m^{2}K)	52.56	35.57	32.63	33.30	48.00
13	local Nu	99.3	66.9	61.3	62.5	90.1
14	Overall Nu	76.0				

Table C.27 Oscillating experiment, oscillating, $v = 4.78 \text{m/s}$, HFS#2 at leading edge

1	Room Temperature (°C)	24.60				
2	HFS #	1	2	3	4	5
3	Angle (0° at leading edge)	72	0	-72	-144	144
4	Surface Temperatrue(°C)	46.60	45.54	47.71	48.47	48.71
5	HFS Temperature (°C)	47.82	47.48	48.46	49.41	50.02
6	HFS Reading(μV)	646.85	992.64	708.95	719.76	786.24
7	HFS factor(μV/W/m^2)	0.785	0.888	0.893	0.927	0.906
8	Temperature for calculation	35.60	35.07	36.15	36.54	36.66
9	corrected factor (μV/W/m2)	0.781	0.884	0.888	0.921	0.900
10	Air conductivity k (W/m K)	0.027	0.027	0.027	0.027	0.027
11	q"(W/m^2)	828.164	1122.837	798.3684	781.1327	873.1703
12	h(W/m^{2}K)	37.65	53.61	34.55	32.72	36.22
13	local Nu	71.2	101.5	65.2	61.7	68.3
14	Overall Nu	73.6				

Table C.28 Oscillating experiment, oscillating, $v = 4.78 \text{m/s}$, HFS#3 at leading edge

1	Room Temperature (°C)	24.96				
2	HFS #	1	2	3	4	5
3	Angle (0° at leading edge)	144	72	0	-72	-144
4	Surface Temperatrue(°C)	45.99	45.78	44.33	44.87	46.02
5	HFS Temperature (°C)	46.74	47.43	46.13	46.26	46.87
6	HFS Reading(μV)	448.55	785.42	980.82	618.52	678.36
7	HFS factor(μV/W/m^2)	0.785	0.888	0.893	0.927	0.906
8	Temperature for calculation	35.47	35.37	34.64	34.92	35.49
9	corrected factor (μV/W/m2)	0.781	0.884	0.889	0.923	0.902
10	Air conductivity k (W/m K)	0.027	0.027	0.027	0.027	0.027
11	q"(W/m^2)	574.2026	888.716	1102.753	670.0992	752.4296
12	h(W/m^2K)	27.31	42.69	56.94	33.66	35.73
13	local Nu	51.7	80.8	108.0	63.8	67.6
14	Overall Nu	74.3				

Table C.29 Oscillating experiment, oscillating, $v = 4.78 \text{m/s}$, HFS#4 at leading edge

1	Room Temperature (°C)	25.43				
2	HFS #	1	2	3	4	5
3	Angle (0° at leading edge)	-144	144	72	0	-72
4	Surface Temperatrue(°C)	47.58	49.12	47.78	44.78	46.21
5	HFS Temperature (°C)	48.34	50.26	49.35	46.95	47.77
6	HFS Reading(μV)	461.85	609.39	871.20	983.47	710.08
7	HFS factor(μV/W/m^2)	0.785	0.888	0.893	0.927	0.906
8	Temperature for calculation	36.51	37.28	36.61	35.11	35.82
9	corrected factor (μV/W/m2)	0.780	0.882	0.888	0.923	0.901
10	Air conductivity k (W/m K)	0.027	0.027	0.027	0.027	0.027
11	q"(W/m^2)	591.8791	690.9376	981.5529	1065.696	787.8826
12	h(W/m^{2}K)	26.72	29.16	43.92	55.07	37.92
13	local Nu	50.4	54.9	82.8	104.3	71.6
14	Overall Nu	72.8				

Table C.30 Oscillating experiment, oscillating, $v = 4.78 \text{m/s}$, HFS#5 at leading edge

1	Room Temperature (°C)	25.74				
2	HFS #	1	2	3	4	5
3	Angle (0° at leading edge)	-72	-144	144	72	0
4	Surface Temperatrue(°C)	50.75	52.53	53.68	52.93	50.77
5	HFS Temperature (°C)	51.33	53.68	54.45	53.53	51.43
6	HFS Reading(μV)	619.44	743.92	797.77	1072.24	1339.75
7	HFS factor(μV/W/m^2)	0.785	0.888	0.893	0.927	0.906
8	Temperature for calculation	37.61	38.50	39.07	38.70	37.62
9	corrected factor (μV/W/m2)	0.779	0.881	0.885	0.919	0.900
10	Air conductivity k (W/m K)	0.027	0.027	0.027	0.027	0.027
11	q"(W/m^2)	794.7624	844.5623	901.1743	1166.328	1489.399
12	h(W/m^{2}K)	31.78	31.52	32.26	42.90	59.50
13	local Nu	59.7	59.1	60.4	80.4	111.9
14	Overall Nu	74.3				

Appendix D - Temperature maps of the body parts

Figure D.1-D.8 show the temperature map of head, neck, upper arm, forearm, thigh, calf, hand, and foot, respectively.

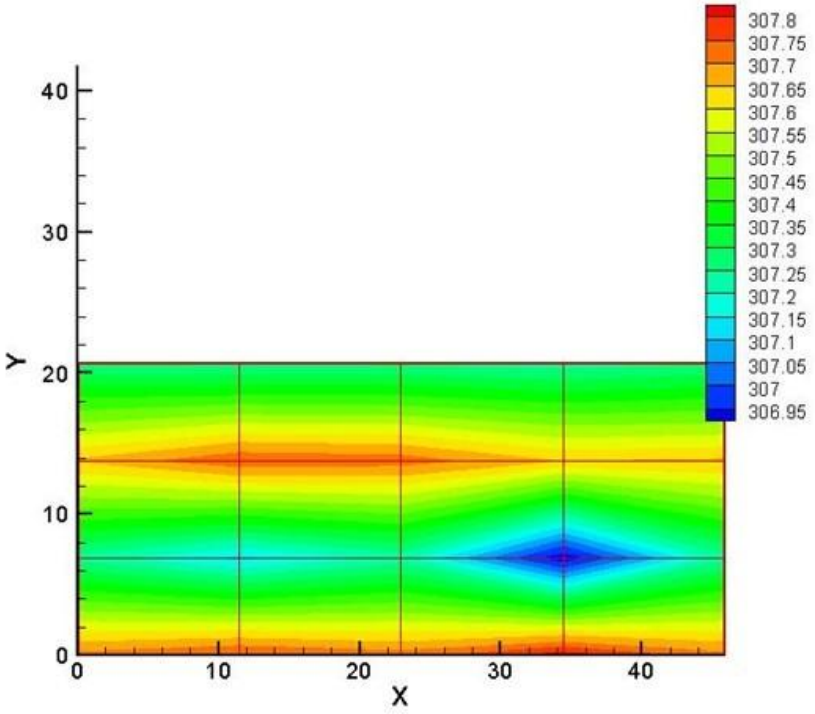

Figure D.1a Head temperature map of old model

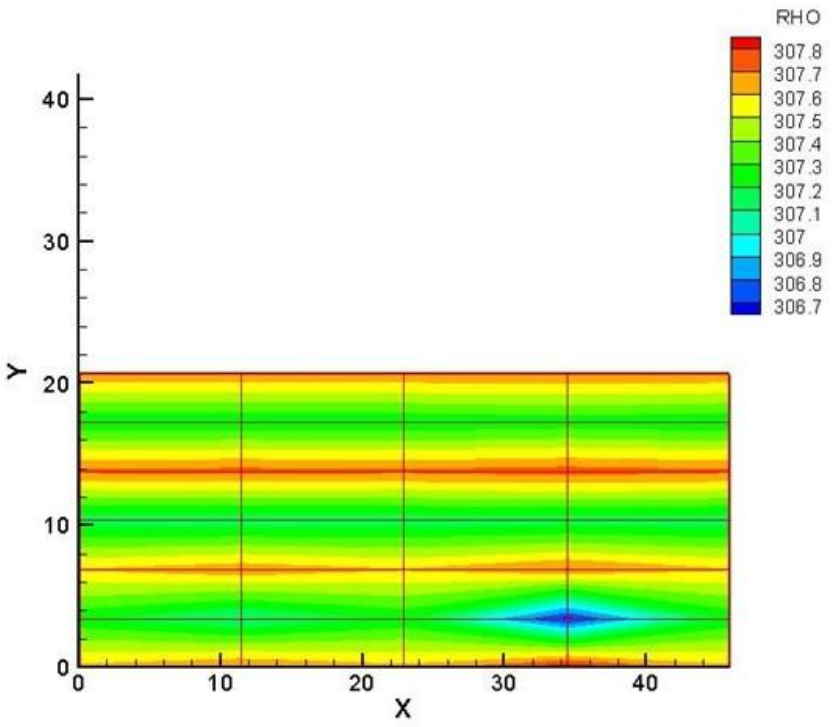

Figure D.1b Head temperature map of new model

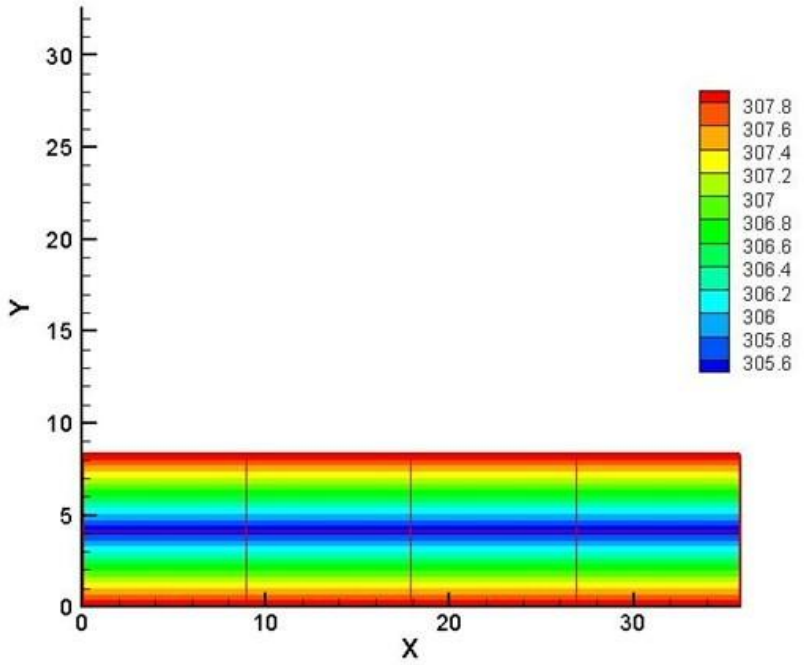

Figure D.2a Neck temperature map of old model

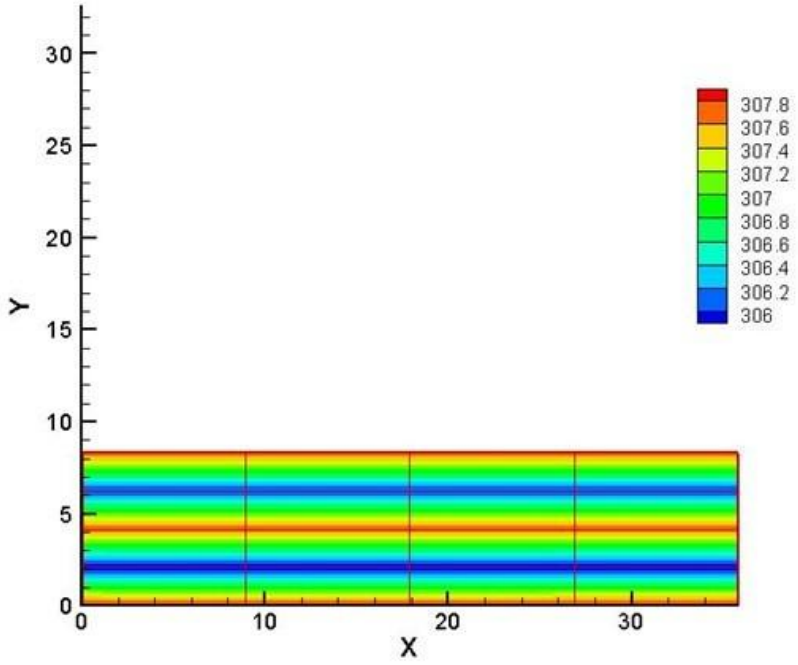

Figure D.2b Neck temperature map of new model

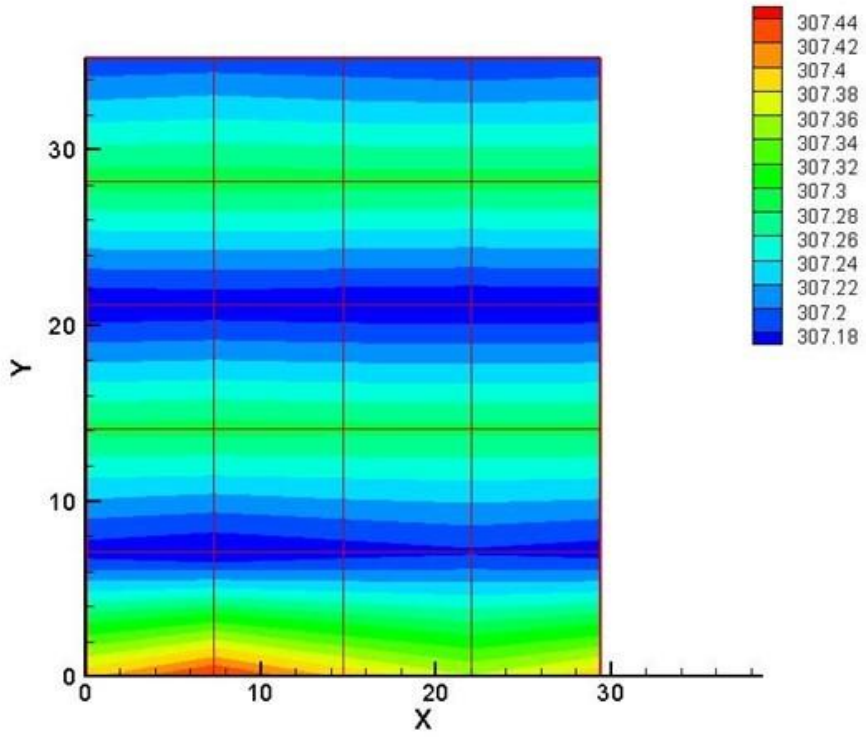

Figure D.3a upper arm temperature map of old model

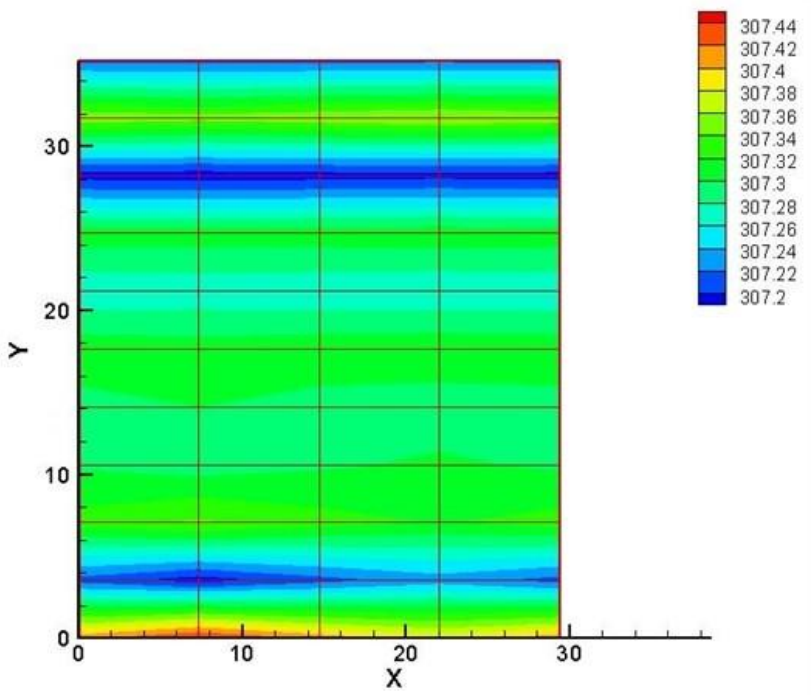

Figure D.3b upper arm temperature map of new model

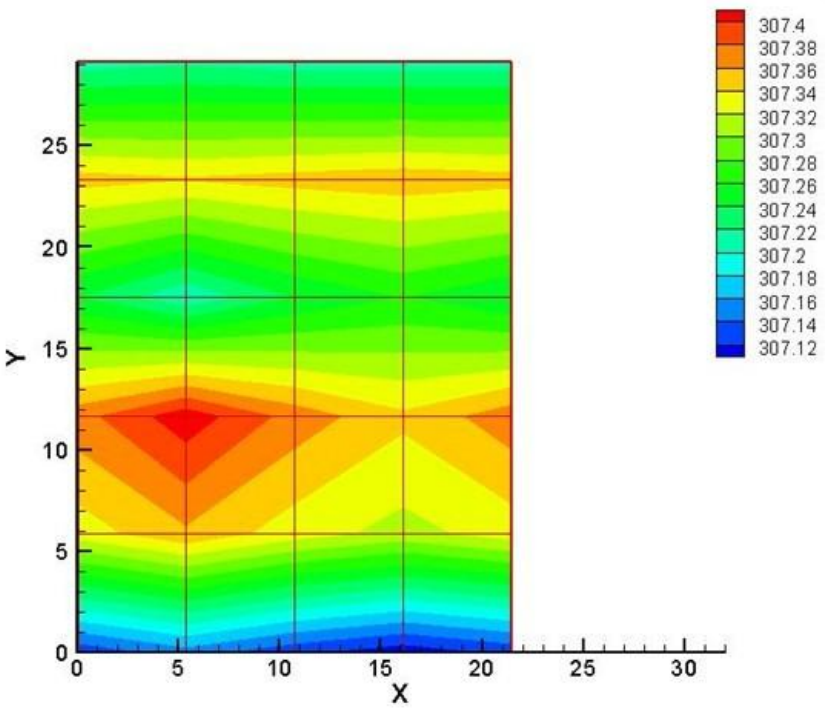

Figure D.4a forearm temperature map of old model

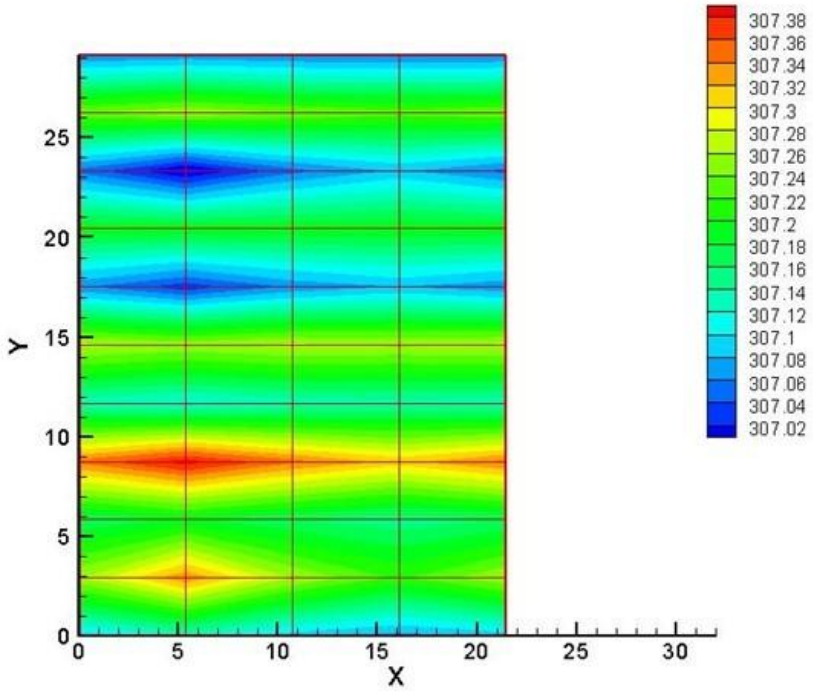

Figure D.4b forearm temperature map of new model

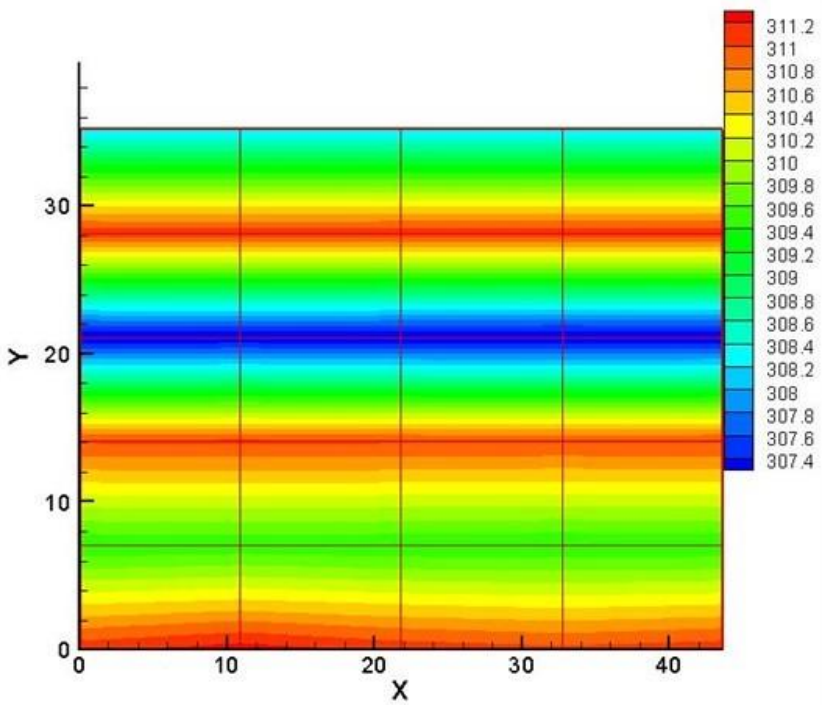

Figure D.5a Thigh temperature map of old model

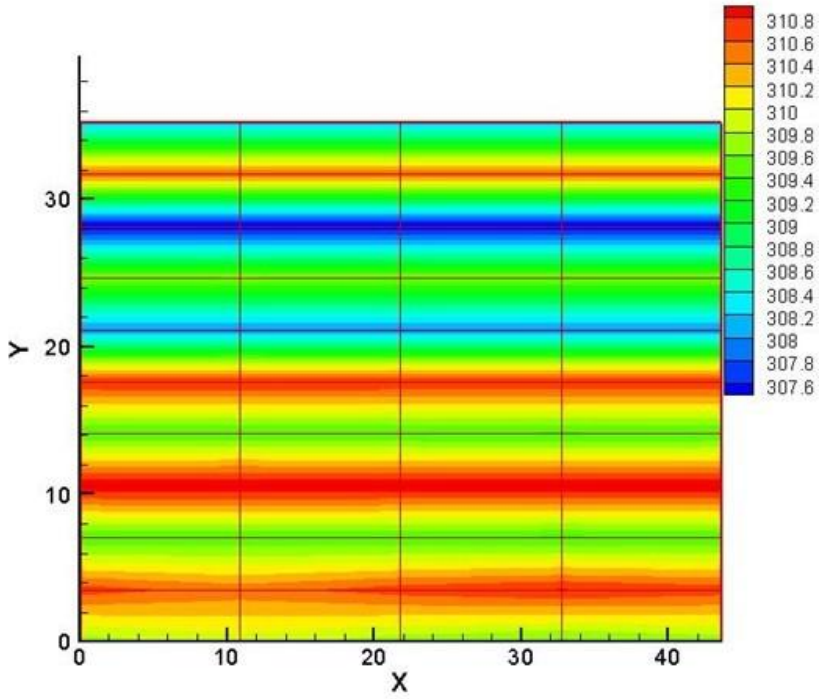

Figure D.5b Thigh temperature map of new model

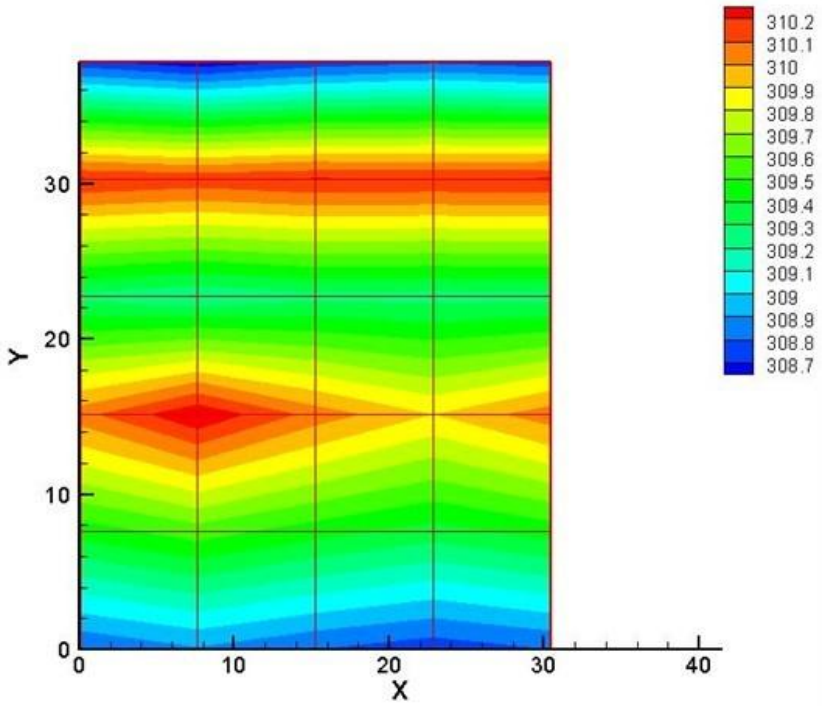

Figure D.6a Calf temperature map of old model

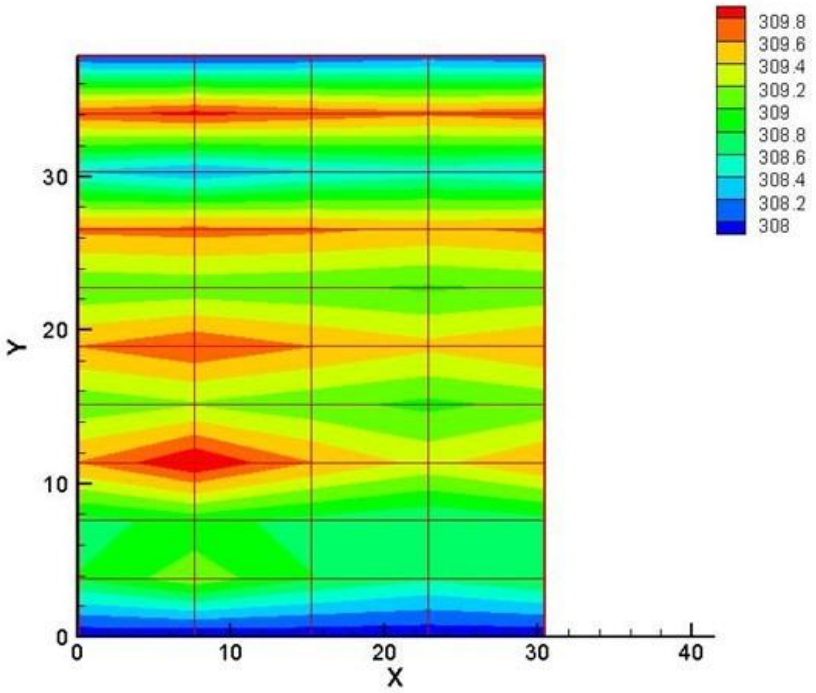

Figure D.6b Calf temperature map of new model

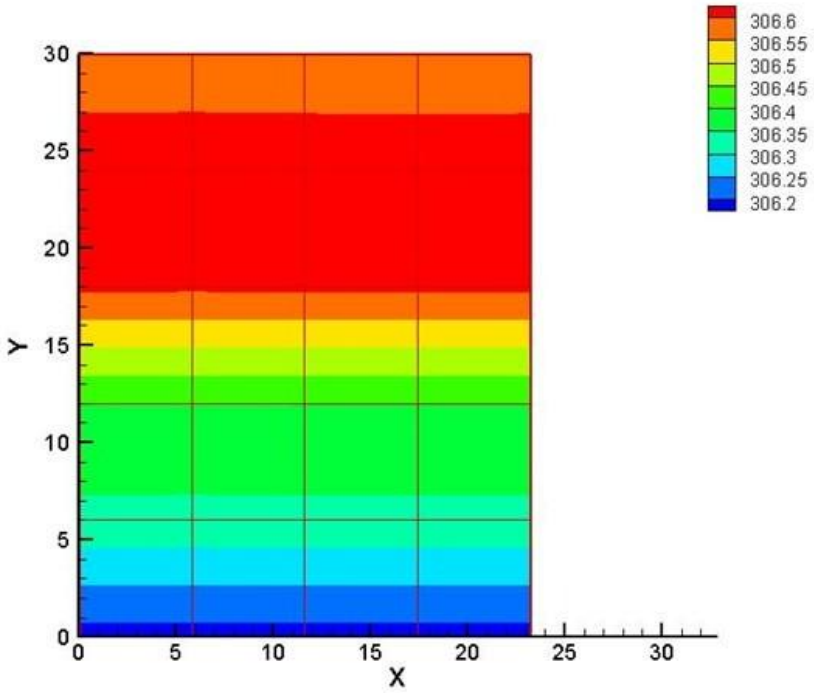

Figure D.7a Hand temperature map of old model

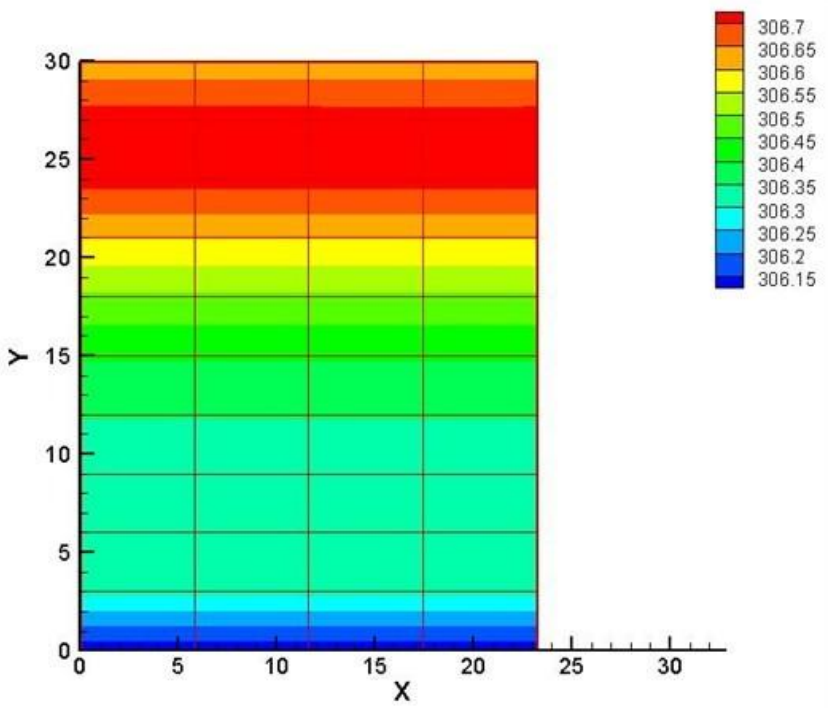

Figure D.7b Hand temperature map of new model

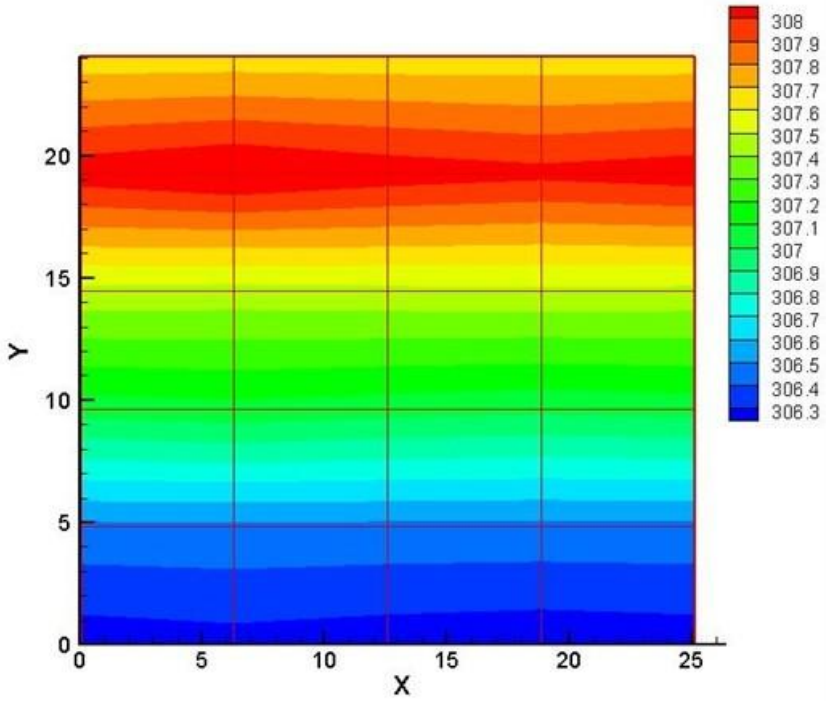

Figure D.8a Foot temperature map of old model

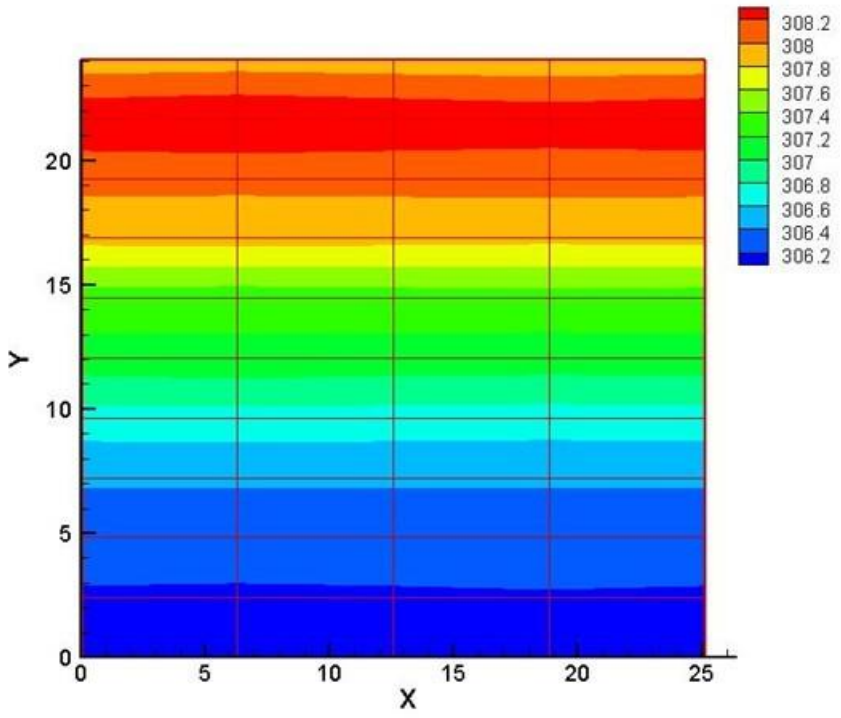

Figure D.8b Foot temperature map of new model